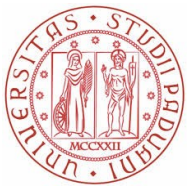

UNIVERSITÀ DEGLI STUDI DI PADOVA

DIPARTIMENTO DI SCIENZE CHIMICHE

CORSO DI LAUREA MAGISTRALE IN MATERIALS SCIENCE

TESI DI LAUREA MAGISTRALE

Platinum nanoparticle activated ZnO/WO3 thin films for optical hydrogen sensors

Relatore: Prof. Alessandro Martucci

Controrelatore: Prof.ssa Alberta Ferrarini

Laureando: Sebastiano Berghino

ANNO ACCADEMICO 2023/2024

Abstract

Hydrogen is predicted to become ever more important as an energy source and vector in the coming years, in the context of the development of a circular economy. Due to its explosivity, there is a growing need for fast and efficient hydrogen sensors, as evidenced by the growing number of publications in scientific literature about this topic.

This thesis focuses on the production of an optical hydrogen sensor composed of WO_3 and ZnO. In particular, films composed of pure ZnO, pure WO_3, and composites containing Zn and WO_3 were synthesized using the sol-gel approach. The sols obtained were deposited on fused silica glass substrates via spin-coating, annealed at 550°C, and coated with platinum nanoparticles. The films thus obtained were characterized via Grazing Incidence X-Ray Diffraction, Ellipsometry, Raman Spectroscopy, Scanning Electron Microscopy, and static and dynamic gas sensing tests.

The effects of ageing, the recovery gas, the synthetic approach, and zinc concentration were investigated. Results demonstrated that ageing of the precursor sols leads to a worsening of gas sensing performance ascribable to an excessive thickness of the films and a change in morphology.

Two different syntheses were compared, one involving the mixing of the precursor sols (M-synthesis) and the other the dissolution of the Zn precursor into the WO_3 sol (S-synthesis). It was discovered that both syntheses lead to a $WO_3/ZnWO_4$ heterostructure, with different effects on film morphology. Both syntheses produced sensitive and fast gas sensors, with performance improving with decreasing zinc concentration. The S-synthesis was selected since it constitutes a simpler approach and produced films with better response and recovery speeds.

The optimal zinc concentration was found to be at a Zn/(W+Zn) molar ratio of 0.067 as it produced the most sensitive films, due to a combination of morphological and compositional factors, such as grain refinement, porosity and formation of heterostructures. The prepared films showed good response ($\Delta Abs_{\lambda=870nm}$= 0.2 at 100°C), fast response and recovery (15-50s) and stability over 10 cycles at 150°C.

Summary

Introduction

Hydrogen is fundamental in many industrial processes, such as ammonia synthesis. Due to its high energy density and the fact that upon combustion it does not produce greenhouse gases, it has received growing interest as an energy source and vector. Unfortunately, it is hazardous to handle, since it has a wide combustible range in air (4-75% vol) and readily reacts with atmospheric oxygen in an explosive manner. For this reason, there is a growing demand for sensitive, fast, and stable hydrogen gas sensors. WO_3, a metal oxide semiconductor widely known for its electrochromic properties, shows good promise as a candidate sensing material, especially for optical sensors, due to its capability of changing color from transparent to blue upon exposure to hydrogen gas, forming tungsten bronze H_xWO_3. This process is called gasochromism.

The gasochromic reaction is favoured by the functionalization via noble metals, especially noble metal nanoparticles, granting a high active surface for hydrogen adsorption on the film. Heterostructures composed of WO_3 and other semiconductor materials have proven themselves in literature as having improved gas sensing performance compared to pristine WO_3. This work aims to enhance the gasochromic properties of WO_3 via zinc doping and to discuss the optimal synthesis and zinc concentration for this purpose.

Chapter 1 first presents the general properties of hydrogen gas, its applications in many industrial processes, and the required gas sensing parameters for an optimal hydrogen sensor. Then, the most common gas sensing devices are discussed, with a particular attention to metal oxide semiconductor sensors.

Chapter 2 discusses the materials employed over the course of this work and their specific importance to hydrogen gas sensors. First, WO_3 and its gasochromic properties are discussed, and a review of its sol-gel syntheses is presented. Then, the effect of noble metal nanoparticle functionalization is discussed, with a particular attention to platinum nanoparticles and their synthesis via polyol approach. Later, ZnO and $ZnWO_4$ are presented, focusing on their hydrogen sensing properties and their applications in sensing devices, especially in combination with the above-mentioned materials, underlining the importance of heterostructure in the improvement of gas sensing.

Chapter 3 reports the experimental procedures and characterization techniques employed during the course of this work. In this chapter, first the sol-gel syntheses of ZnO and WO_3 are presented. Successively, the two synthetic approaches employed for the production of composite films, one based on the mixing of the two sols, the M-synthesis, and the other on

the dissolution of zinc precursor into the WO_3 sol, the S-synthesis, is reported. In the following pages, the film production process is reported, explicating the procedures adopted for substrate preparation, spin-coating deposition, and heat treatment. Finally, the instruments, measurement conditions and data elaboration approaches employed are reported, which were Grazing Incidence X-Ray Diffraction, Scanning Electron Microscopy, Ellipsometry, Raman Spectroscopy, and static and dynamic gas sensing measurements.

Chapter 4 presents the samples investigated and the results of their investigation. First, the detrimental effect of sol and sol mixture ageing on morphology and gas sensing is discussed, together with the effect of employing argon as a recovery gas. Then, the two synthetic approaches are confronted in terms of crystal structure, morphology, and gas sensing properties, proving the formation of the $ZnWO_4$ phase, and leading us to the selection of the most convenient synthesis. Finally, the effect of zinc concentration on crystal structure, morphology, and gas sensing is investigated, which allowed us to determine the best composition for our purpose. Particular attention was paid to determining the optimal operating temperature for our gas sensors, as several different temperatures were employed in the course of dynamic gas sensing measurements.

Chapter 1: Gas Sensing Technologies

In this chapter, an overview of hydrogen and the most common technologies for gas sensing are presented. Section 1.1 explains the importance of hydrogen in today's society and industry and the necessity of effective sensors for it. Section 1.2 presents first the desired characteristics for the ideal hydrogen sensor, and then discusses the most common available sensing technologies available today, focusing in particular on metal oxide semiconductor (MOS) gas sensors.

1.1 Hydrogen and its properties

Hydrogen is the simplest and most abundant element in the universe, but it is not naturally available on Earth due to its high reactivity. As a consequence of this reactivity, hydrogen has several well-established industrial applications, the most important in terms of hydrogen consumption being the refining industry, requiring 26.4 million tons of gas per year. Examples of refining processes that consume hydrogen include hydrocracking, hydrotreating and desulphurization [1].

The second greatest consumer of hydrogen is the fertilizer industry. Ammonia (NH_3), a precursor to many nitrate-based fertilizers, is produced through the Haber-Bosch process in which atmospheric nitrogen is reduced by hydrogen via a metallic catalyst. This fundamental step of the supply chain demands 22.8 million tons of gas per year. Other industrial applications of hydrogen include metallurgy, methanol production, semiconductors, the food industry, glass-making, and fuel for space rockets: these sectors, while consuming each a comparatively low amount of hydrogen, together make up 18% of the world's annual demand. The most recent development in the industrial use of hydrogen is the production of synthetic fuels and biofuels [1]. Figure 1.1 presents hydrogen consumption for industrial use by six major European economies.

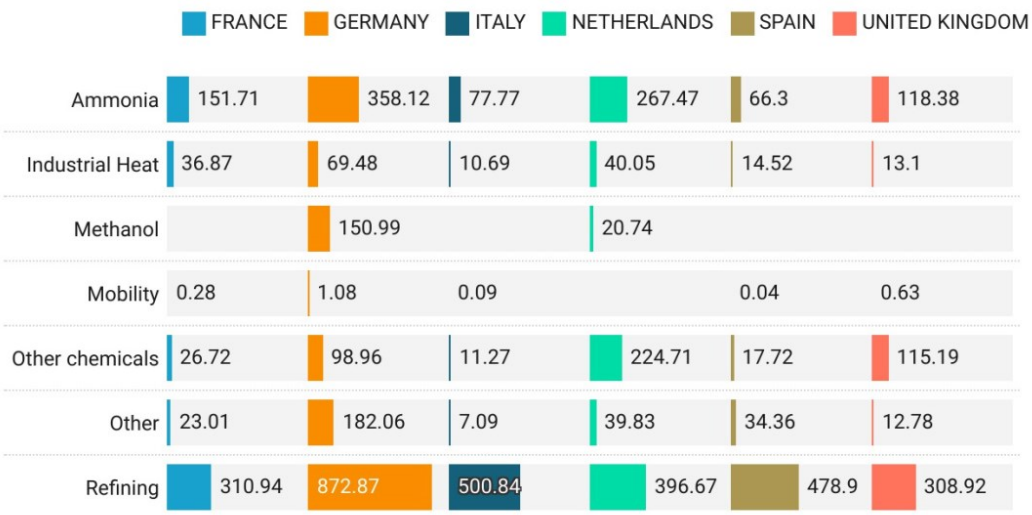

Figure 1.1: European hydrogen consumption by end-use in industrial applications [2]

Hydrogen gas is forecast to become increasingly important in the coming years as an energy source. The dependence on fossil fuels and the rapid increase in carbon dioxide emissions put the sustainable development of the global economy at risk [3]. There is a need for a green, clean, and efficient energy carrier, and hydrogen shows promise with its high energy density per unit of weight (120.7 MJ/kg), greater than any other known fuel [4]. Another advantage hydrogen has over fossil fuels is that, since it is synthetic in origin, it lacks the problem of uneven geographical distribution and its geopolitical consequences.

However, compared with other combustible gases, hydrogen has a wide combustible range in air (4-75%vol), a modest lower flammability limit (LML), fast diffusion (0.61 cm^2/s), low minimum ignition energy (0.017 mJ at stoichiometric ratio), and fast flame propagation speed in air (260 cm/s) [5]. Furthermore, the phenomenon of hydrogen embrittlement and the fact that hydrogen leaks easily through vessels or pipeline valves, make hydrogen handling, storage, and distribution risky and accident-prone [3],[5].

Thus, with the growth of the hydrogen economy, the demand for better detection, that is for better sensors, has grown as well. The colourless, odorless and tasteless nature of hydrogen make the development of effective sensors necessary for the development of a green economy. Thus, scientific interest in hydrogen detection has risen over the years, made evident by the increase in the number of publications on this topic as seen in Figure 1.2 [3].

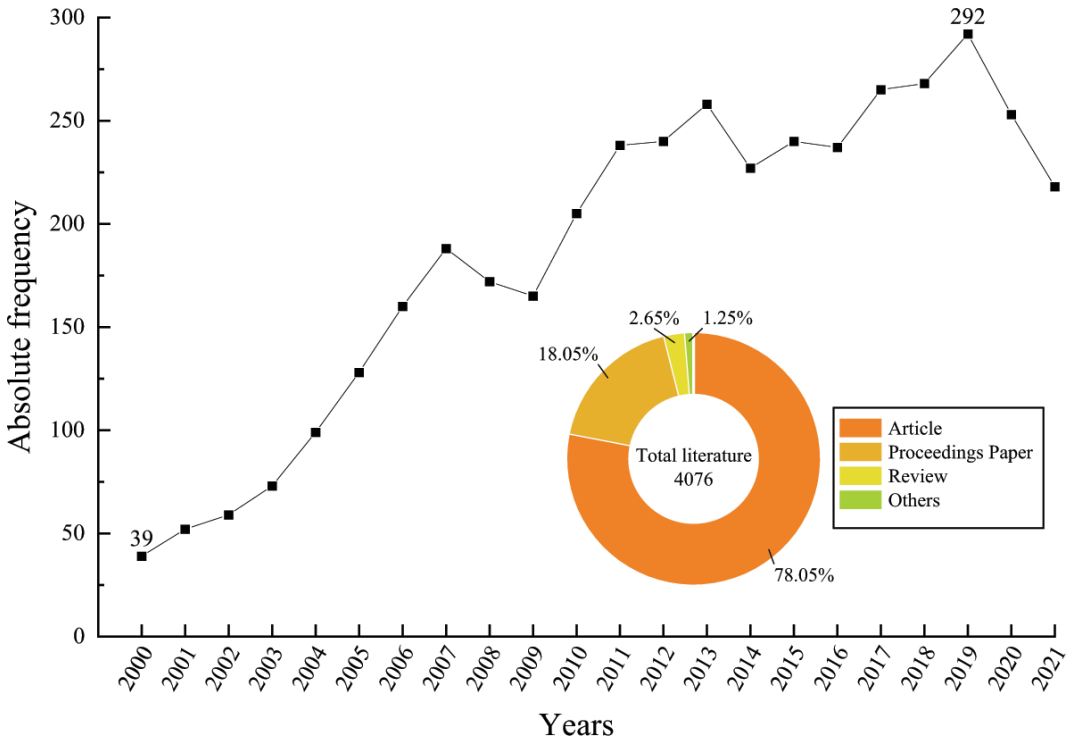

Figure 1.2: Annual distribution of the number of literature and distribution of the type of literature regarding hydrogen detection [3].

1.2 Gas Sensors

The International Union of Pure and Applied Chemistry (IUPAC) defined chemical sensors in 1991: “A chemical sensor is a device that transforms chemical information, ranging from the concentration of a specific sample component to total composition analysis, into an analytically useful signal. The chemical information may originate from a chemical reaction of the analyte or from a physical property of the system investigated” [6]. Most sensors include a detector and a transducer. The role of the detector in a chemical sensor is to react with the analyte, producing some change of physical or chemical properties. A transducer is needed if the changing property is not an electrically measurable quantity. The transducer transforms the change in physical/chemical property into an electrical output signal. The concentration of the gas detected can usually be obtained by measuring the intensity of the electrical signal. [7] If there is no chemical reaction, and the analyte provokes a change in a physical property of the detector, the sensor is called a physical sensor.

1.2.1 Sensing Parameters

Before proceeding with the illustration of the different kinds of gas sensors, it is best to define the main requirements of a chemical sensor.

- Sensitivity: the change of the measured signal per unit of analyte concentration. The slope of the signal intensity vs. concentration curve is then equal to the sensitivity, with more sensitive devices having a steeper slope, and thus being better able to discriminate between small changes in concentration [8].
- Specificity: the ability of the sensor to discriminate between different analytes. This is a particularly critical factor in gas sensors, since large groups of chemicals (for instance, oxidizing or reducing gases) react similarly with the detector, producing similar signals. A sensor with good specificity is able to measure an analyte with little or no interference from the environment [8].
- Stability: the capability of the sensor to reproduce, over time, the same response for the same concentration of analyte. The reproducibility of the signal is thus dependent on the stability of the sensor [8].
- Detection limit: the lowest concentration that the sensor is able to detect [8].
- Dynamic range: the difference between the highest measurable concentration and the detection limit [8].
- Response time: the time occurring between the onset of the signal change due to the presence of the analyte, and the moment in which the signal reaches a certain value. In literature, the response time of a gas sensor is usually given as the time in which the signal reaches 90% of its total change [9].
- Recovery time: the time passing between the moment in which the analyte is no longer present and the moment in which the sensor signal returns within a certain interval of the baseline. Typically, the recovery time of a gas sensor is calculated as the time in which the signal recovers 90% of the variation with respect to the baseline [9].
- Working temperature: the temperature at which the sensor has maximum sensitivity.
- Life cycle: the operational period of the sensor.

The ideal gas sensor must possess high sensitivity, dynamic selectivity, wide detection range, stability, low detection limit as well as fast response [10].

On May 10, 2017, a Hydrogen Sensor Workshop was held in Brussels, Belgium. The workshop was jointly organized by the sensor test laboratories at the Joint Research Centre (Petten, Netherlands) and the National Renewable Energy Laboratory (Golden, Colorado, United States), with assistance from the Fuel Cell and Hydrogen Joint Undertaking. The purpose of the workshop was to bring together stakeholders in the hydrogen community with an interest in hydrogen sensors, with a special focus on the ability of existing hydrogen sensor technology to meet end-user needs in applications for hydrogen as an alternative fuel [11]. The Workshop identified several sensor performance gaps hindering the diffusion of hydrogen technology, as summarized in Table 1.

Metric requirement and Gap Identification	Supplemental Comments	Application
Metrological Metrics		
Lifetime		
10-year life	Replacement cost too high, down time associated with sensor failure	Infrastructure/Automotive
Impact of chemical stressors (poisons)	Harsh chemical environment adversely affecting performance	Infrastructure/Automotive
Impact of physical stressors (T, P, RH)	Harsh chemical environment adversely affecting performance	Infrastructure/Automotive
Accuracy		
Impact of chemical stressors (interferents)	Chemical Interferents may cause false positive or false negative alarms	
Impact of physical stressors (Environment, T, P, RH)	Environmental Interferents may cause false positive or false negative alarms	
Response Time		
General	<2 sec is desired for many applications	Infrastructure/Automotive
Flow-rate Dependence	Impact with quiescent environment vs. dynamic flowing conditions	Infrastructure/Automotive
Exhaust and process control	< 1 sec (300 ms)	Automotive

Deployment Metrics		
Cost and Availability Capital Cost	Need for lower cost	Automotive/Infrastructure
Codes, Standards and Regulations/Directives Issues Standards not always available (gaps)	Complex, costly, and often national requirements	Automotive/Infrastructure
Complex, costly, and often national requirements	Complex, costly, and often national requirements	Automotive/Infrastructure
Operational Metrics		
Cost Maintenance and Calibration	Considered a bigger concern than capital cost; maintenance intervals > 1 year desired	Automotive/Infrastructure
Sensor Placement and Guidance Location/placement of sensor	Dispersion behaviour of hydrogen plumes not fully characterized	Infrastructure
Wide Area Monitoring	No formal guidance on sensor placement is needed	Infrastructure/Research

Table 1.1: high-priority gaps impacting the performance and use of hydrogen sensor [11]

1.2.2 Pellistors

Combustible gases, that is gases that undergo a combustion reaction in air, are detectable by the calorimetric, or *heat-tone*, method. The most common type of calorimetric sensor is the *pellistor,* a portmanteau of pellet and resistor. A typical pellistor is made out of two platinum coils each embedded in a pellet, a porous ceramic bead, usually γ-Al_2O_3. These platinum coils act both as a resistance thermometer and a heater. One of the beads has a surface activated by a noble metal such as Pd, Pt, or Rh, while the other is inactive and acts as a compensating element, so that fluctuations in relative humidity, temperature or thermal conductivity of the analyte gas influence both heads equally, guaranteeing that the output is stable [12]. A current is passed through the platinum coils, heating them up to 500°, which thanks to the catalytically activated surface of the pill is enough to make the analyte gas react [13]. Hydrogen reacts with the adsorbed oxygen on the surface of the pill producing

water. This reaction is exothermic and increases the temperature of the activated pill, changing the resistance of the coil. Since the beads are mounted in a Wheatstone bridge with a downstream DC amplifier, this resistance change causes an imbalance in the circuit which constitutes the sensor signal. Such a sensor is schematized in Figure 1.3.

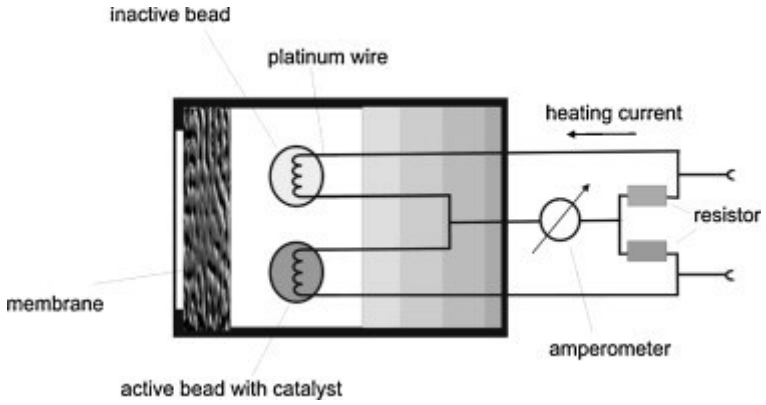

Figure 1.3: scheme of a typical pellistor, from [12]

Pellistors are a widely available technology with a long history, having been commercially available since the 1960's, but present some notable disadvantages, such as their lack of selectivity, due to the fact that every combustible gas can react with the activated pill, making the use of pellistors

not recommended for detecting hydrogen in the presence of interfering gases, for instance hydrocarbons. In the second place, the presence of inhibitors or poisons, chemicals that adsorb reversibly or irreversibly respectively on the surface of the pill, causes a drop in the sensor response, because these substances adsorb more easily than hydrogen, decreasing the number of active sites. Organic silicon and phosphorus containing compounds are some of the most common poisons, while organic halogenides represent a class of inhibitors [12].

1.2.3 Thermal conductivity sensors

Thermal conductivity sensors exploit the high thermal conductivity of hydrogen (0.174 W/mK at 20 °C) compared with air (0.026 W/mK) [12]. Such a sensor is comprised of two thermistors, in contact with the analyte gas and the reference gas, usually air, respectively, both connected to a Wheatstone bridge. When the measuring thermistor is in contact with hydrogen, it loses heat at a faster rate than the reference thermistor, thus reducing its

resistance, which is detected as an imbalance in the Wheatstone bridge. This configuration is depicted in Figure 1.4. More recent variants of thermal conductivity sensors do not need a reference thermistor. Instead, it employs a hot and cold element between which a constant temperature difference is maintained. The heat from the hot to the cold element flows through the monitored gas, and thus the flux changes in the presence of hydrogen. As a consequence, the power required to maintain the temperature difference varies, and this constitutes the measurement of the detector as it depends on the concentration of hydrogen.

Advantages of thermal conductivity sensors include their wide detection range (1-100% H_2) [12], the fact that they can operate in absence of oxygen, their resistance to poisoning since they do not contain catalytic metals and have long operating timelines with small drifts. Disadvantages include their relatively high detection limit, making measurement of highly diluted hydrogen a challenge, and the interference from other highly thermally conductive gases, such as helium, argon, methane or carbon monoxide.

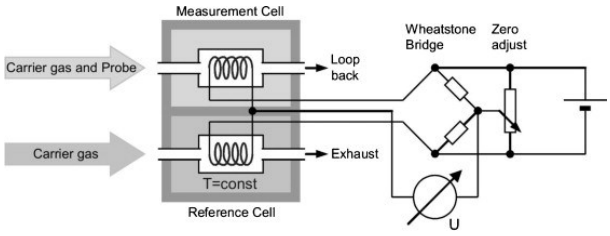

Figure 1.4: a thermal conductivity sensor in Wheatstone bridge configuration, taken from [12]

1.2.4 Electrochemical sensors

Electrochemical gas sensors exploit a redox reaction to detect hydrogen. Charge transfer between a working or sensing electrode and a counter electrode, with electrons passing through an external wire and H^+ ions passing through an electrolyte, constitutes the working principle. Most sensors also include a reference electrode. Operation at low temperature requires a liquid or a polymeric electrolyte, while high temperature applications demand a solid electrolyte. [14] Depending on the type of measurement performed, the sensor can be amperometric, potentiometric or conductometric.

The amperometric sensor is operated under an externally applied voltage, which drives the electrode reaction in one direction, with the potential of the counter electrode maintained constant by a potentiostat, and the electron current is measured. This sensor arrangement is depicted in Figure 1.5. In a potentiometric sensor, the measurement takes place ideally at zero current, and the potential difference between the sensing and reference electrode is registered. Finally, in a conductometric sensor, the change of the conductivity of a liquid electrolyte is registered, exploiting the large conductivity of H^+ compared to other ions. Regardless, the structure of electrochemical gas sensors has several common elements, such as a membrane permeable to the analyte gas, commonly made out of PTFE [13, 14]. The measuring electrode, typically made of gold or platinum, is in contact with the membrane. Sulfuric acid is commonly used as a liquid electrolyte, but the problems of leakage and corrosion must be taken into consideration. A solid polymer electrolyte, such as Nafion®, or ceramics, can solve this issues. The reactions taking place at the measuring electrode and the counter electrode are as follows:

$$H_2 \rightarrow 2H^+ + 2e^- \qquad (1.1)$$

$$1/2O_2 + 2H^+ + 2e^- \rightarrow H_2O \qquad (1.2)$$

The electron current is thus proportional to the concentration of H_2, according to Faraday's law, thus providing a linear response. Electrochemical gas sensors are particularly suitable for use in hand-held measuring devices, since no additional electrical energy is required to operate the sensors, and they tend to be small and light [13]. They also have the favourable characteristics of low power consumption and operation at room temperature [12]. Disadvantages of electrochemical gas sensors include sensor drift due to material degradation and low selectivity to hydrogen compared to other gases.

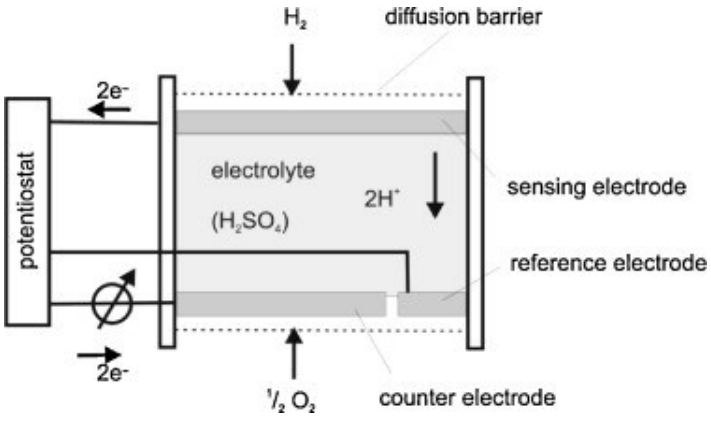

Figure 1.5: an electrochemical sensor in amperometric configuration, from [12]

1.2.4 Metal Oxide Semiconductor Sensors

1.2.4.1 Resistive Sensors

Metal oxide semiconductor (MOS) gas sensors are a widely studied category of devices presenting many advantages in terms of fabrication and application. For a pristine oxide, two main sensing mechanisms are proposed in literature: reduction-reoxidation, also called oxygen vacancy model, and ionosorption [9] [15].

The reduction-reoxidation mechanism can explain how n-type semiconductors respond to hydrogen. Many metal oxides, such as SnO_2, ZnO, and WO_3, are intrinsically n-type semiconductors due to oxygen vacancies in the crystal lattice, with these vacancies acting as electron donors. When exposed to air, the vacancies react with molecular O_2, which is thus chemisorbed on the surface of the oxide, extracting electrons from the conduction band, according to the reaction:

$$2V_{\dot{O}} + O_{2\,(gas)} + 2e^{-}_{(CB)} \rightleftharpoons 2O^{x}_{O} \qquad (1.3)$$

A reducing gas, such as H_2 or CO, can react with the chemisorbed oxygen, releasing electrons back into the conduction band as described below:

$$CO_{(gas)} + O^{x}_{O} \rightleftharpoons CO_{2(gas)} + V^{x}_{O} \qquad (1.4)$$

$$V^{x}_{O} \rightleftharpoons V_{\dot{O}} + e^{-}\ (CB) \qquad (1.5)$$

$$V_{\dot{O}} \rightleftharpoons V_{\ddot{O}} + e^{-}\ \ (CB) \qquad (1.6)$$

According to the ionosorption model, oxygen adsorbs at the oxide surface in a delocalized manner, trapping electrons from the conduction band and forming ions—charged molecular ($O_2^{-}{}_{ads}$) and atomic ($O^{-}{}_{ads}$ and $O^{2-}{}_{ads}$) species—that are electrostatically stabilized at the surface in the vicinity of metal cations [15]. The adsorption thus results in space charge effects such as depletion and accumulation by changing the surface potential.

Reducing gases react with this ionosorbed oxygen, releasing the captured electrons back into the conduction band [9]:

$$O_{2(gas)} \rightleftharpoons O_{2(ads)} \quad (1.7)$$

$$O_{2(gas)} + e^- \rightleftharpoons O_{2(ads)}^- \quad (1.8)$$

$$O_{2(ads)}^- + e^- \rightleftharpoons 2O_{(ads)}^- \quad (1.9)$$

$$O_{(ads)}^- + e^- \rightleftharpoons O_{(ads)}^{2-} \quad (1.10)$$

$$CO_{(ads)} + O_{(ads)}^- \rightleftharpoons CO_2 + e^-(CB) \quad (1.11)$$

Although the exact mechanism is still under debate, the following conclusion can be deduced from the reactions above: the reaction of the semiconductor with oxygen causes band bending, with a length equal to the thickness of the space-charge layer, and the Schottky barrier between two grains increases, reducing the possibility for electrons to contribute to conduction. The ionized oxygen species may react with a reducing gas or may be replaced by a competitive species, which results in a change in the band bending, as shown in Figure 1.6. The space-charge thickness decreases as the number of adsorbed oxygen species decreases, the band bending length decreases, and the Schottky barrier is lowered, making it easier for electrons to move between grains, thus determining an increase in the conductivity for a n-type semiconductor [16].

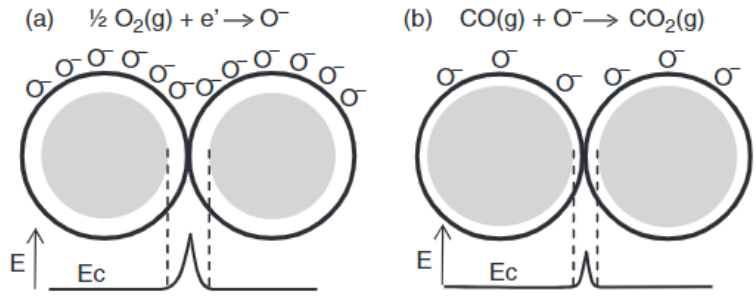

Figure 1.6: the modifications of the band structure of a semiconductor in the presence of oxygen and successively of a reducing gas, taken form [16].

In the presence of an oxidizing gas, an n-type semiconductor instead manifests a decrease in conductivity, since the reaction with the analyte decreases the amount of electrons in the conduction band and heightens the Schotthy barrier between grains. For the same reason, a p-type semiconductor responds in the opposite manner: in the presence of a reducing gas, the electrons injected into the conduction band recombine with holes, which causes a decrease in conductivity since holes are the majority carriers for p-types. When exposed to an oxidizing gas instead, the conductivity of a p-type semiconductor rises as the amount of holes in the valence band is increased. Table 1.2 summarizes the interesting properties of various MOSs for gas sensing.

	Material	Electronic configuration	Band gap (eV)	Crystal structure	Target pollutant	Attractive property for gas sensing
n-type	SnO_2	[Kr] $4d^{10}5s^05p^0$	~3.6	Tetragonal	H_2, CO, NO_2, NH_3, H_2S, SO_2	High chemical sensitivity, good stability, nontoxicity, good heat tolerance, corrosion resistant
	ZnO	[Ar]$3d^{10}$ $4s^0$	~3.37	Wurtzite	H_2, CO, NO_2, NH_3, H_2S	Good thermal and chemical stability, nontoxicity
	TiO_2	[Ar]$3d^04s^0$	3.2/ 3	Anatase/rutile	CO, NO_2	Chemical stability, nontoxicity, high-temperature stability, harsh environment tolerance
	WO_3	[Xe] $4f^{14}5d^06s^0$	2.4–2.8	Monoclinic	H_2, H_2S, NO_2	Presence of W in multiple oxidation states (+2 to +6), rich morphology, and high intrinsic surface area
	In_2O_3	[Kr] $4d^{10}5s^05p^0$	~ 3.7	Cubic/ rhombohedral	CO, NO_2, H_2S	Good stability, good physio-chemical properties
p-type	CuO	[Ar]$3d^94s0$	~ (1.2–1.9)	Monoclinic	CO, NO_2, H_2S, VOCs	Nontoxicity
	NiO	[Ar]$3d^84s^0$	~ (3.6–4)	Rocksalt (NaCl)	NH_3, H_2S	High thermal and chemical stability
	Co_3O_4	[Ar]$3d^{6-7}4s^0$	1.48 and 2.19	Spinel	CO, NO_2, NH_3	Good conductivity and oxidative catalytic capacity
	Cr_2O_3	[Ar]$3d^34s^0$	3.4	Corundum	H_2, NO_2	Thermo dynamical stability and resistance to chemical attack, presence of Cr in multiple oxidation states (+2 to +6)

Table 1.2: properties of metal oxide semiconductor gas sensors, from [9]

Advantages of resistance-based MOS sensors include high sensitivity, fast response, acceptable lifetime, wide operating temperature range, low cost and modest power consumption. Disadvantages include poor selectivity, interference from humidity and temperature, high operating temperature, as the absorption of oxygen is an activated process, contamination, susceptibility to aging and memory effects, and requiring O_2 to operate [12]. Figure 1.7 depicts the structure of a resistance-based MOS gas sensor. The insulation layer is typically Al_2O_3.

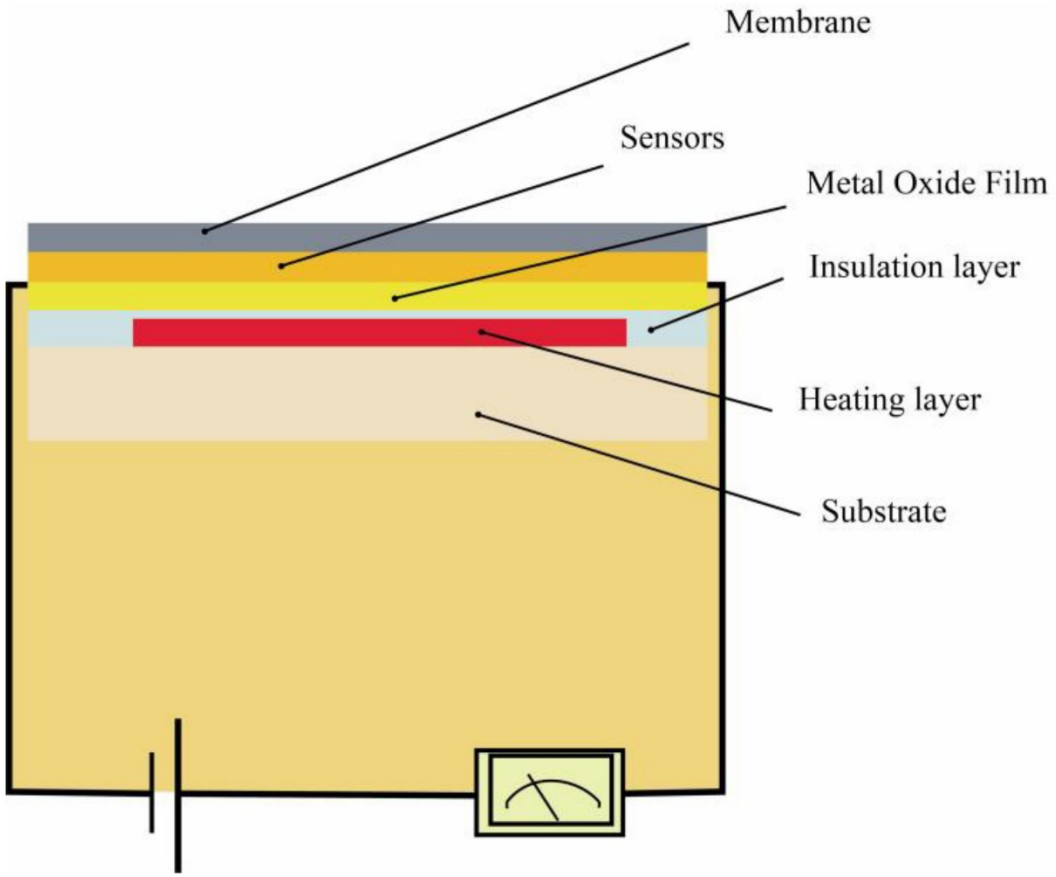

Figure 1.7: Schematic diagram of metal oxide semiconductor-type sensor structure, taken from [17].

1.2.4.2 Schottky Diode Sensors

Non-resistive semiconductor gas sensors can exploit a variety of phenomena to produce a response. Schottky diode-type sensors generally employ a layer of metal (usually Pd or Pt) deposited on the semiconductor material to form a Schottky junction, often with an interposed insulating layer (MIS/MOS). When a metal is brought in contact with a semiconductor the Fermi level of the semiconductor adjusts to and aligns with the Fermi level of the metal by an amount equal to the difference between the two work functions of the two materials (Schottky barrier height). [12] When the metal comes into contact with hydrogen, the hydrogen molecules decompose into hydrogen atoms and diffuse into the metal, accumulating at the metal-insulator interface where they are polarized and create a dipolar layer. This causes a change in the Schottky barrier height, shifting the I-V characteristic curve, and the response can be measured as the change in voltage under constant bias current [17]. Advantages of Schottky diode sensors include their

micromachinability, low cost, small size, and the possibility of mass production. Their main disadvantage is the susceptibility to drift [12].

Metal oxide semiconductor-type field-effect transistor (MOSFET) sensors employ the same influence of hydrogen on the Schottky barrier height, but the device is assembled over a silicon substrate, ion-implanted with a source and a drain, and with a gate formed out of a catalytic metal (Pt or Pd) contacted with SiO_2. The absorption of hydrogen changes the work function of the gate electrode, resulting in a voltage change in the sensor signal. Advantages comprehend fast response, accurate measurements, low influence from ambient parameters, high sensitivity and selectivity, small size and the possibility of mass production. Disadvantages comprehend baseline and hydrogen induced drift, hysteresis of the characteristic curve, and saturation at modest concentrations [12].

1.2.4.3 Optical Sensors

Optical gas sensors are based on the change in optical properties caused by the chemical reaction with the analyte. With respect to sensors based on electrical or electrochemical phenomena, optical sensors have the advantage of a higher resistance, flexibility, and absence of electric contacts and electrical currents, and they are unaffected by electrical and magnetic noise. They are fast, cost effective, and not easily poisoned [16]. The use of optical fibers both as detectors and to transmit the electromagnetic radiation to and from the sensing region provides advantages in terms of miniaturization and cost and allows measurements over large distances or at places where access is difficult. In interferometric measurements, a change in the dimensions or the refractive index of the sensing material produces a change in the phase of light beam, which can be detected by means of interferometry [12]. Another application of optical fiber technology to optical gas sensing is found in reflectivity measurements, in which micromirrors consisting of a thin layer of the sensing material, usually Pd, coated onto the cleaved end of an optical fiber, detect the change in reflectivity of the palladium layer on exposure to hydrogen.

Another phenomenon which has been widely studied as a sensing mechanism for hydrogen is the variation in the Surface Plasmon Resonance (SPR) of the sensing material. [8] This resonance is a coherent oscillation of the surface conduction electrons excited by an electromagnetic radiation. When a surface plasmon is confined to a structure of a size comparable to the wavelength of the incoming light, for example like in the case of Au or Ag

nanoparticles (NPs), metal free electrons participate in the collective oscillation, and a localized surface plasmon resonance (LSPR) is excited. Since these coherent oscillations of metal surface electrons are extremely sensitive to changes in the dielectric properties of the interfacing material, this property can be exploited for developing sensors with high sensitivity. For instance, it has been demonstrated that when TiO2–Au films are exposed to reducing gasses, a blue shift of the Au LSPR peak is induced, as a result of electron injection into the n-type oxide matrix [18].

Another approach to an optical gas sensor is constituted by a gasochromic device. A material is defined as chromic if it exhibits a distinct color change when exposed to an external stimulus, especially when the change is reversible and controllable [19]. We speak of electrochromism when such a color change is due to ion insertion (cathodic electrochromism) or extraction (anodic electrochromism) under an external voltage. A description of electrically induced colour changes in thin films of tungsten oxide immersed in sulfuric acid was given in an internal document at the Balzers AG in Liechtenstein in 1953, proving that WO_3 was the first electrochromic material ever discovered. We defined gasochromism as the change in color provoked by reaction with a gas. There has been much interest in the gasochromic properties of WO_3 in recent years, as the following Chapter will discuss. Other gasocromic materials include MoO_3 and V_2O_5. In general, a gasochromic gas sensor uses as a measurand the change in transmittance (or absorbance) when the sensor is exposed to the target gas. This has the advantage of being a simple, versatile approach, requiring relatively low temperatures when compared to conductometric devices, and being easily integrable with optical technologies.

Chapter 2: Gas Sensing Materials

In this chapter, the materials employed in this work are discussed. Section 2.1 presents the general properties of WO_3, its gas sensing mechanism, and its sol-gel synthesis. Section 2.2 describes noble metal functionalization, with a focus on platinum nanoparticles and their synthesis. Section 2.3 deals with ZnO, its properties, and its sol-gel synthesis. Section 2.4 presents $ZnWO_4$ as a material and proposes some examples of gas sensors in which $ZnWO_4$ is combined with the materials described earlier.

2.1 WO_3

WO_3 is a transition metal oxide which has received great attention over the years due to its electro-optical, electrochromic, ferroelectric, catalytic and sensing properties [20]. WO_3 thin films have recently attracted a lot of attention for applications in optoelectronics, photovoltaics, lithium-ion batteries, microelectronics, sensors, superconductivity, ferroelectrics, storage devices and porosity for electrochromism. Besides the above-mentioned applications, WO_3 thin films-based electrochromic devices are currently employed in sunglasses, sunroofs of the automobile, rearview mirrors, and tunable tinted glass for automotive and buildings windows for optical modulation purpose [21].

At atmospheric pressure, WO3 is known to form five different phases: monoclinic II (ε-WO3), triclinic (δ-WO3), monoclinic I (γ-WO3), orthorhombic (β-WO3), tetragonal (α-WO3), and cubic WO3. [22] Such phases are characterized by corner- and edge-sharing amongst WO_6 octahedra. Figure 2.1 shows these crystal structures projected along the three main crystallographic axes, along with their space group in Hermann-Maguin notation and the corresponding phase transition temperatures. Note that as temperature increases, the crystal structure becomes more resembling of the ideal cubic ReO_3 structure, that is a defective perovskite-type structure lacking the central atom in 12-fold cubooctahedral coordination [23]. At room temperature, monoclinic γ-WO3 has been reported as the most

stable phase. This phase presents lattice constants *a*=7.306 Å, *b*=7.540 Å, *c*=7.692 Å, β=90.881° [24].

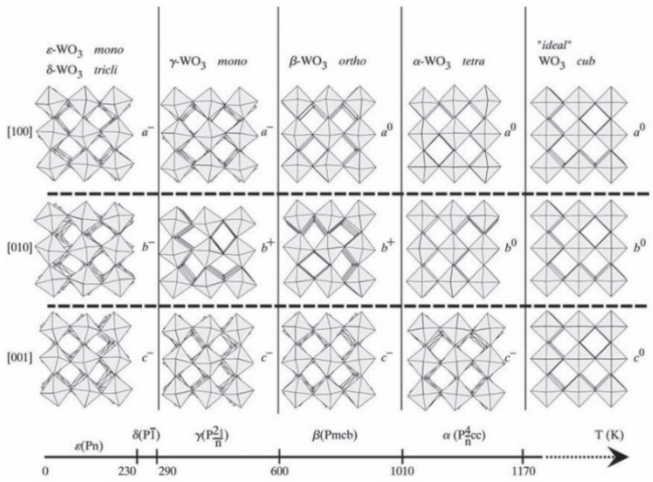

Figure 2.1: the five phases of WO_3, from [22]

WO_3 is well-known for its nonstoichiometric properties, as the lattice can withstand a considerable amount of oxygen deficiency [25]. Due to these oxygen vacancies, WO_3 is a wide-band gap n-type semiconductor, with amorphous WO_3 being reported as having an Energy Gap E_g = 3.25 eV [24], while monoclinic crystalline γ-WO_3 having E_g = 2.62 eV [20]. The valence band is formed from the combination of filled O 2p orbitals, whereas empty W 5d orbitals contribute to the formation of the conduction band. Morphology strongly influences the band gap value, as it has been shown that E_g decreases with increasing grain size [26]. A widely accepted explanation of this dependency relies on quantum confinement effects [27].

The optical properties of WO_3 are dominated by its absorption threshold, which is in turn determined by its bandgap. Pristine, stoichiometric WO3 is transparent to visible light, with a slight yellow tint in samples with smaller bandgap, evidencing absorption in the blue range [28]. For photon energy hv > E_g, the absorption coefficient α can be modeled according to

$$\alpha h\nu = K(h\nu - \mathrm{Eg})^{\frac{1}{r}} \qquad (2.1)$$

With r = ½ since WO_3 is an indirect band gap semiconductor [28]. It is also worth noting that WO_3 thin films have quite the large refractive index, with value ranging from 1.9 to 2.6 [29].

2.1.1 WO_3 Gas Sensing Mechanisms

A lot of interest regarding WO_3 has revolved around its chromism, being a cathodic electrochromic material [30]. Due to its large lattice parameters, small ions such as H^+ or Li^+ are easily and reversibily intercalated into WO3. H^+ insertion causes the formation of Tungsten bronze HWO_3 according to the simplified reaction:

$$[WO_3 + H^+ + e^-]_{bleached} \rightleftharpoons [HWO_3]_{coloured} \quad (2.2)$$

The bleaching process in particular can take different pathways:

$$H_xWO_3 + \frac{x}{4}\,O_2 \xrightarrow[Oxidation]{} \frac{x}{2}\,H_2O + WO_3 \quad (2.3)$$

$$H_xWO_3 \xrightarrow[Decomposition]{} \frac{x}{2}\,H_2 + WO_3 \quad (2.4)$$

$$H_xWO_3 \xrightarrow[Disproportionation]{} \frac{x}{2}\,H_2O + WO_{3-\frac{x}{2}} \quad (2.5)$$

According to [31], the decomposition takes place at 176°, while the disproportionation at 336°. This makes oxidation the only available bleaching pathway at room temperature. When the intercalation of H^+ is due to the dissociative chemisorption of H_2 and subsequent spill-over of protons into the WO_3 lattice, we speak of gasochromism [32]. This is a redox reaction, in which tungsten is reduced from W^{6+} to W^{5+}. Orel et al. [32] proved that, in mesoporous nanocrystalline monoclinic WO3 impregnated with Pt, the injection of H^+ causes the reversible formation of tetragonal H_xWO_3, as evidenced by the increase of the intensity of the IR-active stretching modes of terminal groups $W{=}O_t$ at 970 cm^{-1} and the decrease of the intensity of the IR-active W-O-W corner-sharing stretch mode at 635 cm^{-1}, respectively meaning that the number of terminal $W{=}O_t$ increases and that W-O-W bonds are broken, decreasing the number of corner-sharing octahedra. This allowed them to propose the mechanism for the coloring and bleaching reactions illustrated in Figure 2.2. The authors explain the strong and broad absorption peaks present in the spectra of amorphous colored films trough the small polaron theory [33], in which the hopping of electrons from W^{5+} to an adjacent W^{6+} gives rise to a broad absorption peak around ~1000 cm^{-1} and thus to the blue coloration. This hopping of electrons is accompanied by a

reversible change of coordination around W^{5+} and W^{6+} in amorphous films, contrasting with the formation of t- H_xWO_3 in crystalline films.

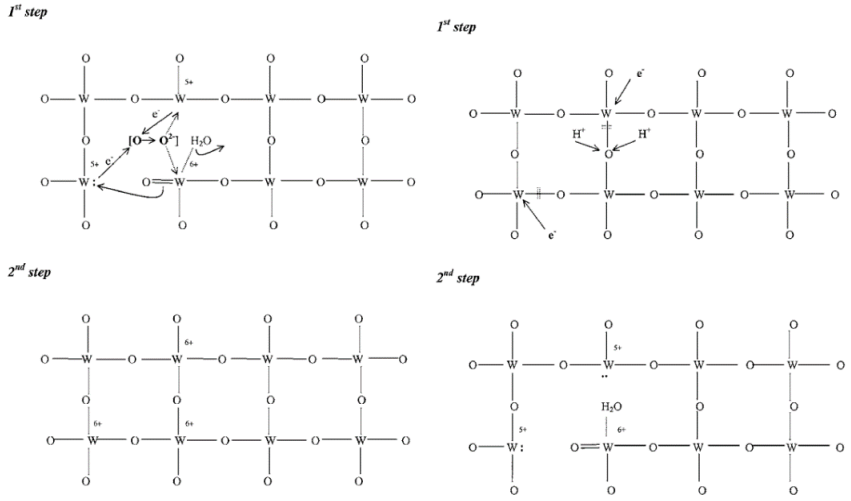

Figure 2.2: bleaching (left) and coloring (right) mechanisms as proposed in [32].

2.1.2 Sol-gel synthesis of WO_3

Several precursors for WO_3 sol-gels have been investigated in literature, such as sodium tungstate Na_2WO_4, ammonium paratungstate ($(NH_4)_{10}W_{12}O_{41}$•$5H_2O$), tungsten chloride (WCl_6), and metallic tungsten powder [16]. Out of these, metallic powder presents the advantage of non-volatility, non-acidity and low toxicity.

Yang and coworkers have discussed in detail the mechanism of tungsten powder dissolution during the course of WO_3 network formation, as depicted in Figure 2.3. H_2O_2 adsorbs on the surface of the powder triggering the redox reaction and the catalytic decomposition of H_2O_2. The dissolved tungsten (mostly W(VI)) forms W(O2) complex with H_2O_2. These complexes can catalyze the solution reactions, which are typical Haber-Weiss peroxide chain breakdown between H_2O_2 and W(VI)/W(V) redox couple [34].

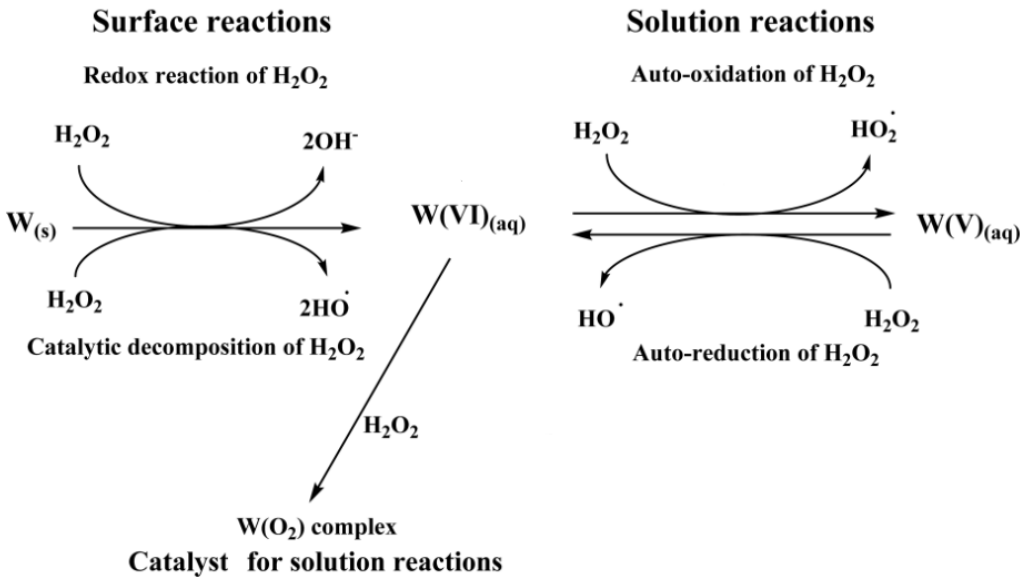

Figure 2.3: the dissolution reactions between H_2O_2 and W powder, modified from [34]

Stefan et al. [35] argue that the dissolved powder then forms peroxo-tungstic acid (PTA), according to reaction (3.1):

$$W \xrightarrow{H_2O_2} H_2WO_5 \xrightarrow[-\frac{1}{2}O_2]{-H_2O} WO_3 \qquad (3.1)$$

The formation of PTA precursors mainly depends on the degree of the decomposition of the excess of H_2O_2 in the solution, the atmospheric humidity during the condensation process and the condensation rate. Thermal analysis shows that the thermal decomposition of PTA precursor is finalized at about 550ºC [35]. X-ray diffraction patterns of WO3 thin films produced by Hemati and coworkers [36] annealed at 300 and 400 °C are shown in Figure 2.4. As the figure shows, at a temperature of 300°C, the film is amorphous, whilst the monoclinic phase is formed after annealing at 400°C.

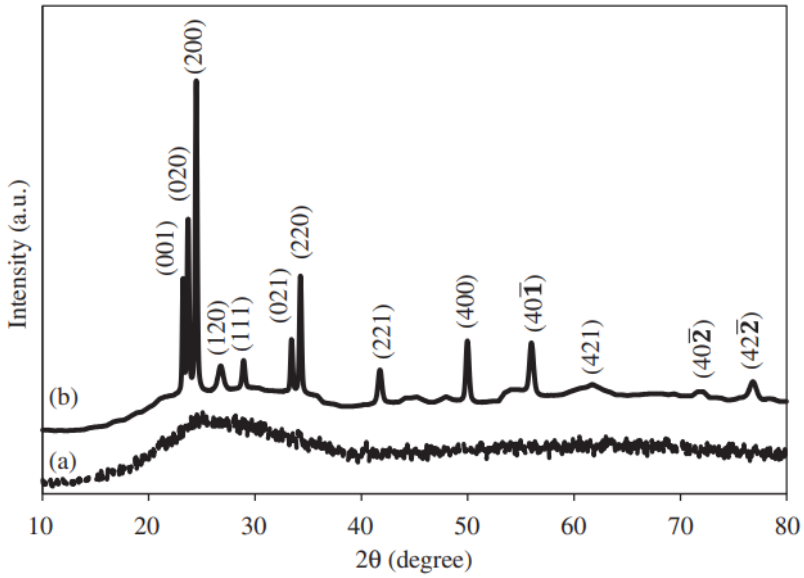

Figure 2.4: XRD patterns of WO3 thin films annealed at (a) 300° and (b) 400°, from [36].

2.2 Noble Metal Functionalization

As mentioned above, noble metal functionalization is essential to improve the sensing capability of metal oxide semiconductor sensors. Several synthetic approaches leading to morphologically different functionalization have been studied, such as thin film deposition [37], impregnation [32, 35], and nanoparticle deposition [18, 36]. In general, it can be said that the addition of a noble metal increases sensitivity, lowers the working temperature, and improves the response and recovery time [40].

Depending on the exact nature of the metal and the semiconducting oxide considered, two mechanisms have been proposed to explain the promoting effects of noble metal functionalization, represented in Figure 2.5: chemical functionalization and electronic functionalization. In the first case, the target gas is chemisorbed dissociatively, the activated fragments diffuse along the metal surface, and spill-over to the semiconductor surface to react with the chemisorbed Oxygen. Thus, the gas sensing reaction takes place at the surface of the semiconductor, and the contribution of the metal to gas sensing enhancement is due to its catalytic properties [40]. Such is the case for the interaction of Hydrogen gas with Platinum. In the second case, there is an electron transfer from the semiconductor conduction band to the metal due to work function mismatch, generating a Schottky barrier and increasing the thickness of the electron depletion layer. Upon exposure to Oxygen, the metal is oxidized, and reaction with a reducing gas removes the Oxygen bound to the metal,

releasing the electrons back into the semiconductor [41]. In this case, the conduction properties of the metal and its corresponding oxide enhance the sensor sensitivity and response. This mechanism has been proven for systems such as Ag_2O-SnO_2, PdO-SnO_2, CuO-SnO_2 [40].

Figure 2.5: schematic representation of chemical (left) and electronic (right) functionalization, taken from [40].

As anticipated, Platinum is well suited for Hydrogen detection, since H_2 spontaneously adsorbs dissociatively on Platinum surfaces with remarkable adsorption energy (E_{ads} ~ 0.7-0.8 eV) [42] and good kinetics, with the rate of hydrogen adsorption about 10 thousand faster on platinum than on palladium [43]. Being a surphace reaction, its topochemistry has been widely studied, in order to determine which crystal plane is most suitable for Hydrogen adsorption. It has been proved that the heat of adsorption of H_2 on Platinum increases with respect to the crystal plane in the order (110) < (111) < (100) [44], and that the underpotential deposition rate is higher for (111) and (110) planes than for polycristalline samples, which in turn is higher than the rate for (100)-oriented samples [45].

Xi and coworkers have demonstrated, trough density functional theory calculations, that, after dissociative adsorption on Platinum catalyst, the H atoms migrate to a terminal oxygen on the WO_3 surface, (001) according to their hypothesis. Then, it migrates to another in-plane oxygen and diffuses across the surface or is inserted into the lattice. According to them, H migration from an oxygen to its underneath neighbour can be facilitated catalytically by water, which bridges two separated O atoms to mediate proton exchange. Furthermore, they prove that H easily diffuses through bulk WO_3 with an activation energy lower than 0.23 eV, and that H_xWO_3 is metallic [46].

2.2.1 Synthesis of Platinum Nanoparticles

It is evident then that establishing morphology control is indispensable to optimize the performance of Pt-activated gas sensors. Herricks and coworkers [47] studied the role of $NaNO_3$ as a shape-directing reagent in the polyol synthesis of Platinum nanoparticles; they proved that the nanoparticles obtained without $NaNO_3$ are small and irregular in shape, lacking well-defined crystal facets, whereas with increasing concentration of $NaNO_3$ the nanoparticles were found to possess well-defined octahedral and tetrahedral shapes, with preferential growth along the ⟨111⟩ and ⟨100⟩ directions. They justify this trough Chernov's theory [48], which discusses the competition between adsorption and surface diffusion in the kinetics of crystal facet growth. If surface diffusion is fast, adsorption is the rate-determining step, and any ridge forming on the particle surface has the same supersaturation than any other point on the surface, therefore it is not favored and the particle will grow according to its surface kinetics, without changing its shape over time. Instead, when adsorption is faster than surface diffusion, a ridge will experience higher supersaturation at its top than at its base, since supersaturation increases with distance from the center of the particle, and thus edges and corners are favored to grow. These two cases correspond to the particles synthesized under low and high concentration of $NaNO_3$ respectively.

In other studies [49], [50], $AgNO_3$ has been used as a shape-directing reagent, resulting in NPs with cubic and octahedral shapes, with a predominant (111) orientation. Tsuji et al. [51] showed that PVP molecules, beyond their obvious role as dispersant, play an important role in controlling the morphologies of the branch-like Pt nanoparticles. Their explanation of the influence of PVP involves co-operative kinetic adsorption and desorption of PVP molecules and various anions on particle surfaces that influence the growth of Pt nanoparticles, leading to the evolution of branched Pt agglomerates once again due to the difference between growth rates along various crystallographic directions of fcc Pt.

Chen and coworkers [52] studied the influence of atmosphere on the reduction kinetics in the formation of Platinum nanoparticles. They found that under a nitrogen atmosphere, star-shaped nanoparticles were produced over a period of 1 h, while in air the reaction proceeded at a much slower rate and the nanostructures became more branched and subsequently assembled into submicrometer-sized agglomerates. In agreement with [47], they conclude that if the reduction proceeded too quickly with high supersaturation, only isotropic, spherical

Pt nanoparticles were produced, while if the reduction was slowed by air, the low supersaturation favored the growth along the ⟨111⟩ direction. It is fundamental to maintain all solutions under inert atmosphere during the synthesis, to prevent oxidation of Pt to PtO and the agglomeration of nanoparticles [52].

The polyol, usually some ether glycol or a 1,2-diol, acts both as a solvent of the solid precursor and as a reducing agent [53]. The polyol medium offers several other advantages: its high boiling point (197.6° at room pressure [54]) allows syntheses at relatively high temperature, ensuring that well-crystallized materials are obtained; it protects the as-prepared metal particles from oxidation; its ability to coordinate metal precursors as well as the particle surface minimizes coalescence; the high viscosity of the medium favours a diffusion-controlled regime for particle growth, resulting in controlled structures and morphologies.

It is well-known that the formation of equally charged NP stabilizes suspensions via repulsive electrostatic forces. For this reason, lowering the electrostatic potential at the particle surface leads to a destabilization of colloids. This can be induced by the addition of ions, which can be adsorbed to the particle surface and compensate their charge. According to Chen and coworkers [55], NaCl helps improve the yield by neutralizing the surface charge to make the majority of the Pt NP precipitate.

2.3 ZnO

Zinc oxide has been seen as a promising material for thin film optoelectronic, piezoelectronic, transparent electronic, spintronic, sensing, and photovoltaic devices [56]. It has even had application for antibacterial treatments, sunscreen lotions, catalysis andphotocatalysis. ZnO is also used as an additive in ever-increasing number of industrial products such as paint, rubber, cosmetics and coatings [57]. ZnO crystallizes at room pressure in the hexagonal (wurtzite) structure, shown in Figure 2.6, with a = 3.25 Å and c = 5.12 Å and belongs to the space group C^4_{6v} in the Schoenflies notation and $P6_3mc$ in the Hermann–Mauguin notation. The wurtzite structure is made out of two superimposed hexagonal close packed (hcp) sub lattices of Zn^{2+} cations and O^{2-} anions, shifted with respect to each other along the three-fold c-axis. Because of this, it presents a polar plane, (0001). From another point of view, each Zn^{2+} is tetrahedrally coordinated by four O^{2-}, and

vice versa. It transits to the rock-salt structure at about 9 GPa [58]. ZnO can also present a metastable blende structure which can be stabilized only by heteroepitaxial growth on cubic substrates [59].

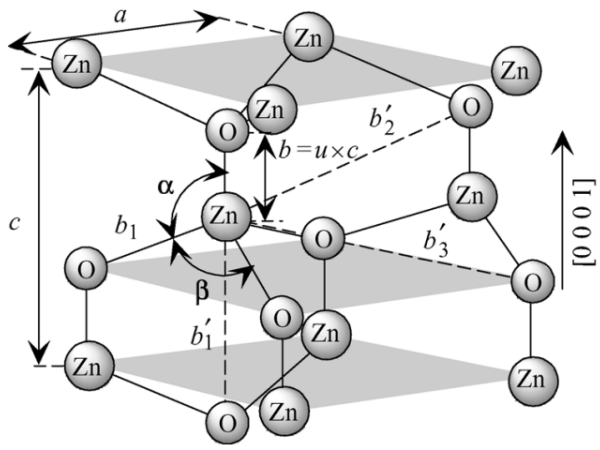

Figure 2.6: the wurtzite structure of ZnO, taken from [59]

ZnO has a refractive index equal to 2.01, and its high exciton binding energy of 60 meV makes it one of the most encouraging photonic materials in the blue-UV region [57]. ZnO-based gas sensors are broadly employed in various applications due to their excellent sensing response, good selectivity, easy fabrication, low cost, good thermal and chemical stability, and non-toxicity. ZnO is intrinsically a II-IV semiconductor showing n-type conductivity due to point defects such as oxygen vacancies and hydrogen multicenter bonds in its crystal lattice [16] [60], [61] with high carrier mobilities in the range of 100 $cm^{2/}Vs$ [56]. It has a direct band gap of 3.37 eV (r=2 in eq. (2.1)). Its conductometric gas sensing mechanism for reducing gases is based on the reaction of the analyte with adsorbed oxygen and the consequent release of electrons into the conduction band causing a resistance decrease, as typical for an n-type semiconductor. It has been used as an active material for the detection of several gaseous species such as oxygen, CO, hydrogen, ammonia, and a wide range of volatile organic compounds. One especially important property of ZnO with regards to H_2 sensing is the diffusion barrier for H atoms, as low as 0.20-0.50 eV [62]. Nonetheless, ZnO-based sensors usually suffer from poor selectivity and long-term instability due to reaction with moisture and CO2 under normal ambient conditions [61].

2.3.1 Sol-gel synthesis of ZnO

Typical ZnO thin film precursors for solution-based techniques include zinc sulfate, zinc nitrate, zinc chloride and zinc acetate [16]. The use of metal salt precursors containing inorganic counterions in non-aqueous media carries the problem of removing the anion from the film, while organic counterions such as acetate offer the advantage of producing volatile by-products upon sol pyrolysis [63]. A second problem that presents itself the temperature stability of the metal salt wherein a higher decomposition temperature is desirable in order to balance the thermodynamics and kinetics of grain growth [64]. Elevated annealing temperatures of 450°C to 600°C are typically used to simultaneously pyrolyze the precursor and induce high crystallinity, grain growth and film texture. Therefore $Zn(NO_3)_2$, which pyrolyzes at a relatively low temperature of 150°C induces rough, dendritic growth due to the combination of high driving force and kinetic limitations. Instead ZAD, which pyrolyzes at a higher temperature and undergoes polycondensation processes, results in smooth, uniform, non-dendritic films [65]. Hence, ZnO films synthetized from ZAD have demonstrated superior electrical and optical performance [66].

The formation mechanism of ZnO suggests that ZnO colloids or gels are formed by the polymerization of zinc hydroxide and/or zinc-oxo acetate clusters from ZnO precursors [67], [68]. Gómez-Núñez et al. [69] have studied the thermal decomposition of the acetate ligands and ethanolamine (EA), which they used in place of diethanolamine (DEA), trough IR spectroscopy. As can be seen from Figure 2.7, the intensities of the bands due to the acetate ligands (the asymmetric and symmetric stretching modes of the bridging ligands at ca. 1580 and 1400 cm^{-1}) decrease, whereas those related to EA (the C–N and C–O groups due to the –NH2 and –OR moieties in the 1100–900 cm^{-1} range, and the wagging mode of – NH2 groups bound to transition metals around 680 cm^{-1}) almost vanish. Moreover, the intense double band appearing below 600 cm^{-1} indicates the presence of ZnO. These findings suggest that the initial step of the decomposition starts between 570 K and 670 K and it involves the cleavage of the Zn–N bond of the deprotonated EA, as depicted in Figure 2.8.

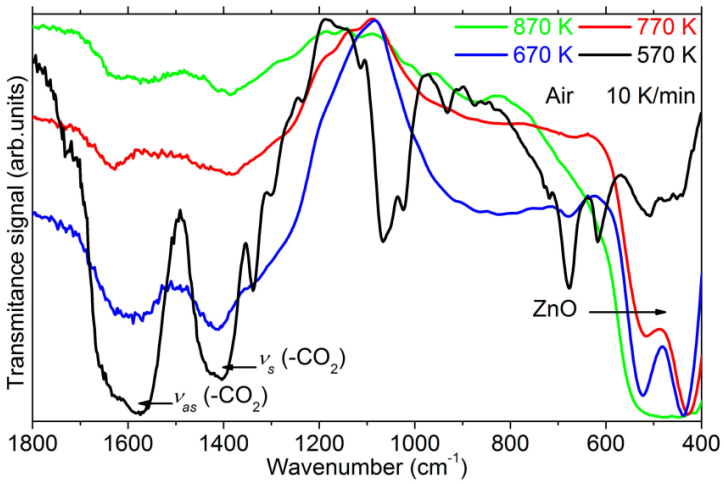

Figure 2.7: IR study of the evolution of a ZnO sol with increasing temperature, taken from [69]

Coupling their experiments with Molecular Dynamics simulations, they verify that the Zn–O(EA) bond length does not change significantly up to 770 K, while the Zn–N bond elongates, further proof that the first step of the reaction is the cleaving of the Zn–N bond. Due to the key role of the H atoms bound to amino groups and the intermolecular N–H···O interactions in intermediate species, they argue that changes in the backbones of aminoalcohols derived from EA may modify the charges of the heteroatoms or induce significant steric effects, which could affect the stability of species and transition states formed in the initial steps of the thermal decomposition. DEA, having more steric encumbrance than EA, may thus favor faster kinetics.

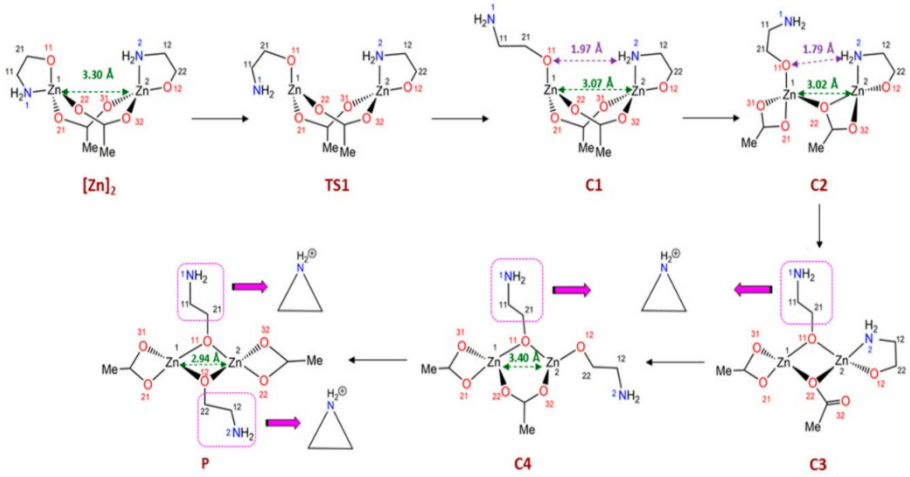

Figure 2.8: The mechanism for the release of N and the formation of the ZnO network, as proposed in [69].

The solvent seems to influence the quality of the films too: Benramache et al. [70] have demonstrated that the crystallinity of ZnO thin films improved when prepared from an ethanol solution instead of a methanol one, justifying our choice of solvent.

It has been argued [71] that the increase in pH of the sols due to addition of an ethanolamine results in the growth of ZnO film with improved preferred orientation along the (002) plane, smooth microstructure, large grain size and low surface roughness, giving ZnO films with low concentration of defects. Nehmann et al. [72] proposed that the Zn–diethanolamine complex Zn(DEA) is formed as a ZnO precursor by ligand exchange reaction between $Zn(OAc)_2$ and H_2DEA, as shown in Figure 2.9. Hayami and coworkers [73], trough TG-DTA and FT-IR investigations, determined that $Zn(OAc)_2(H_2DEA)$ decomposes at 140 °C. At 270 °C, most of the H_2DEA is removed and μ_4-oxozinc compounds were formed. After heating at 420 °C, the acetato groups burned to form hydroxide functionalities. At 500 °C, ZnO was formed. The ZnO film formed from $Zn(OAc)_2(H_2DEA)$ showed high transparency (>90%) and a hexagonal wurtzite structure, with densely packed particles showing a size of ~40 nm.

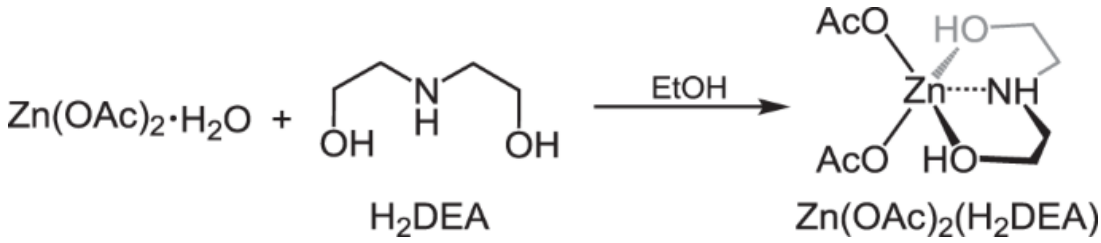

Figure 2.9: The reaction of ZAD with DEA, from [73]

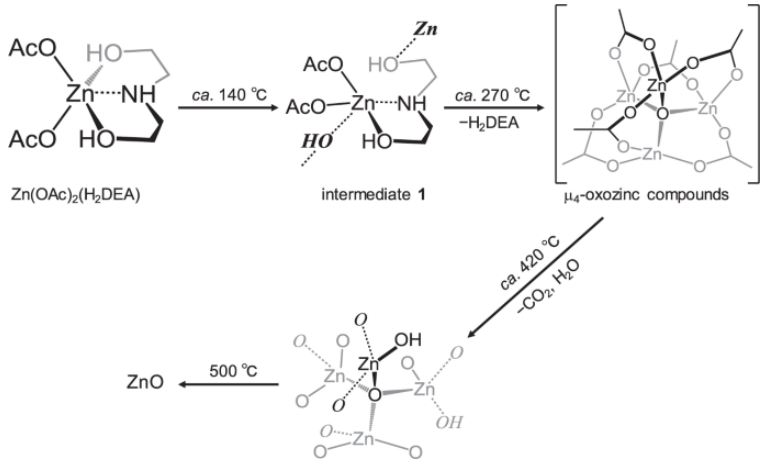

Figure 2.10: A possible pathway for the formation of a ZnO network by decomposition of $Zn(OAc)_2(H_2DEA)$, proposed in [73]

The study by Najafidoust and coworkers [74] revealed that with increasing DEA concentration crystalline size and XRD peak intensity of ZnO decreased. They also showed that the mole ratio of DEA had a great role in the ZnO coatings roughness: the sample with mole ratio 1 of DEA had better surface roughness, uniform morphology and absence of cracks with respect to the sample with mole ratio 2. Increasing the mole ratio of DEA decreased the crystalline and particle size, with detrimental effects on the photocatalysis of blue methylene. This is why we chose to use a mole ratio approximately equal to 1.

Different types of ZnO morphologies and nanostructures can be achieved by using different synthethic methods. Thin films, nanoplates, nanospheres, nanowires, nanorods, nanotubes, nanoflowers, nanofibers, nanoneedles, and nanoribbons [60]. Morphologies with high surface area typically show improved sensing performances with respect to massive ZnO. The sensing response can be also enhanced via metal doping into ZnO, functionalization of noble metal nanoparticles on ZnO surface, inclusion of carbonaceous nanostructures, composition of different MOx nanostructures, UV activation, and e-beam irradiation.

2.3.2 ZnO Sensors

Kim et al. [75] synthesized ZnO nanowires functionalized with Pt and Pd nanoparticles via sputtering, and demonstrated that the oxidation of benzene and toluene with adsorbed oxygen is enhanced owing to the catalytic activities of Pd and Pt. Furthermore, the relative values of the work functions indicate that electrons would flow from ZnO to the noble metal, which results in the formation of Schottky barriers at the heterojunctions between ZnO and metal. A depletion region will be generated with an increase of resistance, and the injection of electrons upon reaction with the chemisorbed oxygen will thus produce a greater resistance variation, enhancing the sensor response. So, according to the above presented theory, it can be argued that both chemical and electronic functionalizations take place.

One interesting application of ZnO for optical H_2 sensing can be found in [76]. In this work, Nie et al. synthesized via colloidal template method a mesoporous ZnO/WO_3 film, which then they loaded with Pt nanoparticles by sputtering. They studied the dependence of the optical sensing parameters on the Zn/W ratio, and found that,in the sensor with composition $(ZnO)_{0.1}(WO_3)_{0.9}$ the average grain size was as low as half that in pure WO_3 films, and corresponding to this a minimum coloring response time-was found (23.0s against 66.3s for pure WO_3). Furthermore, the $(ZnO)_{0.1}(WO_3)_{0.9}$ film showed good stability after 100 cycles,

while pure WO_3 showed a loss of 2.5% of transmittance variation after the same number of cycles. They attribute the better performance to the easier diffusion of H atoms into ZnO with respect to WO_3, and to the grain refinement effect which, by increasing the available oxide surface, improves the kinetics of adsorption.

In a similar work, Lei et al. [77] obtained an ordered two-dimensional nanoporous conductometric composite ZnO/WO_3 sensor for volatile organic components via a sacrificial template-based method that allowed them control over the composition of the film. They argue that the long-range order in the honeycomb-like film greatly improves the gas sensing properties in terms of sensitivity, response, recovery, and stability. Among the various different molar ratios they experimented with, they found that 5% ZnO/WO_3 shows the best characteristics over all temperature ranges. It is interesting to note that they found $ZnWO_4$ appearing in the 10% ZnO/WO_3 sample. In their opinion, the improved performance of composite films with respect to pure WO_3 is due to the abundant n-n heterojunctions with thick depletion layers that are formed between the grains of ZnO and WO_3 and improved O_2 adsorption, causing an increase in resistance when exposed to oxygen and thus a greater resistance decreases upon exposure to reducing gases.

In conclusion, from the above cited literature it is evident that gas sensing properties can be greatly improved via control of morphology increasing the available reactive surface and the thickness of charge depletion layers, and facilitating diffusion of H atoms into the oxide lattice. The addition of metallic nanoparticles improves the kinetics of adsorption.

2.4 $ZnWO_4$

Zinc tungstate, $ZnWO_4$, is one of the most intensively studied materials among wolframate-type tungstates of interest. Since the discovery of its unique luminescence properties of zinc tungstate by Kröger in 1948 [78], $ZnWO_4$ has been extensively studied as a potential material for optical fibers, scintillators, or heterogenepous catalysts [79], [80], [81], [82], [83]. Furthermore, $ZnWO_4$ has intrinsic photocatalytic activity [84], [85], [86], which is similar to that of ZnO [87], [88].

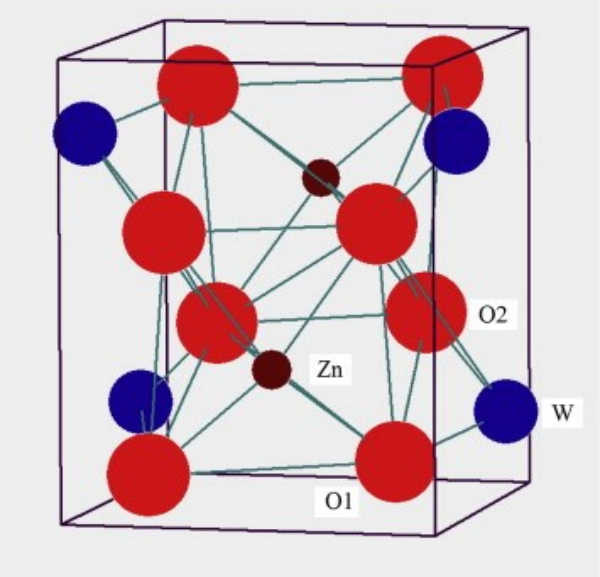

Figure 2.11: the crystal structure of $ZnWO_4$, from [88]

$ZnWO_4$ crystallizes in a monoclinic wolframite-type structure (P2/c space group, with *a* = 4.69263 Å, *b* = 5.72129 Å, *c* = 4.92805 Å, β = 90.6321° [89], depicted in Figure 2.11. In this crystalline structure there are two formula units per primitive cell. The existence of two non-equivalent positions for oxygen atoms (labelled as O1 and O2) is characteristic of the structure of $ZnWO_4$. There are two tungsten atoms and one zinc atom in the nearest arrangement of the O1 atoms, whilst one tungsten atom and two zinc atoms are among the nearest neighbours of the O2 atoms [89]. Six oxygen atoms surround every zinc and tungsten atom, forming distorted ZnO_6 and WO_6 octahedra.

The top of its valence band mainly consists of contributions from the O 2p orbitals while in the bottom of the conduction band predominates the contribution from the W 5d orbitals. The electronic excitations from O 2p to W 5d states are responsible for the optical absorption edge [88], [90]. Its band gap has been estimated to have a value of 3.15-3.52 eV for nanorods and nanoparticles and increasing with the temperature during the synthesis [91], 3.9–4.4 eV as a single crystal [92], or 4.01 eV for porous films [93], and it has been proven that functionalization with platinum nanoparticles decreases the band gap [94]. It is reported that it's a direct band-gap semiconductor, having r = 2 in eq. (2.1) [93]. It has a high work function, having been measured as high as 6.58 eV in a nanorod morphology obtained by hydrothermal synthesis [94], or as low as 4.18 eV when synthesized via a low temperature solvothermal route resulting in large, irregular particles [95]. There is still ongoing debate regarding whether $ZnWO_4$ is a p-type [94] or an n-type [95] semiconductor.

2.4.1 $ZnWO_4$ Sensors

ZnWO4 has proven itself as a promising material for H_2 sensors, showing improved sensitivity and selectivity when functionalized with platinum nanoparticles [94]. Li and coworkers have shown that when a Pt-$ZnWO_4$ sensor was exposed to H_2 or C_2H_5OH gas, some H_2 or C2H5OH molecules absorbed to the surface to the surface of $ZnWO_4$ and then reacted with the $O_2^{-\cdot}$ ions They argue that these interactions can release a large number of free electrons to neutralize the holes, which leads to a reduction in the amount of majority carriers in $ZnWO_4$ nanorods and then gives rise to an increase in the electric resistance of the sensor.

Hu et al. fabricated via thermal decomposition core-shell-type $ZnWO_4/WO_3$ heterostructures [96] They argue that, when $ZnWO_4$, which they consider a n-type semiconductor with work function = 4.7 eV and band gap ∼ 3.3 eV and n-type WO_3 with work function = 5.7 eV and band gap ∼ 2.7 eV are assembled together n-n heterojunctions are formed, having a calculated band gap of about 2.4 eV, which is lower than that of pure WO_3. They explain this via induction by $ZnWO_4$ of electronic states in the band-gap of WO_3. They add that oxygen vacancies in the material also contribute to the active site in the gas-sensing reaction by embedding the defect energy level into the band gap to promote the excitation of free electrons and then supplying more electrons to participate in the reaction. When zinc is introduced into the system, some will replace W^{6+} in the WO_3 lattice, resulting in more oxygen vacancies and thus more active sites for the gas sensing reaction, improving the sensing performance with respect to pristine WO_3. According to them, upon exposure to reducing gases, the release of electrons causes a reduction in resistance, as can be expected of n-type semiconductors.

In another work, Cai et al. [97] realized composite ZnO/$ZnWO_4$ nanofibers via electrospinning that exhibited high sensitivity, outstanding enhanced selectivity, and excellent long-term stability towards triethylammine with respect to pure ZnO. They justify this by arguing that an n-n heterojunction is formed, giving rise to increased depletion of majority carriers when exposed to air, explained trough the usual surface oxygen adsorption model. Upon exposure to a reducing gas, the release of electrons produces a variation in conductivity greater than in pure ZnO thanks to the heterojunction, with electrons flowing from ZnO to $ZnWO_4$, which they report having a bandgap of 3.36 eV.

Nevertheless, it can be argued form the literature discussed above that $ZnWO_4$ shows promise in gas sensing applications due to its tunable electronic properties via different synthetic approaches resulting in different morphologies. The favourable heterojunctions it forms with other interesting materials improve the response of conductometric sensors. Unfortunately, there hasn't been much research about the effect of $ZnWO_4$ in optical gas sensing, so the present work represents a step in a new, unexplored direction.

Chapter 3: Experimental

In this chapter the experimental procedures that have been used and the characterization techniques that have been employed are described. First, the syntheses of ZnO and WO_3 sols are presented in Sections 3.1 and 3.2, followed by the synthesis of Pt NP in Section 3.3; then, the syntheses for the production of composite sols are described in Section 3.4. Section 3.5 deals with the deposition and heat treatment of the films, and Section 3.6 contains the instruments, characterization procedures and data analysis methods used.

3.1: Synthesis of ZnO sol

In a typical sol-gel synthesis of ZnO [73] [98] [99], 0.66 g of zinc acetate dihydrate (ZAD) ($Zn(CH_3COO)_2 \cdot 2H_2O$) were dissolved in 5 ml ethanol (EtOH), brought to 60° and kept under stirring for 30 minutes before adding 0.32 g of diethanolamine (DEA, $HN(CH_2CH_2OH)_2$). After the addition of DEA, the dispersion quickly turned from milky white to transparent, with a nominal concentration [ZnO] = 0.6M. Afterwards, the sol was either used immediately or left to age in the dark.

3.2: Synthesis of WO_3 sol

In a typical sol-gel synthesis of WO_3 [36] [76] [100], 1g of metallic W powder was dissolved in 9 ml H_2O_2 30% w/w and put under stirring at 1000 rpm in an ice bath over a hot plate. Due to the strong exothermic character of the reaction, the temperature was raised very slowly, approximately according to this procedure: for the first hour, the hot plate was kept turned off, then the temperature was raised to 15° over 30 minutes, then to 20° over the next 30 minutes, successively to 25° over another 30 minutes, and finally kept to 30° for about two hours. During this period, the solution slowly turned from transparent to pale yellow as the powder dissolved. The product was then removed from the ice bath, filtered with a 5 μm syringe-filter to remove unreacted powder, and diluted 1:1 by volume EtOH. Finally, the solution was brought to 80° under stirring at 1000 rpm for 45 minutes. unreacted H_2O_2 [36], during this last step the flask was almost but not completely closed with parafilm, so that the

unreacted H_2O_2 could bubble out of the solution. The final product had a nominal concentration [WO_3] = 0.3 M.

3.3: Synthesis of Platinum Nanoparticles

The synthesis of Pt NPs was done according to the polyol method [47], [52]. The glassware was washed with aqua regia and dried in oven at 100° beforehand to ensure the removal of the water film. In a round-bottom flask, 0.067 g of hexachloroplatinic acid (H_2PtCl_6) and 18.7 mg of sodium chloride (NaCl) were dissolved in 3 ml of Ethylene Glycol (EG, $HOCH_2CH_2OH$), degassed and put under inert atmosphere, forming a pale-orange solution (Solution 1). In a three-necked round-bottom flask, 150 mg of $NaNO_3$ and 55 mg of polyvinylpyrrolidone (PVP-10K) were dissolved in 13 ml of EG, degassed, and brought at 160° under inert atmosphere, giving Solution 2. After 20 minutes, Solution 1 was quickly injected into Solution 2. After 5-10 minutes, the color changed from pale orange to dark brown, proving the formation of NPs. This colloidal solution was kept at 160° under inert atmosphere for 30 minutes, then cooled to room temperature and precipitated with an excess of acetone (about 10:1 in volume). Then the solution was centrifuged twice at 4000 rpm for 5 minutes to promote precipitation. Finally, a dark brown precipitate was obtained, which was removed from the acetone and redispersed in EtOH. Hypothesizing a 70% yield, the NPs were dispersed in 3.81 mL EtOH, giving a final nominal concentration [Pt]=30mM.

3.4: Synthesis of composite sols

In order to produce ZnO/WO_3 composite films, two different synthetic approaches were followed, as detailed in the next paragraphs: a solution mixing approach (M-synthesis), and a salt dissolution approach (S-synthesis).

3.4.1. M synthesis

In the first synthesis, which we will call “Mixing synthesis” or, more briefly, “M-synthesis” the two solutions of ZnO and WO_3, prepared according to the previous protocols, were gently

mixed together in an Eppendorf vial in different volume ratio, in order to tune the final molar ratio between Zn and W. This approach, schematized in Figure 3.1, was adapted from the literature [76]. Leonard and coworkers [101] similarly prepared a composite film by mixing the precursor sols together and then depositing and annealing the composite sol.

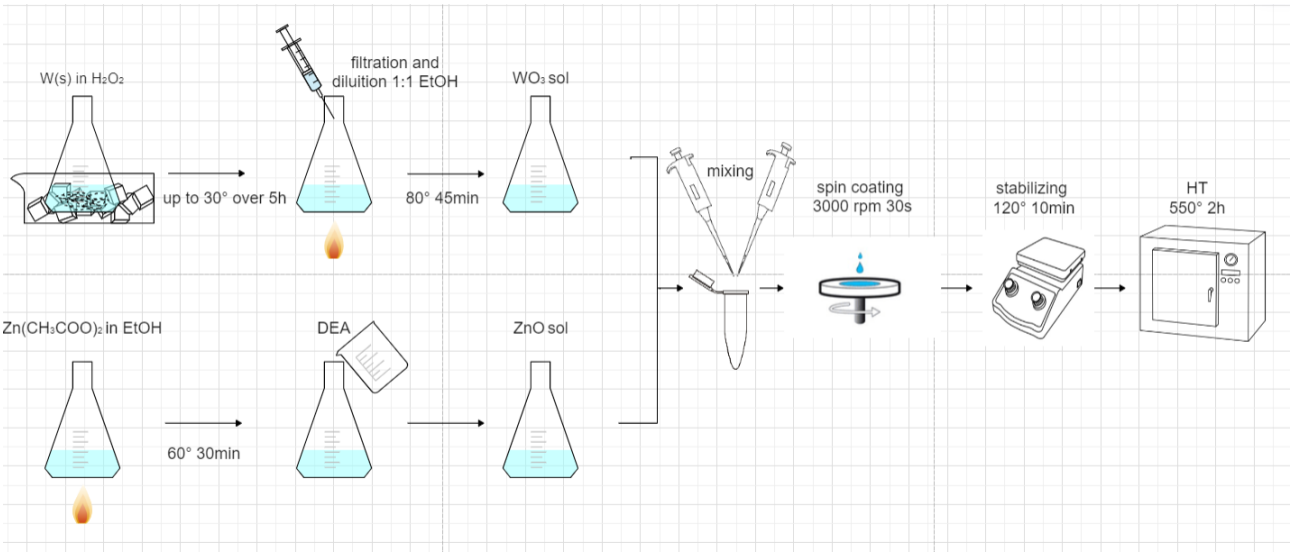

Figure 3.1: Fabrication process of thin films via the M synthesis and subsequent deposition and heat treatment.

3.4.2. S synthesis

In the second synthesis, which we will call “Salt dissolution synthesis” or “S-synthesis” henceforth, ZAD salt was directly dissolved into the WO_3 solution according to specific mole ratios. If the WO_3 solution was still hot enough and the target Zn concentration low enough, no additional stirring was required to complete dissolve the precursor, thanks to the high acidity of the WO_3 sol. Otherwise, a few minutes of moderate stirring was sufficient to completely dissolve ZAD. Figure 3.2 schematizes this procedure. To the best of our knowledge, no one has attempted this synthetic route before, but a similar approach can be found in [101] and [102], in which ZAD is dissolved in a WO_3 sol obtained from phosphotungstic acid hydrate or ammonium paratungstate, respectively. These works lead us to believe that our syntheses might have produced $ZnWO_4/WO_3$ films, as will be discussed in the results section.

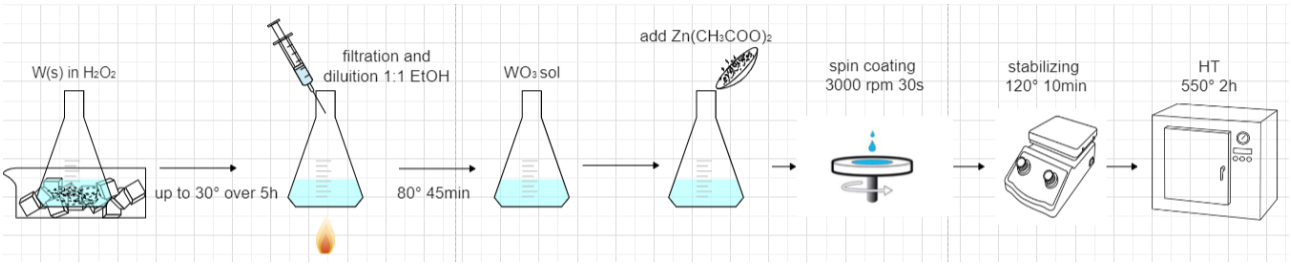

Figure 3.2: Fabrication process of thin films via the S synthesis and subsequent deposition and heat treatment.

3.5 Preparation of thin films

3.5.1 Substrate preparation

Substrate preparation and cleanliness is of cardinal importance in order to obtain a film of good quality: over the course of this work, we optimized the cleaning procedure, which was essential in order to obtain reproducible results. The substrates were first cut with a diamond-tipped pen from silicon wafers and quartz slides (1.5x1.5 cm) with the help of a ruler and some cloth to protect the material from scratches. For the gas-sensing measurements, the corners of the substrates were snapped using hooked metal tweezers to fit the samples in the measurement cell.

The cleaning procedure is as follows: first, substrates were rinsed in EtOH, then ultrasonicated in EtOH for 3 minutes. Finally, they were plasma cleaned for 5 minutes using a Harrick PDC-002-CE plasma cleaner controlled by a Plasmaflo PDC-FMG-2 flow control unit. During the cleaning and deposition processes, plastic tweezers were preferred to handle the substrates and prevent the formation of additional cracks. Teflon-tipped or metal tweezers were instead used to handle the substrates when hot to prevent contamination from molten plastic.

3.5.2 Sol deposition

The sols obtained with the methods discussed above were deposited by spin-coating either on silicon or quartz substrates, according to the following procedure: 30 µl of sol or mixture were dropped on the substrate via micropipette and were then spun at 3000 rpm for 30s

without acceleration using a Laurell WS-650MZ-23NPPB spin coater. Then, the as-deposited films were stabilized over a hot plate at 120° for 10 minutes to improve film adhesion and evaporation of residual solvent.

For the Pt-functionalized films, Pt nanoparticles were then deposited upon films previously crystallized through thermal treatment (see 3.5.3). The deposition parameters were as follows: 20 µl of Pt NP were dropped on the film, followed by spin coating at 2000 rpm for 30s, and stabilizing at 250° for 30 minutes on a hot plate. Two layers were deposited as a compromise between having good surface coverage and preventing a loss of transmittance due to an excessively thick Pt layer.

3.5.3 Heat Treatment

For the heat treatment, the films were placed in an oven at room temperature and heated it up to 550° at 10°C/min, holding the temperature for 2 hours, then let to cool to room temperature inside the oven overnight. We have chosen this temperature as literature proves that at least a temperature of 500°C is needed to guarantee the formation of crystalline monoclinic WO_3 [35] [36].During the course of our trial runs we noticed that our oven did not guarantee a homogeneous temperature across the length of the chamber, and preliminary X-ray diffraction patterns showed that the samples crystallized better the more they were placed towards the end of the oven. The effect was further compounded by using a refractory heat disperser to hold our samples, as this proved too good of a thermal contact and thus led to samples that didn’t crystallize enough as they were dispersing too much heat. So, to optimize the heat treatment, we started arranging our samples face-up in boat-shaped ceramic vessels, which we took care to always place at the very end of the oven: this allowed us to obtain films with a better degree of crystallinity.

3.6 Characterizations

3.6.1 X-Ray Diffraction

XRD is a non-destructive technique used to obtain information about composition, microstructure and morphology of materials generally in the solid state or in powder form.

An X-ray beam interacts with the sample and undergoes coherent diffraction with the crystal lattice, as described in Bragg's Law:

$$n\lambda = 2dsin\theta \quad (3.1)$$

Where n is the diffraction order, λ is the incident wavelength, d is the interplanar spacing for the crystal plane family causing the diffraction, and θ is the incidence angle, or Bragg's angle. The diffracted beam is collected by a detector. By plotting the intensity of the beam reaching the detector as a function of the Bragg's angle, the diffraction pattern is obtained for each material.

The characteristic pattern of the crystalline material is then compared with the reference spectra of known substances.

The crystalline phases of the thin films were characterized by X-Ray diffraction (XRD) by using a Philips Panalytical XPert Pro, diffractometer equipped with grazing incidence X-Ray optics (GIXRD). The analyses were performed at an angle of 0.5° incidence, using Cu K_α Ni-filtered radiation at 40 kV and 40 mA.

The thus-collected diffraction patterns were then analyzed via Match! software via the following procedure: first, the data were smoothed via the "Smooth" function once to remove instrumental artifacts, and the baseline due to amorphous phases was eliminated to leave a diffraction pattern made out only of peaks. Then, the function "Find Peaks" was run, setting the peaks to be optimized for position, FWHM, and area. The peaks thus detected were confronted with the software's database, inputting Zn, W and O as the sole possible constituents of the phases.

To assess the crystallite size, Scherrer's Equation was used:

$$D = \frac{k\lambda}{\beta cos\theta} \quad (3.2)$$

where D is the average crystallite size for a certain phase, k is a shape factor that we considered equal to 0.9, λ is the incident wavelength, β is the FWHM for the considered peak corrected for instrumental broadening, which in our case was equal to β_{instr}=0.28°, and θ is the Bragg angle for the considered peak.

3.6.2 Scanning Electron Microscopy

SEM is a precision instrument for high resolution micro-area topographical, morphological and compositional analysis. The characterization is performed using a high-energy electron beam. The electron beam is generally generated via thermionic emission or field emission and focused through electromagnetic lenses onto the sample, producing a composite signal made out of secondary electrons, backscattered electrons, auger electrons, and secondary X-rays.

Therefore, the signal generated is collected by various detectors and reprocessed to obtain a high-resolution image. This occurs under vacuum conditions, which prevents molecules present in the microscope column from interacting with the electron beam. SEM can provide micro-images at nanometer resolution with large scan areas.

Scanning Electron Microscope was used to evaluate the surface morphology of the nanocomposites using a FE-SEM, Zeiss Sigma HD microscope operating at 3 kV and collecting signal with InLens detector.

Assessing the grain size distribution via SEM images was done through ImageJ software, following the procedure exposed in [104]. First, the scale of the as-obtained image was obtained from the original scale bar, which then was cropped togherther with the other measurement parameters. Then the scale was set in the software via the “Set Scale” function. Then, a combination of the “Smooth” and “Sharpen” functions was run a few times, to improve the definition of the grain boundaries. Then, the contrast of the image was maximized, and the “Despeckle” function was run to remove excess pixels. Finally, the length of 100 particles for each sample was collected, measured along the grain’s longest dimension, taking care to reproduce the distribution of lengths by considering a few large grains and all the surrounding smaller grains, as to randomize the position of the analyzed particles while still making sure to represent all the lengths.

3.6.3 Ellipsometry

An ellipsometer is an instrument used to measure the thickness of thin films and their optical properties, such as the refractive index, and their dielectric function. The operation of an ellipsometer is based on the reflection of polarized light on a material to obtain information about its thickness and optical properties. Light incident on the sample is linearly polarized using a polarizer and then reflected off the surface of the material. Hence, the light changes its polarization state due to interaction with the material. The ellipsometer measures the ratio of the radiation intensity reflected in the plane of incidence (Rp, p-polarized) to that perpendicular to it (Rs, s-polarized), identifying ψ and Δ for each angle-wavelength combination. The first parameter ψ identifies the angle between the two polarization components of the reflected ray, while Δ identifies the phase between these two components. Then, the data obtained from the ellipsometer are fitted with the appropriate model for the dielectric function (such as Cauchy, Drude or Lorentz) through integrated software.

In the thesis project Ψ and Δ have been measured using a J.A. Woollam V-VASE Spectroscopic Ellipsometer in vertical configuration, at angles of incidence of 65°- 75° for both silicon and quartz substrates in the wavelength range 300-1000 nm.

The film thickness has been evaluated from Ψ, Δ data using the WVASE32 ellipsometry data analysis software, fitting the experimental data with the Cauchy model.

3.6.4 Raman Spectroscopy

Raman spectroscopy provides information regarding the vibrational energy levels of molecules. Although is has a resemblance with IR spectroscopy, the principle of Raman spectroscopy is based on inelastic light scattering. Most of the scattered radiation has the same frequency as the incident radiation and this is called Rayleigh scattering. A small part of the scattered radiation, about 1 every 10^7 photons, has frequencies at lower (Stokes lines) and higher (anti-Stokes lines) frequencies. For this reason, high-intensity sources such as lasers are typically used. For a particular vibrational mode of a molecule to be Raman-active, the selection rule is that the molecular polarizability must change during the transition between fundamental and excited state.

In this work, Raman spectra were acquired using a XploRA PLUS MicroRaman Spectrometer, using a 532 nm laser source. Each measurement is composed of 3 iterations each with an accumulation time of 30 s, with a frequency range of 20-1000 cm^{-1}.

3.6.5 Gas Sensing Measurements

A spectrophotometer is an optical device used for determining the transmittance, and thus the absorbance, of a sample in the form of solution or thin film at a given wavelength. A light beam exits from a monochromator and passes through the sample reaching a detector positioned behind it. The variation in light beam intensity (transmittance) is given as:

$$T = \frac{I}{I_0} \tag{3.3}$$

where I is the output beam intensity and I_o is the input beam intensity.

Absorbance is the quantity used for the results and is related to transmittance by the following relationship:

$$A = \log(\frac{I_0}{I}) \tag{3.4}$$

In the thesis project a Jasco V-650 spectrophotometer with a wavelength range between 190 nm to 900 nm coupled with a Harrick gas flow cell controlled by a Gas Blender 3000 mixer by MCQ Instruments was used to perform the optical gas sensing test.

Our quartz-deposited thin films were thus exposed to light in the UV-VIS-NIR range. Since the detector is placed behind the sensitive material, this constitutes a transmission-based optical gas sensor. The measurand of this device is the change in absorbance of the thin film upon exposure to hydrogen gas. These data were collected by the spectrophotometer's detector and visualized by the integrated software Spectra Manager. Figure 3.3 schematizes the combined spectrophotometer-gas cell apparatus.

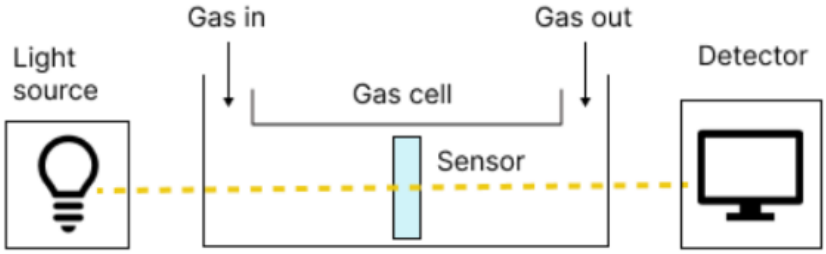

Figure 3.3: scheme of a transmittance optical gas sensor.

For static gas sensing tests, first we acquired the baseline of the sample at room temperature in the range 200-900 nm, with a resolution of 2 nm, without fluxing gas. Then we brought the sample to the desired temperature of 100°C, waited a few minutes for the sample's temperature to homogenize and then acquired a reference spectrum of the sample at the set temperature. Then the reference gas (dried air) was fluxed at 400 ml/min for 10 minutes to completely saturate the atmosphere inside the cell before acquiring the spectra of the samples. Then, the gas was switched from air to H_2 (5% balanced in Ar), following the same procedure (400 ml/min). After 15 minutes, the spectrum of the samples in the colored state was collected. Finally, the gas was switched back to compressed air to purge the system (400 ml/min), and after the usual 15 minutes we acquired a spectrum of the now-bleached state of the sample.

The Optical Absorption Change was calculated as follows from the spectra representing the absorbance under air before coloring and H_2,

$$OAC = Abs_{H_2} - Abs_{Air_{before}} \quad (3.5)$$

and plotted against λ to assess for which wavelength the sample showed the highest variation. From these studies, we selected a wavelength (λ=870 nm) in the range where OAC was maximized to perform the dynamic measurements.

The spectra acquired with air after H_2 were confronted with the spectra acquired before H_2 by subtraction to assess the recovery capabilities of the sample.

For the dynamic gas sensing tests, we set our spectrophotometer at the selected wavelength (870 nm), using the same flux of 400 ml/min. In our first round of experiments,

we used a 7-step program using Ar as reference gas, cycling Ar/ H_2 5% in Ar/ Ar/H_2 5% in Ar / Ar/H_2 5% in Ar/ Ar, always fluxing 10 minutes for the first step, then either 10 minutes for all the next cycles if the sample seemed to recover fast enough, or 20 minutes if the recovery was too slow.

In a second set of experiments, we adopted another 7-step program using compressed air as reference gas, consisting of 10-minute cycles as follows: air/ H_2 5% in Ar/ air/ H_2 5% in Ar/ air/ H_2 5% in Ar/ air, with the usual flux of 400 ml/min at 870 nm.

From these dynamic tests, we measured the response of the sample as $\Delta Abs_{\lambda=870nm}$, that is the difference between the average absorbance during the coloring cycle and the average absorbance during the bleaching cycle.

The response and recovery time of the sample were calculated as $t_{response}90\%$ and $t_{recovery}90\%$, respectively. The response time represents the time required for the Absorbance to rise to 90% of its maximum value during a coloring cycle, while the recovery time is defined as the time needed for the Absorbance to decrease by 90% during a bleaching cycle.

Chapter 4: Results and Discussion

In this chapter, the results of our investigations are presented. In Section 4.1, we focused on the optimal ageing time of precursor's sols. In Section 4.2, we experimented with different syntheses in order to obtain the most convenient synthesis. In Section 4.3, we report our work with lower zinc concentrations and its effect on structure and performance.

4.1 Effect of ageing

In the first round of experiments, we wished to assess the influence of the sol ageing time on the gas sensing performance. A set of samples was deposited by spin-coating on silicon and they were used to characterize thickness (ellipsometry) and morphology (SEM).

Name	Composition (Zn:W)	Ageing	Heat Treatment	Thickness (nm)
C1	ZnO	fresh	550°C 2h	82
C3	WO3	8 days	550°C 2h	32
C5	Zn:W1:9	fresh(Z fresh W 8 days)	550°C 2h	38
C7	ZnO	24h	550°C 2h	106
C9	WO3	9 days	550°C 2h	41
C11	Zn:W1:9	24h(Z fresh W 8 days)	550°C 2h	46
C13	Zn:W1:9	fresh (Z 24h W 9 days)	550°C 2h	47
C15	ZnO	48h	550°C 2h	124
C17	WO3	10 days	550°C 2h	41
C19	Zn:W1:9	48h(Z fresh W 8 days)	550°C 2h	45
C20	Zn:W1:9	48h(Z fresh W 8 days)	550°C 2h	46
C21	Zn:W1:9	24h(Z 24h W 9 days)	550°C 2h	45

Table 4.1: samples deposited on silicon to study the effect of ageing of the sol-gel solutions

ZnO and WO3 sols were synthesize following the protocol reported in Chapter 3 (M-synthesis). The sols were left to age for different time before to be mixed together before the deposition. Eventually, the mixed solution was left to age up to 48 h. The samples thus produced are described in Table 4.1. Note that for composite samples, under the ageing column is reported first the ageing time of the admixture, then the ageing time of the single components at the time of mixture. For instance, samples C5 and C11 were prepared form the same mixture, the former being deposited fresh, the latter the next day. By contrast, C13 was prepared the same day as C11, but C13 was made with a mixture prepared that day, while C11 with the mixture of the day before.

4.1.1 Effect of ageing on macroscopic structure

Our first preliminary investigation to evaluate the quality of the films on a macroscopic scale was trough optical microscopy. Even though such a technique clearly cannot provide information on the microscopic structure, it is still useful in assessing the presence of macroscopic defects such as inhomogeneities, cracks or dewetting. Figure 4.1 shows a series of samples with the same zinc/tungsten molar ratio of 1:9, or Zn0.1W0.9, differing by ageing of the mixture.

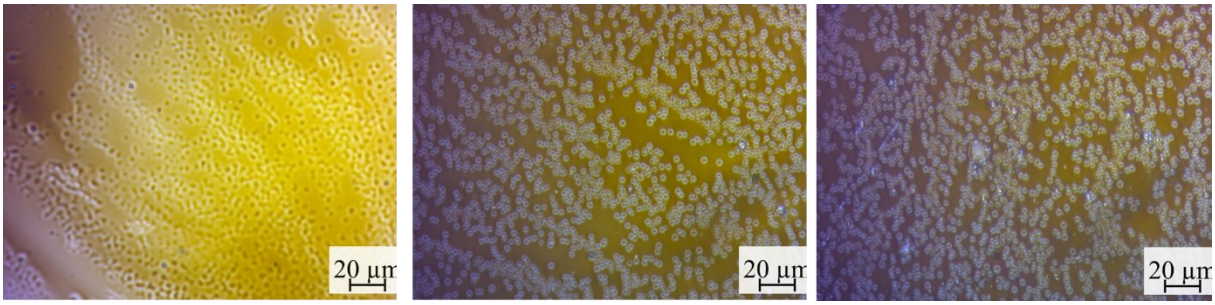

Figure 4.1: optical microscopy of samples (left to right) C5, C11, and C19, in which the sols were mixed together and respectively deposited fresh, aged 24h, or aged 48h.

As can be clearly seen, with the increase of ageing, more bubbles appear on the surface, indicating an irregular structure full of macroscopic defects. According to Norhidayah and coworkers [105], the crystallite size of the ZnO films increases with increasing sol ageing time. This concurs with an increment in the roughness of the film with the ageing time, due to the fact that the crystal growth rate is relatively fast at the liquid–solid interface at higher aging time. Being the sol–gel process based on colloidal particles, they argue that by

increasing the solution ageing time the reaction will be faster, leading to a rougher film. They argue that optimal sol ageing time for a ZnO sol is 24h, which exhibits comparatively smoother surface.

Nazarzadeh et al. [106] proved that ageing changes the distribution of particle size. They base their reasoning on the fact that the smaller the particle size, the greater the tendency to join during ageing. Their analysis showed that after ageing the polydispersity index (PDI) and average particle size (average Z) are higher for sols stirred at 50°C than for those stirred at 60°C, and particularly that the distribution of particles in sols before and after ageing is monodisperse and polydisperse, respectively

Shuangjiao et al. [107] produced an optical fiber WO_3/Pt hydrogen gas sensor and experimented with ageing. They found that the response time of the WO_3/Pt film gradually increases, and the sensitivity first increases and then decreases with ageing, with a maximum when aging for 7 days. When the aging time is shorter, the sol has low viscosity and the prepared sensing film is thin and although the response time is fast, the sensitivity is relatively low. When the aging time is too long instead, the sol will be too sticky which leads to cracking of the film, resulting in low film sensitivity and poor repeatability. Therefore, for them the best aging time was about 7 days. To evaluate this result, we have to take into account the different modalities of gas sensing: in an optical fiber gas sensor, the measurand is a change in refractive index upon H_2 injection, which requires an amorphous film which is not too thin, which in turn requires a sol that has neither too high nor too low viscosity. Our goal to optimize transmittance optical sensing instead requires thin, highly crystalline films, explaining how too long ageing times are undesirable for our goal. In fact, a noticeable increase in viscosity upon formation of the mixture was observed for our films, leading to the formation of bubbles while transferring the mixture from the Eppendorf vial to the film. A similar increase in viscosity upon ageing must have happened also to our pure ZnO and WO_3 samples.

As the following graphs in Figure 4.2 demonstrate, either increasing the ageing time of the mixture or the ageing time of the component sols increases the thickness of the resulting films. The effect is much more pronounced for ZnO than for WO_3 or the 1:9 mixture, and mixture ageing seems to contribute more to thickness than the ageing of the individual sols.

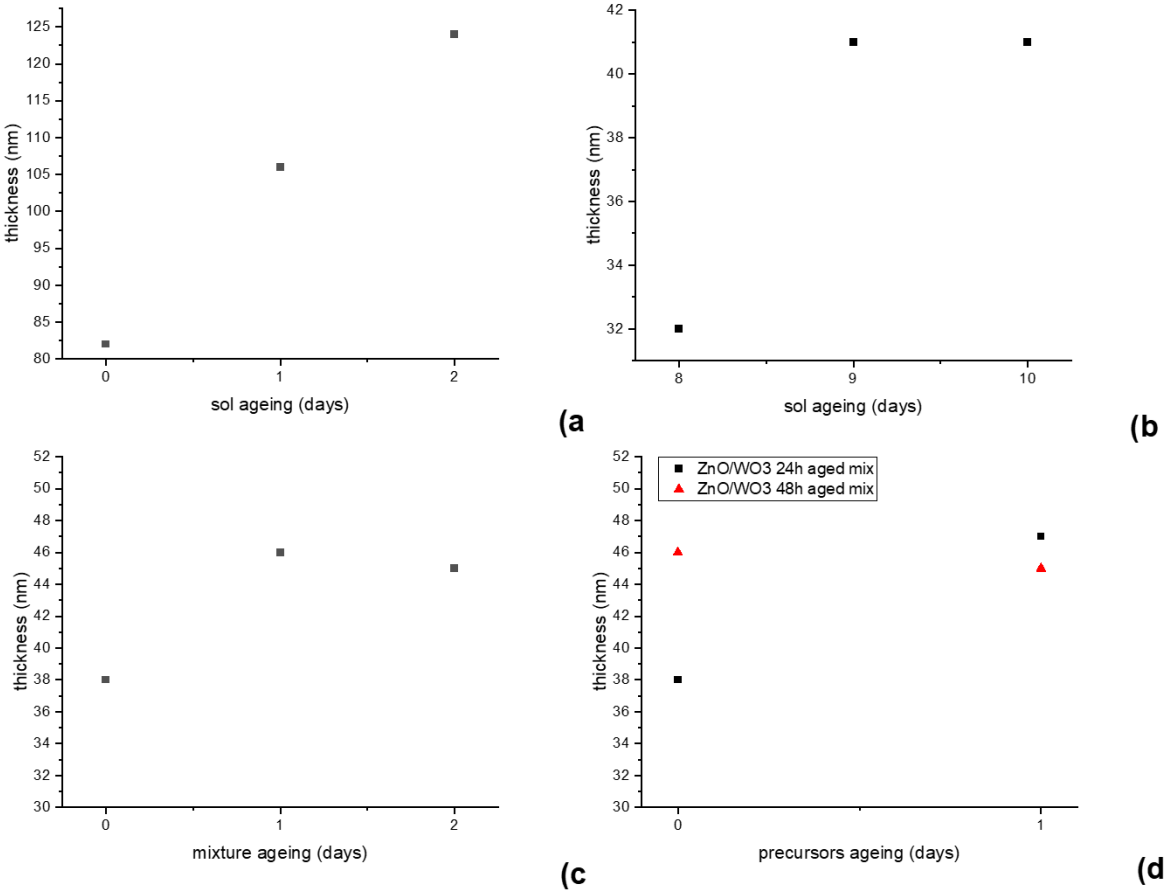

Figure 4.2: thickness of thin films as a function of ageing time; a) ZnO , b) WO_3, c) a Zn/W 1:9 mixture prepared from fresh sols and then left to age, d) Zn/W 1:9 mixtures prepared from ZnO (fresh or aged 24h) and WO3 sols (aged 8 or 9 days) and then left to age 24 or 48 hours.

From these analyses, we deduced that ageing has a detrimental effect on macroscopic film quality and produces an undesirable increase in thickness due to increased viscosity. Next, we turned our attention to the influence of ageing on morphology.

4.1.2 Effect of ageing on morphology

Figure 4.3 shows the different morphology of samples prepared from fresh and aged mixtures starting from fresh sols, with two different Zn/W molar ratio, 1:9 and 2:8. It can be seen that with ageing, there is a change in the distribution of the grain size, with the largest grains becoming larger in proportion to the smaller ones, which increase in number. In essence, the grain size distribution becomes more uneven, probably since during ageing the larger agglomerates had more time to grow at the expense of the smaller ones, in a

typical example of Ostwald ripening. As the image shows, this concurs with a decrease in porosity, which could worsen the permeability of the film to hydrogen gas, leading to a loss of response as will be discussed later.

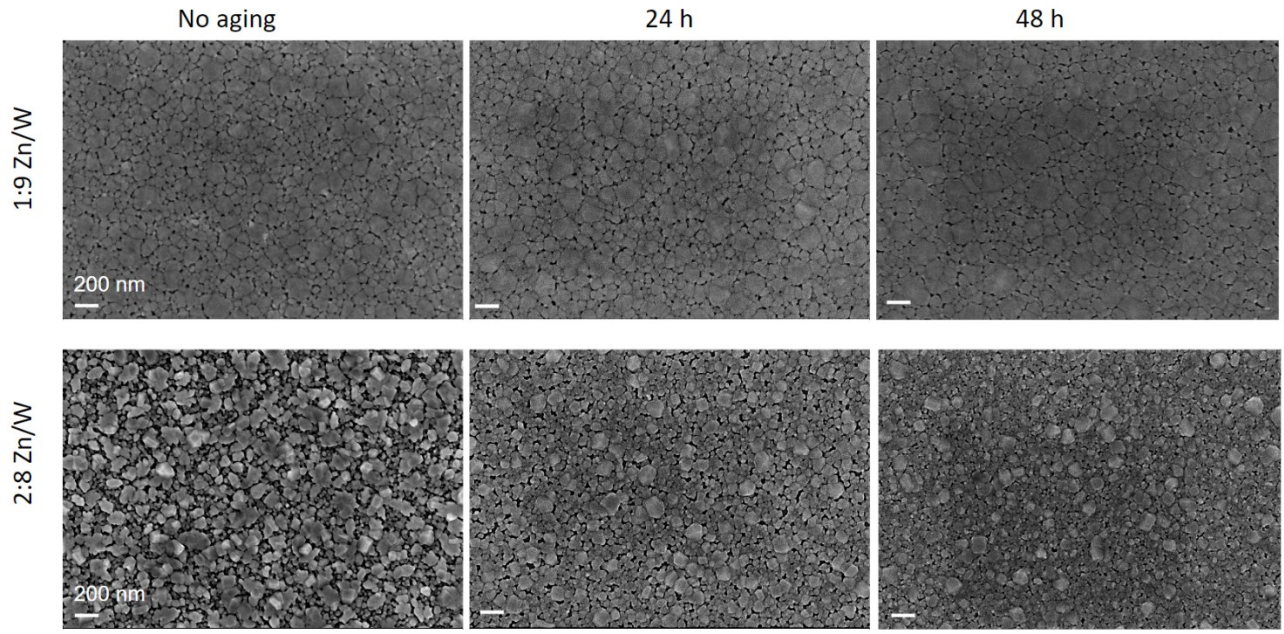

Figure 4.3: SEM images showing the morphological influence of ageing on Zn/W solution.

4.1.2 Effect of ageing on gas sensing

After the preliminary study on silicon, thin films were deposited on fused silica glass to assess the effect of ageing on the gas sensing behavior. Samples were prepared according to the composition reported in Table 4.2, starting with fresh ZnO and WO_3 solutions, and tuning the time of aging of the mixture solution. Gas sensing tests were performed on the samples using argon as reference and carrier gas, at a fixed wavelength of 870 nm and an operative temperature of 100°C.

From earlier studies, it was demonstrated that pure WO_3 films did not recover fully while using Argon gas as a recovery gas in static conditions at 100°C. For this reason, we decided to focus on composite films. Figure 4.4 shows the different static behavior of a WO_3 and a 1:9 composite film.

Name	Composition (Zn:W)	Ageing	Thickness (nm)
Q8	Zn/W 1:9	Fresh	55
Q9	Zn/W 2:8	Fresh	43
Q17	Zn/W 1:9	24h	46
Q19	Zn/W 2:8	24h	53
Q25	Zn/W 1:9	48h	51
Q27	Zn/W 2:8	48h	56

Table 4.2: fresh and aged samples investigated via dynamic gas sensing

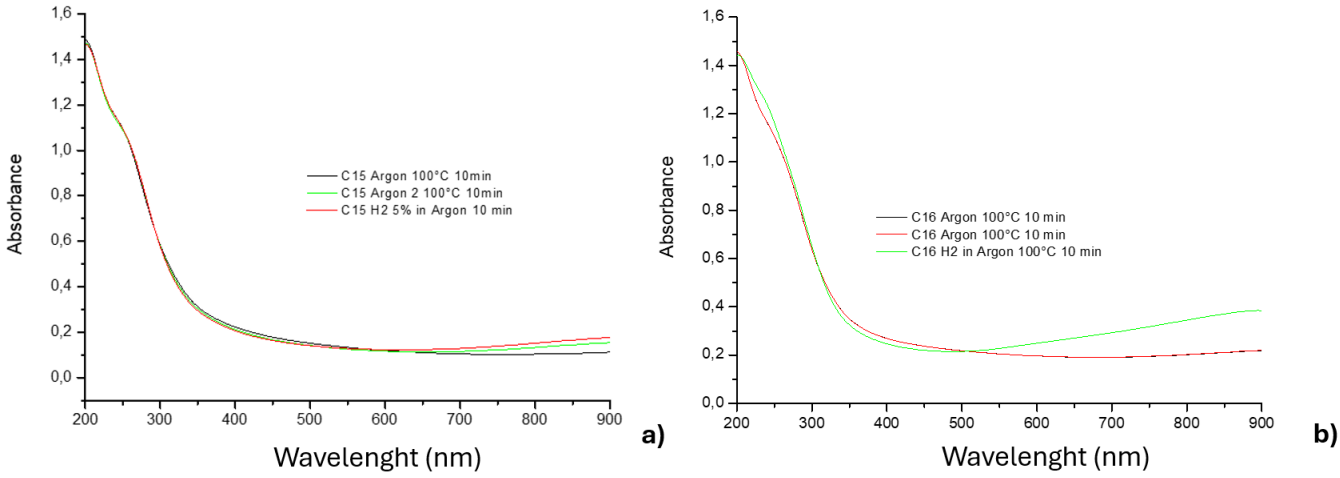

Figure 4.4: static gas sensing for a) WO_3 and b) 1:9 composite using Argon as a recovery gas.

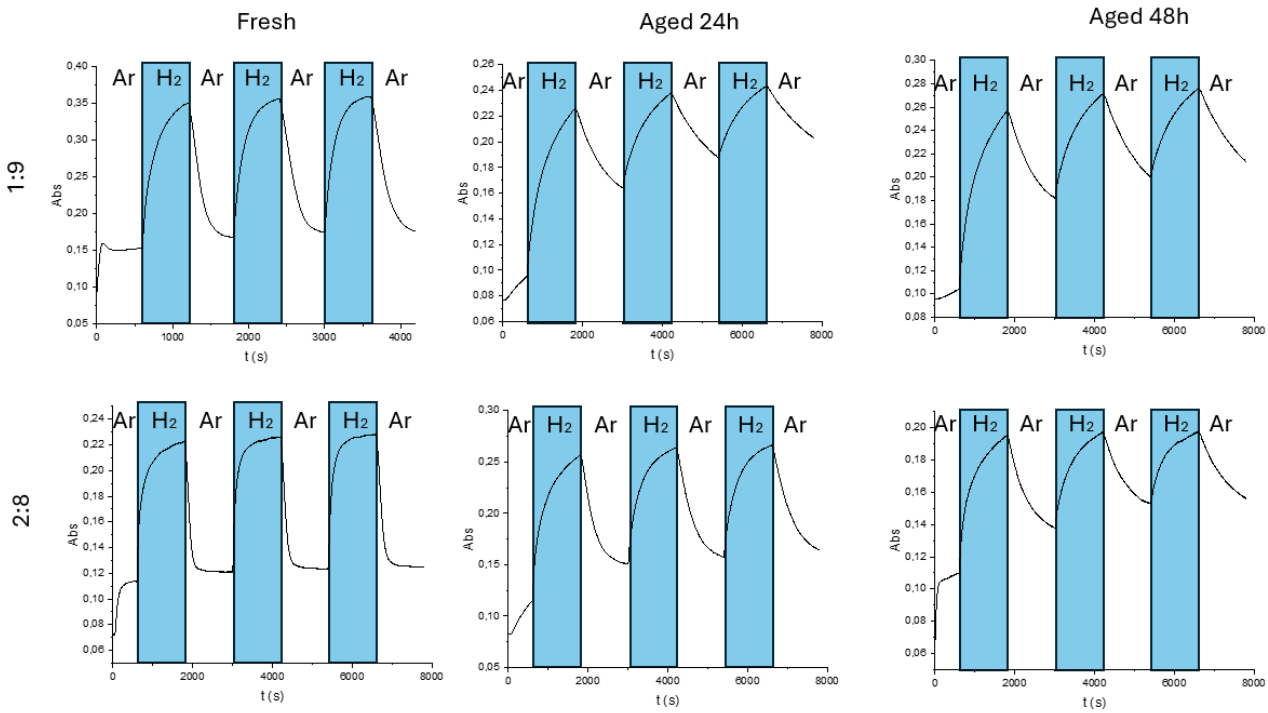

Figure 4.5: dynamic hydrogen sensing tests for samples with different composition and ageing performed at 100°C.

As can be seen from the data in Figure 4.5, Zn/W 1:9 with no ageing shows the highest $\Delta Abs_{\lambda=870nm}$ and the fastest response, while 2:8 had the best recovery. The small initial increase of absorbance seen in the first Ar cycle is ascribable to the change of atmosphere in the gas chamber: as oxygen is substituted by Ar, the atmosphere becomes less oxidizing and the partial pressure of oxygen decreases, which could promote the desorption of oxygen from the film's surface, leading to changes in W oxidation state and thus might provoke a slight gasochromic response even in the absence of hydrogen. This could also explain the baseline drift which becomes noticeable in the aged samples, as the initial oxidized state of the surface is never fully recovered. Table 4.3 presents the gas sensing parameters obtained from these measurements. We decided to report the response and recovery times for the first cycle as these are subject to change upon subsequent cycles. In particular, response times decrease, while recovery times increase with the number of cycles, as will be discussed later. Only the fresh samples recovered within 95% of the baseline, while the aged samples showed a very poor recovery. For this reason, we reported the recovery times only for the fresh samples.

Name	Composition	Ageing	$\Delta Abs_{\lambda=870nm}$	$t_{response}90\%$	$t_{recovery}90\%$ (s)
Q8	Zn/W 1:9	Fresh	0.19	390	300
Q9	Zn/W 2:8	Fresh	0.11	540	205
Q17	Zn/W 1:9	24h	0.15	900	N/A
Q19	Zn/W 2:8	24h	0.14	780	N/A
Q25	Zn/W 1:9	48h	0.13	900	N/A
Q27	Zn/W 2:8	48h	0.09	420	N/A

Table 4.3: OAC, response and recovery of fresh and aged samples.

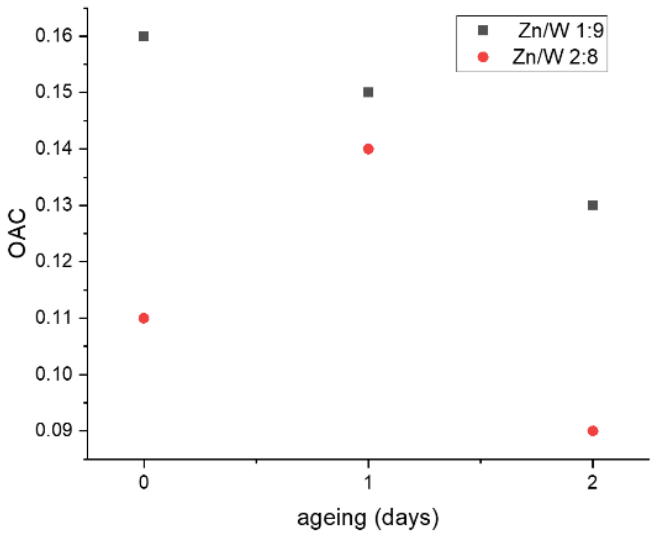

Figure 4.6: The effect of ageing on the $\Delta Abs_{\lambda=870nm}$ of composite films with different compositions.

Figure 4.6 explicits the worsening effect ageing has on $\Delta Abs_{\lambda=870nm}$. For the Zn/W ratio of 1:9, the decrease of $\Delta Abs_{\lambda=870nm}$ with ageing is evident. For the 2:8 samples, Q19, aged 24 hours, showed the best $\Delta Abs_{\lambda=870nm}$, but at the same time also had the worst response time. Since roughness increases both with zinc content [76] and ageing [105], it seems likely that 2:8 presented a rougher surface than 1:9; there may be some compensation between surface roughness and porosity that causes $\Delta Abs_{\lambda=870nm}$ to improve for 2:8 after 24 hours of

ageing. This increased roughness might also explain why, after ageing, 2:8 showed better response times than 1:9, while before ageing 1:9 had the faster response. Nevertheless, the fact that fresh 1:9 had this combined with the best $\Delta Abs_{\lambda=870nm}$ and almost complete recovery lead us to investigate towards lower zinc concentrations.

There are some remarks to be done common to all these preliminary gas sensing experiments. First, the response time on the first circle is always greater than on subsequent ones. Second, no sample showed a complete recovery of the baseline, with the fresh ones coming the closest. This is due to the use of Argon as a recovery gas: an oxidant atmosphere promotes the bleaching reaction to restore HWO_3 into WO_3 [108], so under inert atmosphere the only available recovery mechanism is thermal H_2 desorption, limiting the amount of H that can be removed from the lattice and thus the recovery of the bleached state, since the decomposition and disproportionation reactions require respectively 176°C and 336°C [31]. Thus, the faster response times on subsequent cycles may be linked to the use of Argon, as the initial state is never fully recovered, thus the subsequent colouring cycles take less time to reach the same absorbance. On the contrary, the recovery times become greater on subsequent cycles, which is a behaviour which presented itself even while using air as a recovery gas in other experiments (see Sections 4.2 and 4.3), albeit less dramatically. In summary, these studies provided us with two important information: sol ageing worsens gas sensing, and Argon is not an adequate recovery gas.

4.2 Effect of synthetic approach

4.2.1 Effect of synthesis on crystal structure

In the next round of experiments, we compared the two syntheses, M and S, and their effect on crystal structure, film morphology, and gas sensing properties. Figures 4.7 and 4.8 show, respectively, the GIXRD diffraction patterns for samples prepared through M-synthesis and trough S-synthesis with different molar ratios between Zn and W. Table 4.4 reports the characteristics of the films deposited on quartz and prepared for the X-ray analysis.

Name	Synthesis	Composition (molar ratios)	Composition ($moles_{Zn}/moles_{(W+Zn)}$)	Thickness (nm)	Refractive index at 500 nm
MQ1	M	Zn:W 1:12	0.077	28	2.2
MQ2	M	Zn:W 1:9	0.1	37	2.1
MQ3	M	Zn:W 2:8	0.2	51	2.0
SQ4	S	Zn:W 1:12	0.077	35	2.2
SQ5	S	Zn:W 1:9	0.1	37	2.1
SQ6	S	Zn:W 2:8	0.2	35	2.0

Table 4.4: samples analyzed via GIXRD.

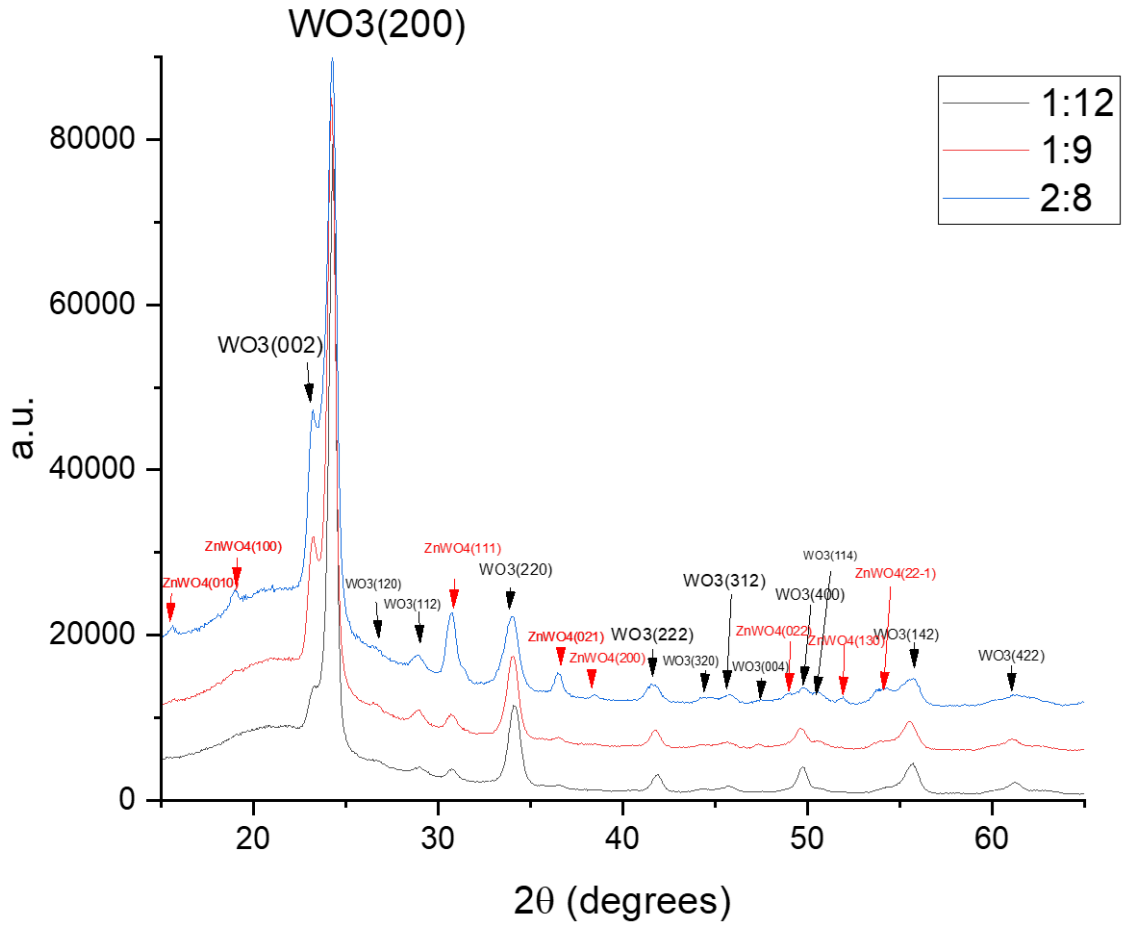

Figure 4.7: GIXRD pattern of films prepared trough M synthesis.

The patterns mainly show peaks attributed to monoclinic WO_3 (JCPDS number 83-0950 [109]), showing a strong (200) preferred orientation for all films. A substantial baseline shows the presence of amorphous phases, due both to the quartz substrate and to the film. The presence of amorphous phases in the film was verified both on silicon and on quartz-deposited films, as even after subtracting the substrate contribution measured from a blank substrate there was still a baseline. As the amount of zinc increases, new peaks emerge, which we attributed to monoclinic $ZnWO_4$ (JCPDS number 73-0554 [110]), and with a preferential (111) orientation. The WO_3 (200) orientation seems to be peculiar to our films, as several studies in literature report the full (002) – (020) – (200) triad for WO_3 [35],[111]. There are some visible differences between the two syntheses: the S synthesis pattern shows a stronger (200) preference than the M synthesis, with the (002) peak being generally less intense, broader and less resolved in the S synthesis. It is also noticeable that, in the S-synthesis, the crystallization of WO3 slightly decreases as Zn doping concentration increases, as can be seen by the deterioration of the diffraction intensity of (200) orientation plane [112]. The M synthesis produced more peaks assignable to $ZnWO_4$, in contrast with

the S synthesis, in which a $ZnWO_4$ phase with a lesser degree of crystallization is formed. Paipitak and coworkers [112] argue that, since the ionic radius of Zn^{2+}(0.74 Å) is slightly larger than that of W^{6+},(0.65 Å) it can be inferred that zinc may be incorporated into the WO_3 lattice by displacing some W^{6+} ions without changing its monoclinic structure. In addition, the formation of the monoclinic $ZnWO_4$ phase is ascribable to the difficulty of substitution of Zn into WO_3 lattice resulting from the difference between their ionic radii. Furthermore, it is noticeable that in the S synthesis, the 1:9 sample produced $ZnWO_4$ peaks with higher intensity with respect to 2:8. This might be due to the higher viscosity of the 2:8 sol that could have prevented a more uniform distribution of Zn across the film and thus worse crystallization.

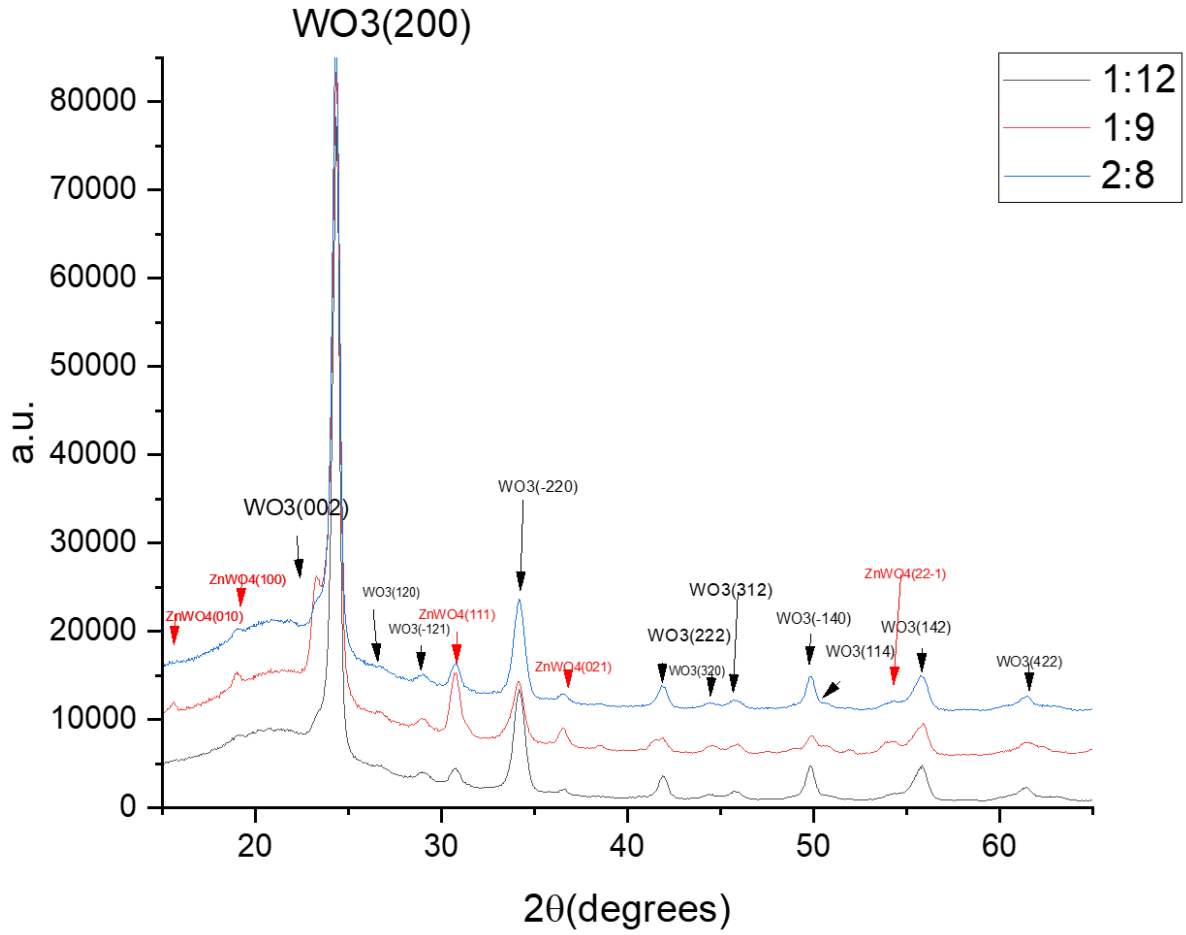

Figure 4.8: GIXRD pattern of films prepared trough S synthesis.

The average crystallite size was investigated through Scherrer's equation. For this purpose, the FWHM of the main peaks of each phase was used, so (200) for WO_3 and (111) for $ZnWO_4$. Figure 4.9 shows the dependence of crystallite size on composition, expressed as zinc molar fraction.

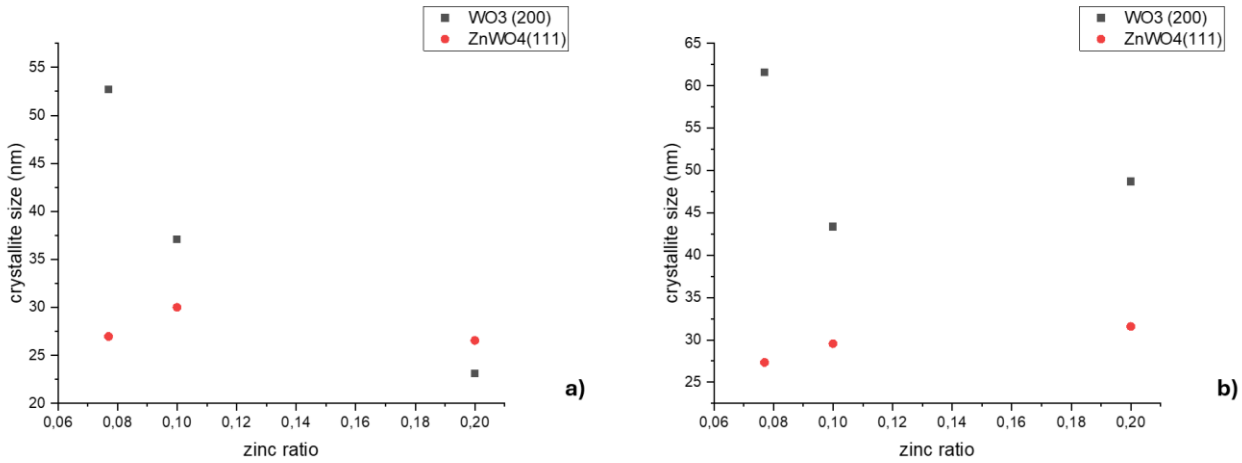

Figure 4.9: dependence of crystallite size on composition in the a) M synthesis and b) S synthesis

Again, similarities and differences between the two syntheses can be noticed: both syntheses lead to $ZnWO_4$ crystallites of sizes in the 27-32 nm range, with a more pronounced increasing trend in the case of the S synthesis. The situation is quite different for WO_3 crystallites, which both intuitively show a maximum for minimum zinc concentration, but while in the M synthesis their size then decreases monotonously, for the S synthesis it reaches a minimum at the 1:9 concentration, and then at 2:8 increases.

Intrigued by the possibility of having obtained via our synthesis the unexpected phase $ZnWO_4$, we decided to investigate our samples deposited on silicon via Raman spectroscopy. Figure 4.10 shows the results for films obtained via the M synthesis, in which the peaks attributable to $ZnWO_4$ were more visible with respect to films from the S synthesis.

The large, offscale band around 520 cm^{-1} is due to the transverse optical phonon mode of the silicon substrate [113]. The vibrational peaks appearing at 69 and 135 cm^{-1} in the Raman spectrum are attributed to WO_3 lattice modes, while in the mid and high-frequency regions appear peaks corresponding to deformation and stretching modes [114], [115], [116]. The peaks at 806, 715, 304 and 272 cm^{-1} are typical Raman peaks of monoclinic crystalline WO_3, which correspond to the stretching vibrations of the bridging oxygen, and these are assigned to W–O–W stretching (ν), and O–W–O bending (δ). While the peaks at 806 and 715 are slightly blueshifted with respect to the literature, the one at 304 shows a redshift of around ~18 cm^{-1}. In [116] there is a noticeable blueshift with increasing annealing temperature, which can explain our blueshifts due to our relatively high annealing temperature. According to [115], the band at 940 cm^{-1} is attributable to the stretching of terminal W=O bonds, common to all types of tungsten trioxide hydrates, and in the reference appears only at low

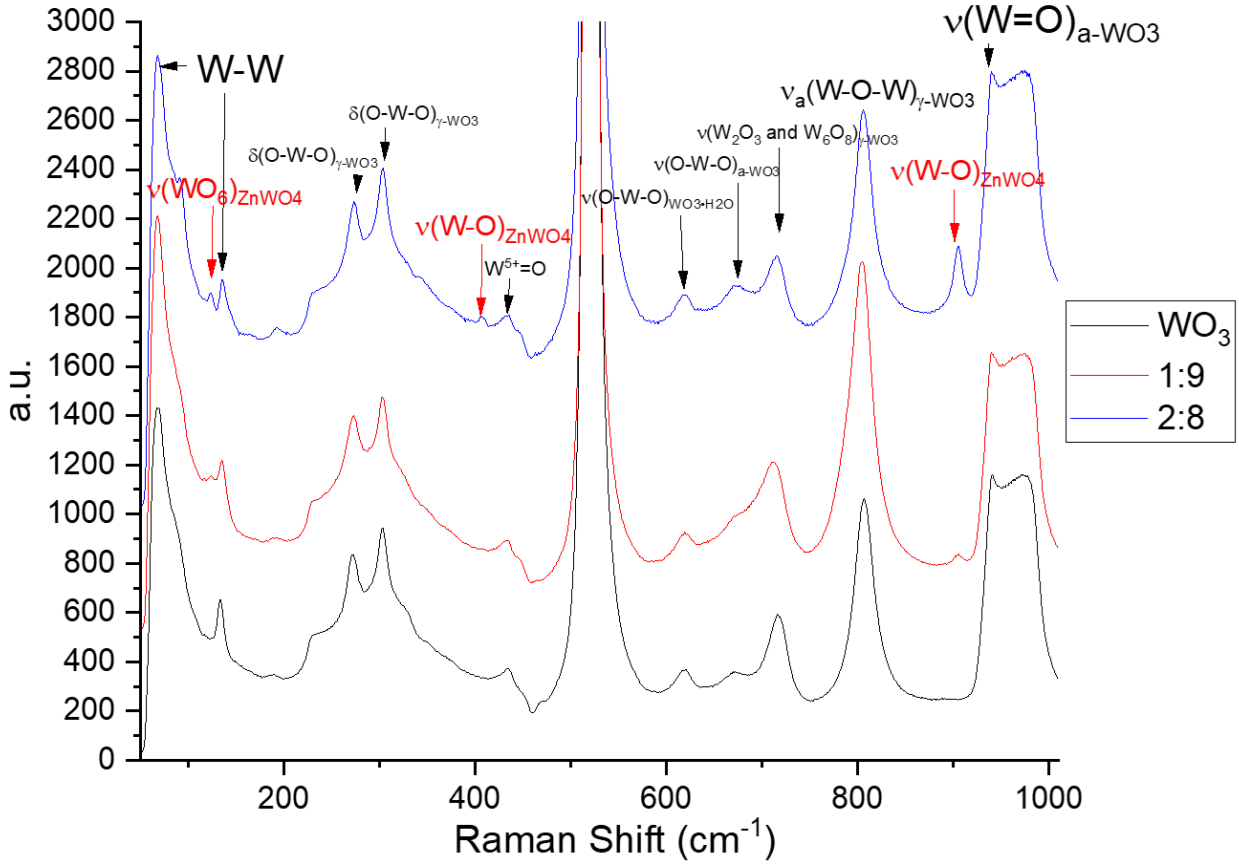

Figure 4.10: Raman spectroscopy of M-synthesis samples

annealing temperatures, while in ours is still visible after annealing at 550°C. This band is proof that our samples still contain a fraction of amorphous hydrated WO_3. Another hint of the presence of such an amorphous phase is given by the peak at 668 cm^{-1}, which [115] assigns to the stretching O–W–O modes of bridging oxygen, and it decreases in intensity with increasing annealing temperature. Furthermore, our graph presents another peak at 620 cm^{-1} attributable not to crystalline monoclinic WO_3, but in this case to its hydrated form, $WO_3 \cdot H_2O$, and in particular to the O–W–O stretching of the bridging oxygen. The small band at 435 cm^{-1} is attributed by [114] to the W^{5+}=O bond, due to the presence of oxygen vacancies together with mixed valence states of tungsten introduced when the sample is annealed in air, as was our case. Most important to our discussion is the peak located at 904 cm^{-1}, which is absent in pristine WO_3 and becomes more intense with growing zinc concentration. This peak is identifiable as one of the modes with A_g symmetry of $ZnWO_4$ [117], [118], being its band with higher intensity, and in particular to one of the six internal stretching modes of the six W–O bonds in the WO_6 octahedra. Other bands, barely visible,

that could be assigned to $ZnWO_4$ is the one at 405 cm^{-1}, absent in the WO_3 sample, which could be another A_g stretching mode of W–O, and the one at 123 cm^{-1}, attributed to an external mode of A_g symmetry related to lattice vibrations of WO_6 octahedra. Instead, no peaks attributable to ZnO could be identified as emerging with increasing zinc concentration [119], [120]. This reinforced our belief that our syntheses led to a $ZnWO_4/WO_3$ heterostructure instead of a ZnO/WO_3 one, while giving us further insight into the structure of our samples. The fact that the W^{5+}=O bond band remained very similar across all samples could hint that the number and local ordering of oxygen vacancies remain similar in the γ-WO_3 phase, which provide active sites for the gas sensing reaction [73] and thus that the variation of sensor response, which will be discussed later, depends more on the presence of $ZnWO_4$ and how it forms an heterostructure with WO_3.

4.2.2 Effect of synthesis on morphology

SEM microscopy was employed to investigate the influence of the different synthetic routes on the morphology of the films.

Figure 4.11 shows the SEM images of the films obtained respectively with M and S synthesis, with the histogram of the particle length distribution measured in nanometers under each image, and Table 4.5 presents some statistical estimates to assess the grain size distribution in each sample.

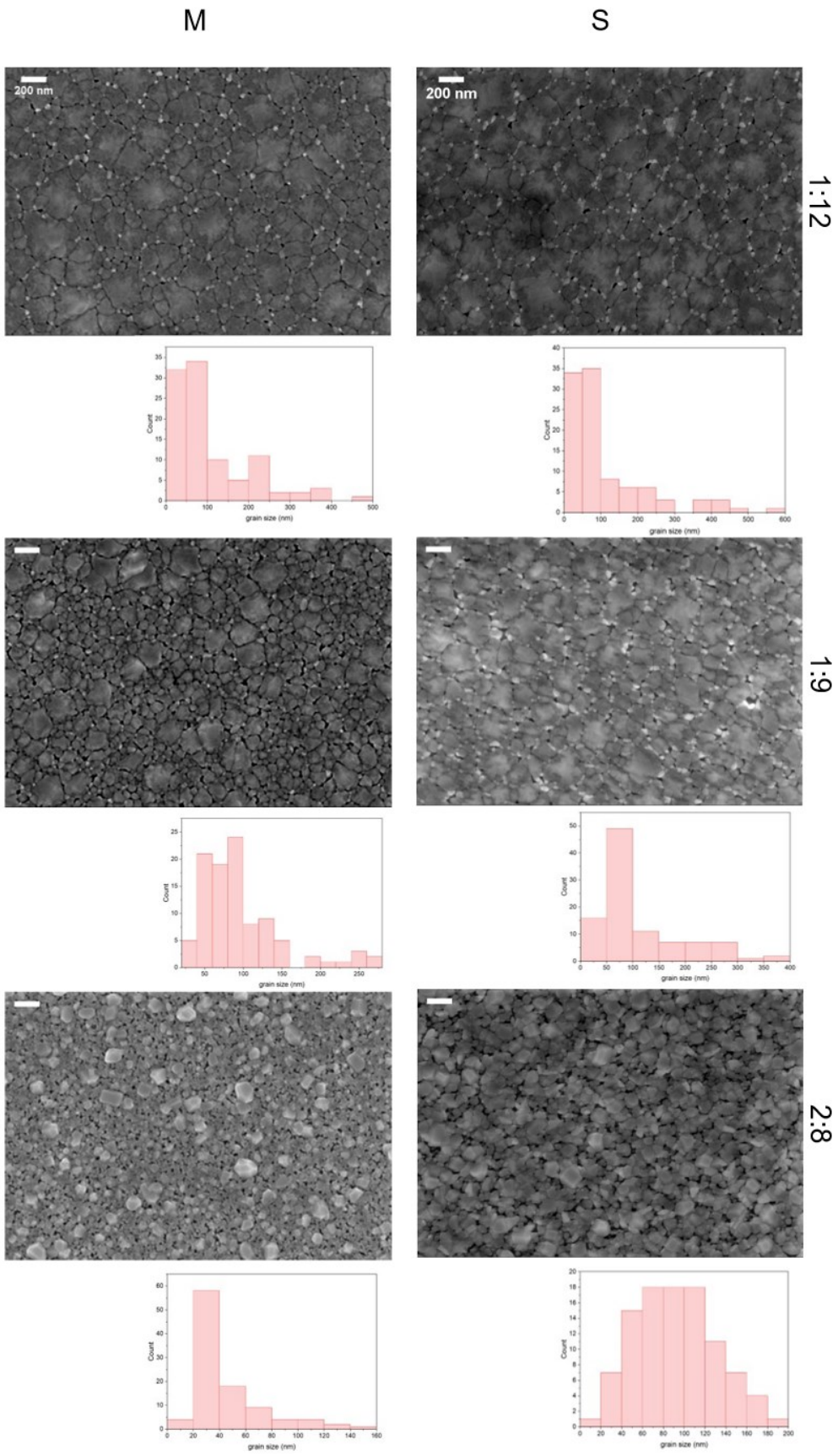

Figure 4.11: SEM images of different composition for synthesis M (left) and S (right) and the correspondent grain size distribution.

Composition	Synthesis	Grain size average (nm)	Grain size mode (nm)
1:12	M	107	45
1:9	M	96	40
2:8	M	45	28
1:12	S	114	48
1:9	S	111	61
2:8	S	91	102

Table 4.5: statistical estimators for grain size in our samples according to synthesis and composition

As in the previous experiments, the grain size distribution depends on the zinc content: the increase of zinc leads to a grain refinement effect and an increase in surface roughness. A similar increase in roughness when zinc content increases from 0.1 to 0.2 mole fraction has been reported in literature [76]. Another common element to both syntheses is the fact that the grain size distribution become narrower, with the maximum grain size decreasing with increasing zinc. In the M synthesis, the barycenter of the distribution shifts slightly to higher diameters, while remaining decidedly right-skewed; the average grain size remaining greater than the modal grain size, but both decrease monotonously. Instead, in the S synthesis, the shape of the distribution changes, with the average decreasing while the mode increases. The distribution becomes decidedly more symmetrical in the 2:8 sample, in which the average is lower than the mode. Another difference between the syntheses can be found in the fact that while the 1:12 samples have similar appearances and grain size distributions, their equivalent 1:9 samples already show differences, with a grain refinement effect stronger in the M synthesis than in the S one.

Confronting the crystallite sizes discussed above with these results on grain size can lead to interesting insights. For instance, it is clear that the larger grains must be either polycrystalline or contain both amorphous and crystalline phases. With the $ZnWO_4$

crystallites being smaller than WO_3 ones for all samples except MQ3 (2:8 M), it is reasonable to suppose that the $ZnWO_4$ ones must be found either in the smaller grains surrounding the larger ones or inside polycrystalline large grains. For the same reasoning, WO_3 crystallites are more likely to be found inside large grains. Unfortunately, the resolution of our SEM microscope wasn't sufficiently high to perform an elemental mapping and confirm these suppositions. Nevertheless, if this reasoning is sound, then it's likely that the more the grain size distribution is right-skewed, the more likely is $ZnWO_4$ to be found in small, mono- or oligocrystalline grains. The more this happens, the more likely WO_3/$ZnWO_4$ grain boundaries are to be formed with respect to WO_3/ WO_3 ones. In other words, having a large difference in size between grains makes more likely that the smaller grains are composed entirely of the phase with the smaller crystallite. Based on the gas sensing data presented below, it could be supposed that these grain boundaries are beneficial to the sensor's response.

4.2.3 Effect of synthesis on gas sensing

To assess the sensing behavior of the prepared samples, both static and dynamic tests were performed using air as a recovery gas. Table 4.6 describes the samples on which the following tests were performed.

Name	Synthesis	Composition (Zn:W)	Composition ($moles_{Zn}/moles_{(W+Zn)}$)	Thickness (nm)	Refractive index at 500 nm
N1		WO_3	0	25	2.3
MQ1	M	Zn:W 1:12	0.077	28	2.2
N3	M	Zn:W 1:9	0.1	31	2.0
N5	M	Zn:W 2:8	0.2	65	1.8
U2	S	Zn:W 1:12	0.077	35	2.0
U3	S	Zn:W 1:9	0.1	41	1.9
U4	S	Zn:W 2:8	0.2	35	2.0

Table 4.6: samples investigated via static gas sensing.

It can be noticed form the table that our composite films are generally not too much thicker than pure WO_3 ones, with the notable exception of N5. One possible explanation is the fact that, having ZAD an higher molar mass than metallic tungsten, with increasing zinc content there is an increase in overall mass, making the sol more viscous and the film thicker. In particular, N5, with its particularly low refractive index hinting at lower crystallization, might have started to form the gel particularly early, leading to an anomalously high thickness. The lower refractive index can also be due to the increased presence of zinc, with the final refractive index an average between the values of the pure materials.

Figure 4.12 shows, as examples, the results of the static gas sensing tests performed respectively on MQ1 and N1. It can be seen there that the composite film has a better response than pure WO_3 in terms of OAC, which it is the difference between absorbance under H_2 and absorbance under air. It is evident that the same wavelength-dependent response is observed, with the largest OAC appearing in the NIR range, peaking around 870 nm. This is proof of the gasochromic effect: in fact, our films turned blue upon exposure to hydrogen. Note that there is a lesser but still noticeable variation of absorbance at about 270 nm, which could be due to the excitement of electrons from the valence band to the conduction band.

Figure 4.13 presents the curves for OAC obtained from static gas sensing measurements performed as above on samples from Table 4.6. Across both syntheses, the same trend is noticeable, an increase of response with decreasing zinc concentration. A secondary maximum can be observed around ~270 nm, which could be associated with the formation of a heterojunction between WO_3 and $ZnWO_4$ and a modulation of the bandgap. It might seem counterintuitive to suppose that with decreasing $ZnWO_4$ this electronic effect becomes more important, but, as the SEM images showed, with less zinc content the surface became less rough [76], and it has been proven that the band gap of WO_3 decreases with decreasing surface roughness [121] and decreases upon zinc doping [122]. Morphological effects might be in play also at the aforementioned wavelengths for gasochromism: the enhanced response of the 1:12 samples might be explainable by the favourable combination of the high porosity of the film, allowing for easier hydrogen adsorption, and high WO_3 crystallite size, which should be proof of large, homogeneous WO_3 crystals, contributing positively to the OAC. This interplay between morphological effects could be confirmed by Figure 4.14, plotting OAC at 870 nm against zinc concentration for both M and S-synthesized samples and confronts them with the OAC of a pristine WO_3 sample at the same wavelength.

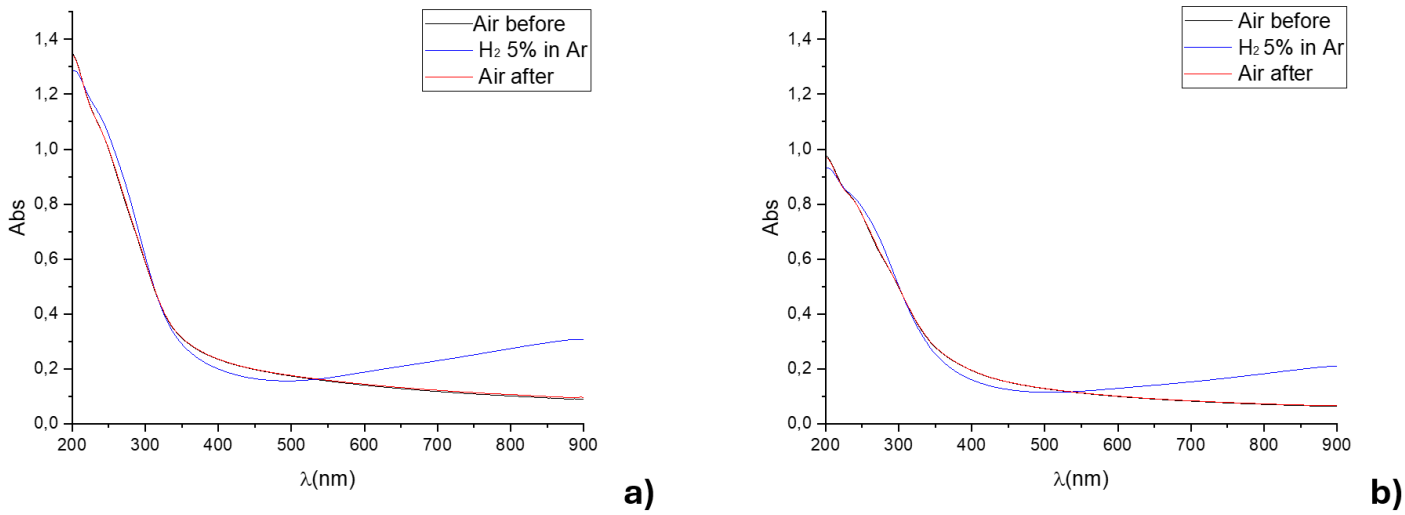

Figure 4.12: static hydrogen sensing a) on MQ1 (1:12 M) and b) on N1 (WO_3)

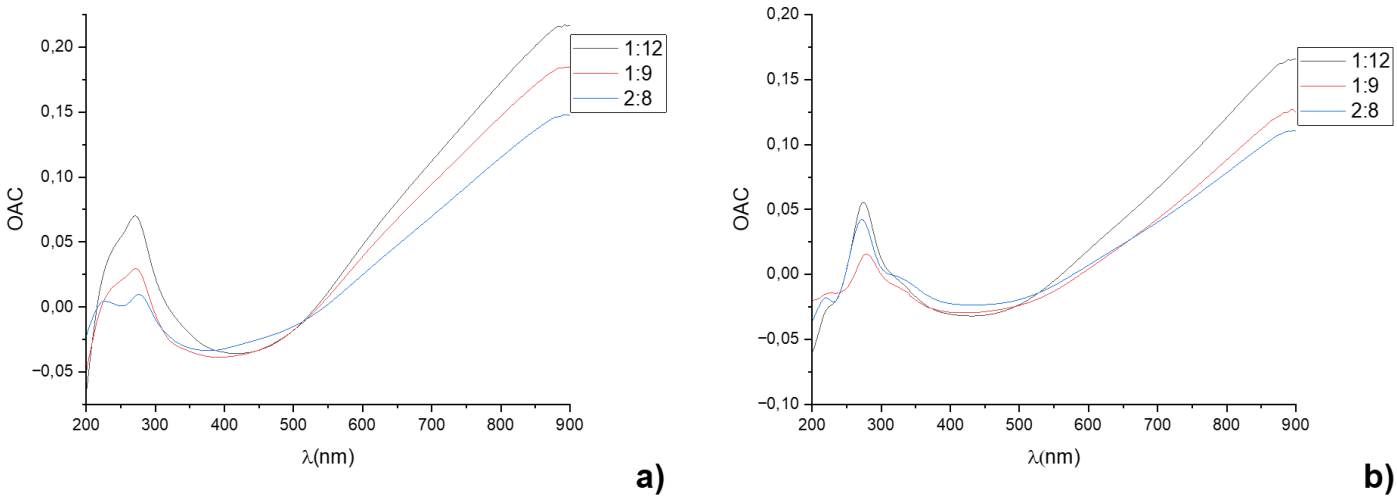

Figure 4.13: OAC as a function of Wavelength for samples obtained via a) the M synthesis and b) the S synthesis

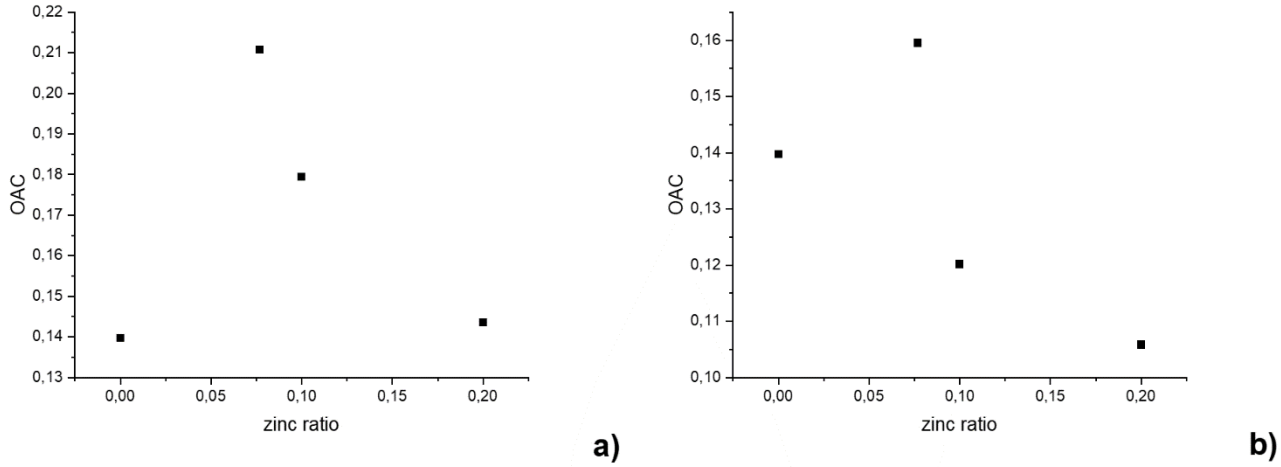

Figure 4.14: OAC at 870 nm against zinc concentration for a) the M synthesis and b) the S synthesis

In both syntheses, the 1:12 sample performs better than pure WO_3, showing a higher OAC. It seems that for higher zinc concentration, the S synthesis samples perform worse than pure WO_3 and the M synthesis in general. Nevertheless, the same trend can be observed, which lead us to ask ourselves if a maximum for OAC could be found between the Z:W molar ratios of 0 and 0.077 (corresponding to 1:12).

The next step, of course, was to effectuate dynamic gas sensing tests to visualize whether the synthesis had any effect on the response and recovery of the sensors, and how temperature differently affected the gas sensing behavior in either synthesis. Figures 4.15-4.17 present dynamic tests performed respectively on MQ1, U2 and U3, and Tables 4.7-4.9 report the gas sensing properties calculated for these samples.

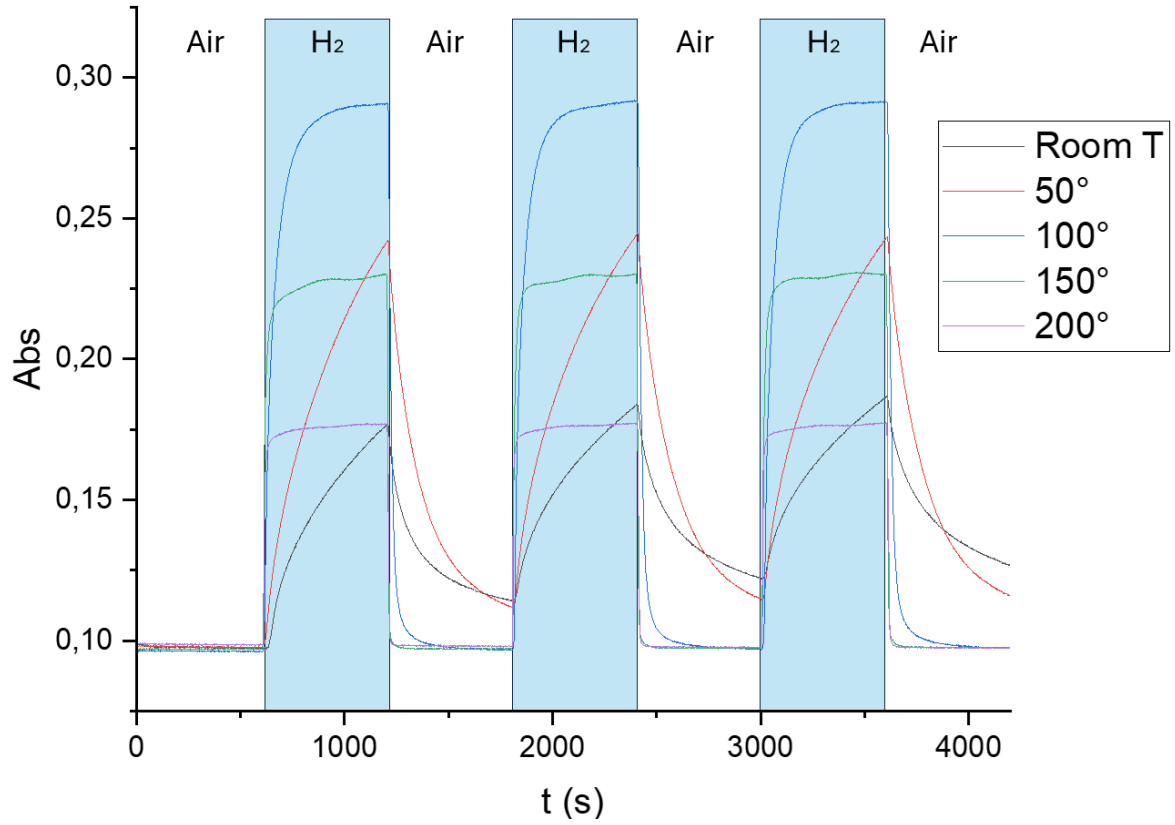

Figure 4.15: dynamic gas sensing tests on MQ1 (1:12 M)

Temperature	$\Delta Abs_{\lambda=870nm}$	$t_{response}$90% (s)	$t_{recovery}$90% (s)
Room T	0.071	N/A	N/A
50°	0.135	N/A	N/A
100°	0.195	135	53
150°	0.133	44	12
200°	0.079	20	17

Table 4.7: Gas sensing parameters dependence on temperature in MQ1 (1:12 M)

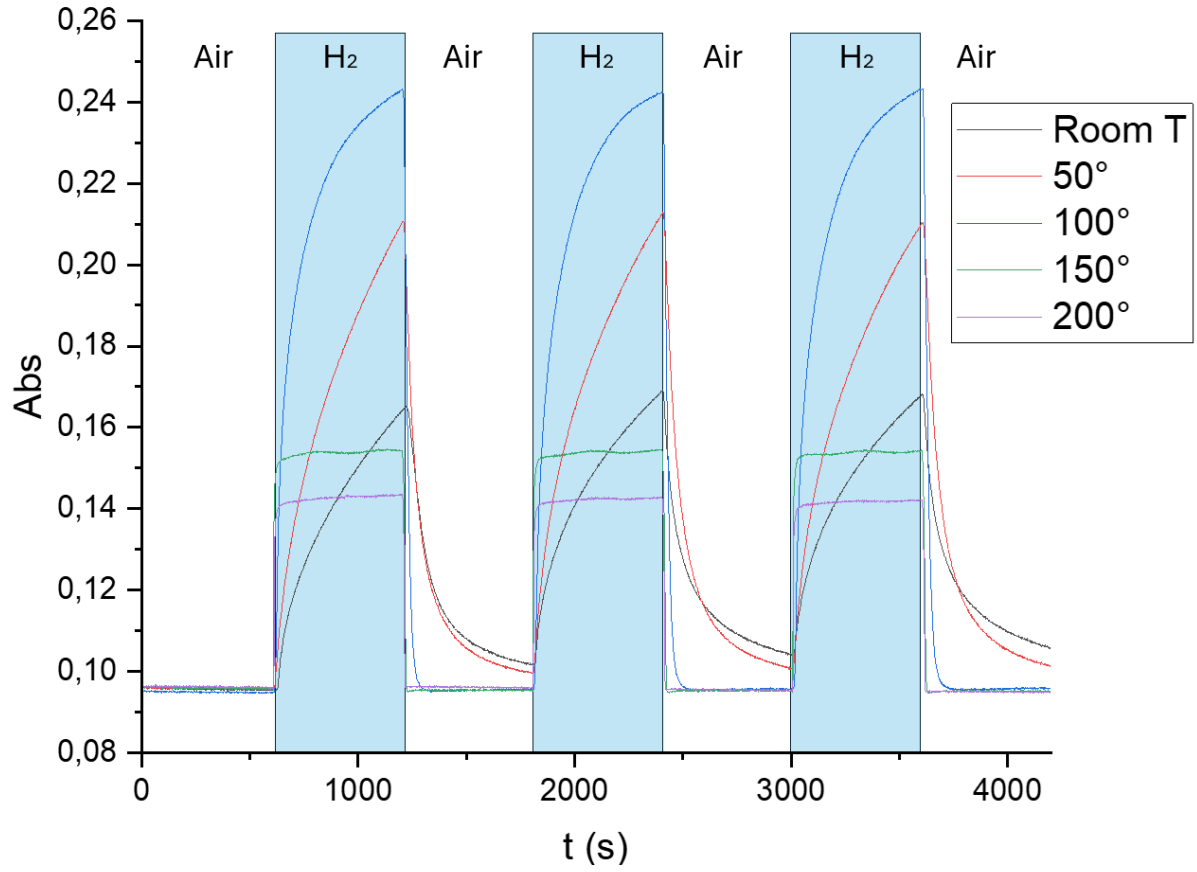

Figure 4.16: dynamic gas sensing tests on U2 (1:12 S)

Temperature	$\Delta Abs_{\lambda=870nm}$	$t_{response}90\%$ (s)	$t_{recovery}90\%$ (s)
Room T	0.067	N/A	N/A
50°	0.112	N/A	N/A
100°	0.147	N/A	46
150°	0.058	13	19
200°	0.047	15	13

Table 4.8: Gas sensing parameters dependence on temperature in U2 (1:12 S)

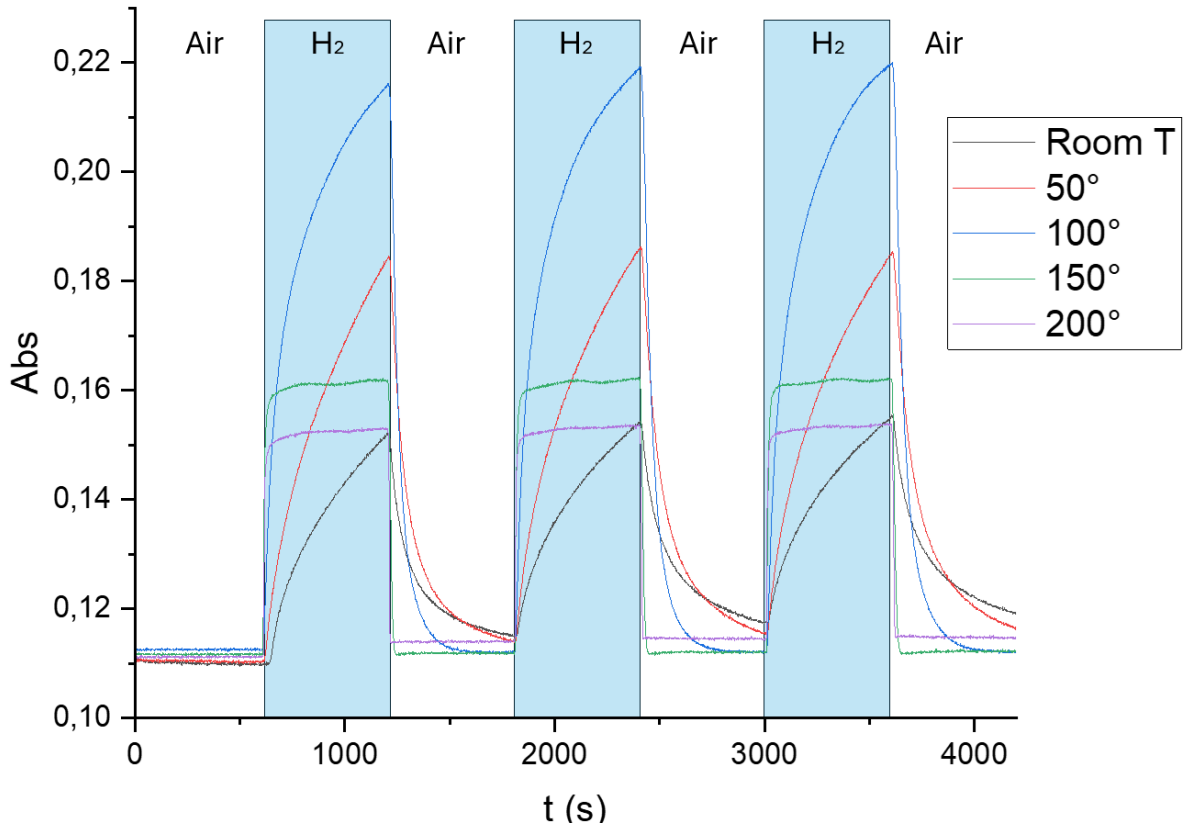

Figure 4.17: dynamic gas sensing tests on U3 (1:9 S)

Temperature	$\Delta Abs_{\lambda=870nm}$	$t_{response}$90% (s)	$t_{recovery}$90% (s)
Room T	0.040	N/A	N/A
50°	0.072	N/A	N/A
100°	0.106	N/A	139
150°	0.050	22	27
200°	0.040	18	13

Table 4.9: Gas sensing parameters dependence on temperature in U3 (1:9 S)

Many considerations can be made on these results. First, it is evident that using Air as a recovery gas allows for a more complete recovery of the baseline compared to Ar, improving with decreasing zinc concentration. This is due to the removal of chemisorbed hydrogen

upon reaction with oxygen, which allows recovery of the baseline at temperatures as low as 100°C. A similar trend with temperature can be noticed across all samples: starting from room temperature to 50°C, the response is low in terms of $\Delta Abs_{\lambda=870nm}$ and then increases, reaching a maximum at 100°C. Okazaki and coworkers [123] report a similar rising trend of optical response with temperature for their sol-gel WO_3/Pt films up to 80°C. Then, in our films, the response decreases as the temperature is further raised. It is interesting to note that, for samples from the S synthesis, there is no saturation of the response at 100°C, which instead has been observed in the sample from the M synthesis. Mazur et al. [124] report, for their sputtered WO_3/Pt thin films, fast response and absence of saturation after 9 minutes at 150°C for concentrations of hydrogen higher than 1000ppm, so we could argue that the presence of zinc improves signal saturation, with 1:12 showing better saturation than 1:9, and that the M synthesis promotes saturation at lower temperatures. We might further argue that this saturation improvement is not due to a morphological effect, since for the 1:12 composition, both syntheses show a very similar morphology, as seen in the SEM images. In terms of $\Delta Abs_{\lambda=870nm}$, MQ1 showed the best performance, which we can attribute to a better-performed deposition, since it was fabricated later with a more accurate substrate cleaning procedure: in fact, it presents a higher refractive index hinting at better crystallinity. We were in fact able to replicate a similar $\Delta Abs_{\lambda=870nm}$ with a later sample obtained via S synthesis, as will be shown later. Concerning the response and recovery speed, the samples had slow and incomplete responses under 100°C. According to [125], the slower response at lower temperatures is due to the rather slow desorption of the water molecules formed by reaction of hydrogen with oxygen. The S synthesis displayed faster response times and comparable recovery times. The S samples had much faster response at 150°C than at 100°C, and remained similar in speed at 200°C. By contrast, for the M synthesis the response speed seems to steadily increase with temperature. It is argued in [123] that the increase of response speed with temperature could prove that the mechanism of WO_3 reduction would be controlled by the diffusion of the reactants, such as dissociated hydrogen atoms or protons. If this was true, then this might hint that the two syntheses produce films in which the coloring reaction has different types of control: it could be diffusion-controlled for films from the M synthesis, and surface reaction controlled for films from the S synthesis, with an activation temperature somewhere between 100°C and 150°C. Concerning the influence of composition in the S synthesis, not only $\Delta Abs_{\lambda=870nm}$, baseline recovery and saturation but also response and recovery times worsen with increasing zinc concentration.

The only advantage of the 1:9 composition with respect to the 1:12 is that it shows a response similar in $\Delta Abs_{\lambda=870nm}$ at higher temperatures, albeit with slower kinetics.

We performed a test to determine whether the U2 sample could reach saturation even after 15 minutes of exposure to hydrogen at 100°C, portrayed in Figure 4.18. As shown, the samples never reached the plateau even after 15 minutes of exposure to H_2. Still, it is interesting to note that a full recovery was nonetheless achieved even after 15 minutes of exposure, which shows promise for the stability of the sensor.

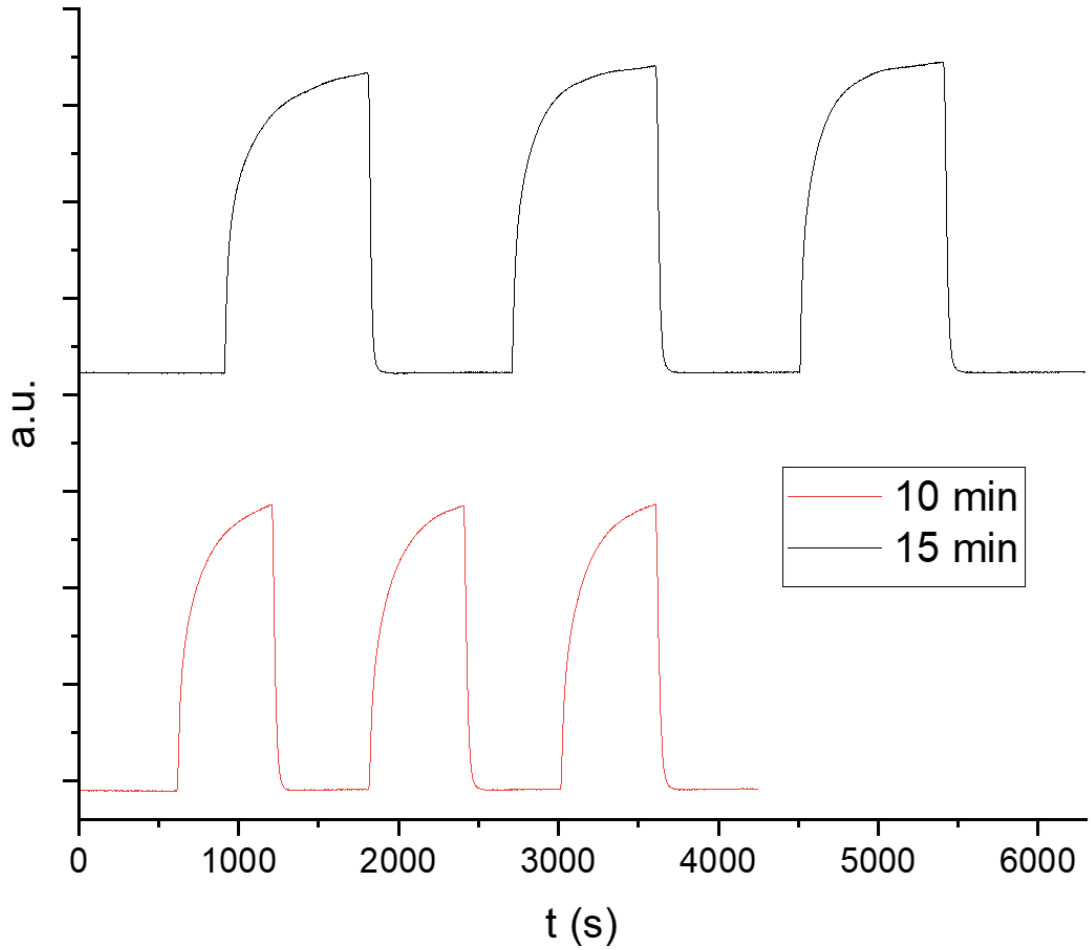

Figure 4.18: comparison of two different dynamic tests with different cycling times performed on U2.

4.3 Effect of zinc concentration

We were next interested in further studying the dependence of gas sensing properties on zinc concentration. For this purpose, we synthesized a series of samples according to the S synthesis, for various reasons. First, it requires less work, since as was discussed in the Methods chapter, the ZAD is mixed directly into the WO_3 sol, saving time. Second, the S synthesis showcased better response and recovery times, and even though U2 had a lower response in general than MQ1, we were convinced that the quality of the film plays a major influence on response. Thus, we were confident that with a more rigorous deposition procedure, and especially with better substrate cleaning, since it was at this point that we added the first rinsing step before sonicating, we could obtain via the S synthesis a sample with an OAC and $\Delta Abs_{\lambda=870nm}$ on the order of 0.19-0.20, and in the meanwhile experiment with different molar ratios.

4.3.1 Effect of zinc concentration on crystal structure

We prepared samples according to Table 4.10 and characterized them first via GIXRD. Figure 4.19 shows their diffraction patterns.

Name	Synthesis	Composition ($moles_{Zn}/moles_{(W+Zn)}$)	Thickness (nm)	Refractive index at 500nm
F1	S	0	34	2.3
F2	S	0.017	34	2.2
F3	S	0.042	35	2.2
F4	S	0.067	36	2.2
F5	S	0.072	35	2.2
F6	S	0.087	36	2.1

Table 4.10: samples prepared for the study on composition

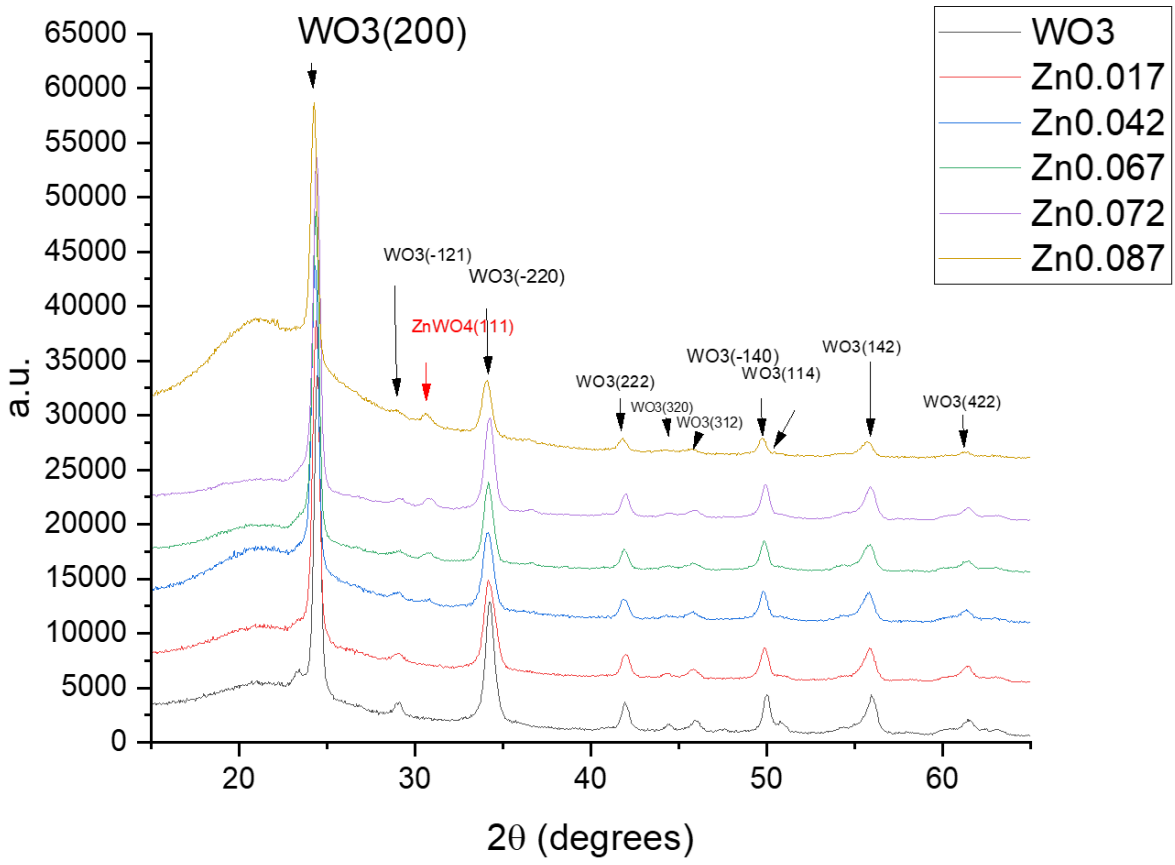

Figure 4.19: the GIXRD patterns of the F series samples.

Again, the patterns show peaks indexed to monoclinic WO_3 (JCPDS number 83-0950 [109]), except for the (111) monoclinic $ZnWO_4$ (JCPDS number 73-0554 [110]). These samples show a strong (200) orientation for the WO_3 phase, with the (002) peak visible only in pure WO_3, in agreement with the previous results. The emergence of the (111) $ZnWO_4$ starts at Zn0.042, but it becomes well-defined only at Zn0.067. The development of the $ZnWO_4$ phase seems to have some influence on the growth of certain WO_3 crystal planes, as the (320) and (312) peaks become broader and less intense, indicating that those crystal planes become less well-defined and could present a higher concentration of defects. Once again, we performed an analysis of the average crystallite size through Scherrer's equation, presenting the results in Figure 4.20.

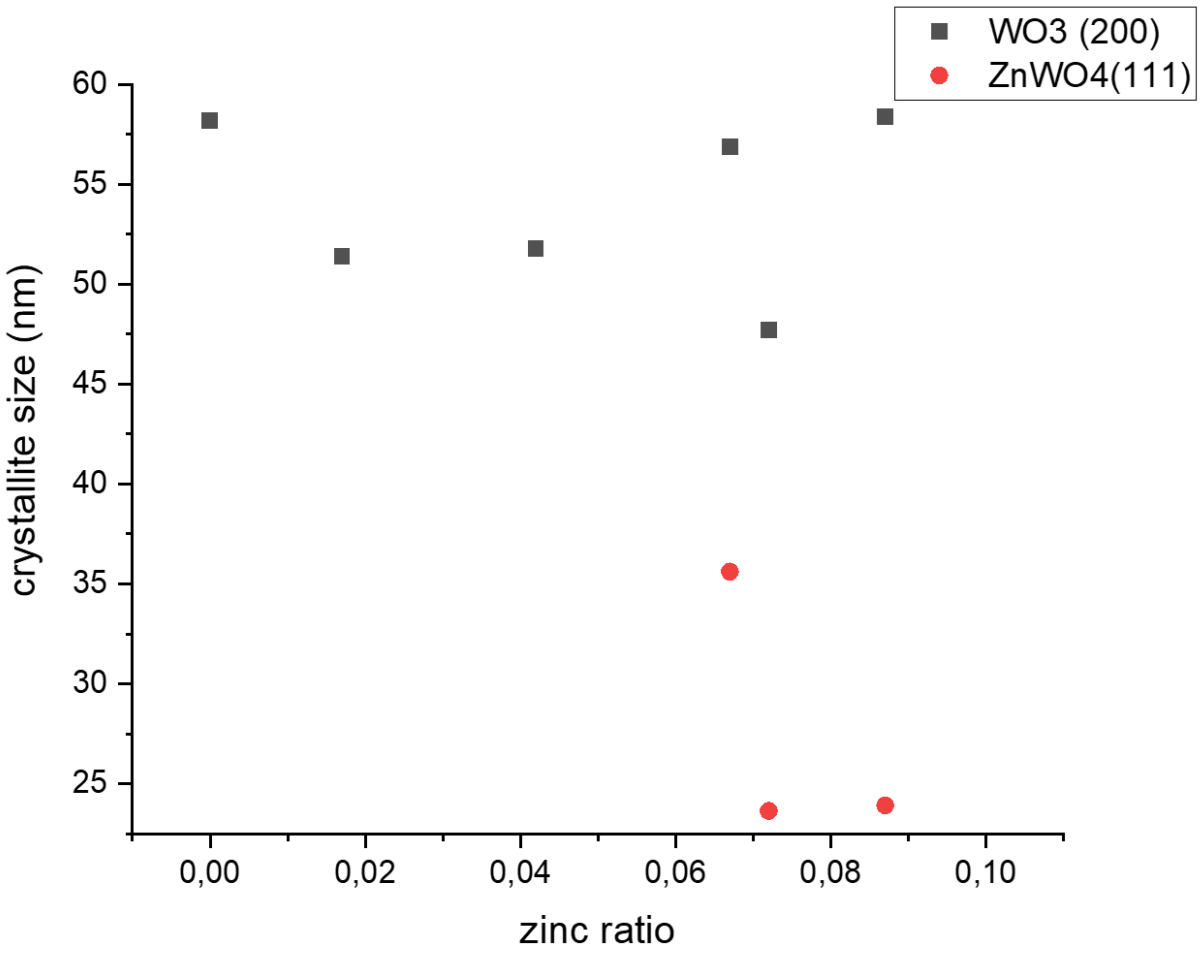

Figure 4.20: dependence of the average crystallite size on zinc ratio in the F series.

The figure shows again that the crystallite size of WO_3 decreases to a minimum with increasing zinc concentration and then rises in a similar trend to earlier data, but this time the minimum is found at a different zinc ratio. The values have remained similar, around 50 nm for WO_3 and 30 nm for $ZnWO_4$, but the latter one with decisively more variance, proving that there may other factors at play in deciding the exact size of $ZnWO_4$ crystallites, such as crystal cell deformation. Still, the general behavior is conserved, with WO_3 crystallites about twice as large as $ZnWO_4$ crystallites. This leads us to believe that the WO_3 crystallite size obtained for F5 (Zn 0.072) is too small and that data point might be an outlier, together with the fact that its (200) peak is quite broad and more difficult to resolve with respect to the other samples.

4.3.2 Effect of zinc concentration on morphology

As in our earlier studies, we performed SEM measurements to assess whether low zinc concentrations had any influence on the morphology. The results are presented in Figure 4.21. Since, in contrast with earlier experiments, these micrographs were obtained on samples over which platinum had already been deposited, it is possible to notice the Pt NPs as the small, bright dots. This confirms that our experimental procedure leads to a uniform coverage of Pt NPs over all the films, as images taken at different scales and on different spots confirmed. Turning our attention to the effect of zinc on morphology, it is clear that these small concentrations of zinc cause a small but still noticeable effect. The pure WO_3 film presents large, compact grains, with very small pores between them. As the concentration of zinc increases, grain refinement takes place, with the emergence of very small grains in between the large ones, and porosity increases. As the amount of zinc is increased further, the grain size distribution changes, with the largest grains becoming smaller and the smallest ones decreasing in number, as discussed above. This is in good agreement with our previous results. The increase in porosity for very low concentrations of zinc can be a justification for the improved gas sensing performance of composite films, as is discussed below.

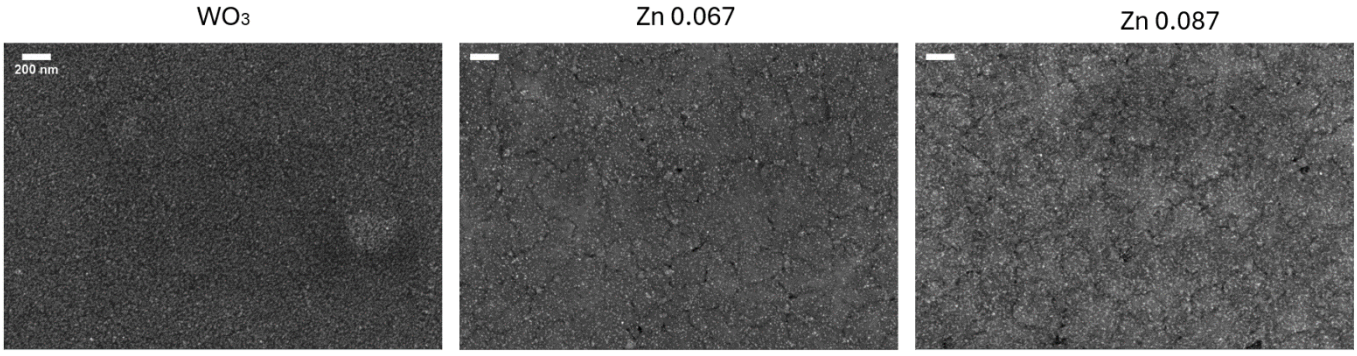

Figure 4.21: SEM micrographs of samples F1, F4, and F6 (left to right)

4.3.3 Effect of zinc concentration on gas sensing

Figure 4.22 shows the OAC spectra obtained from static gas sensing tests run on samples F1-F6, performed according to the previous protocol at 100°C.

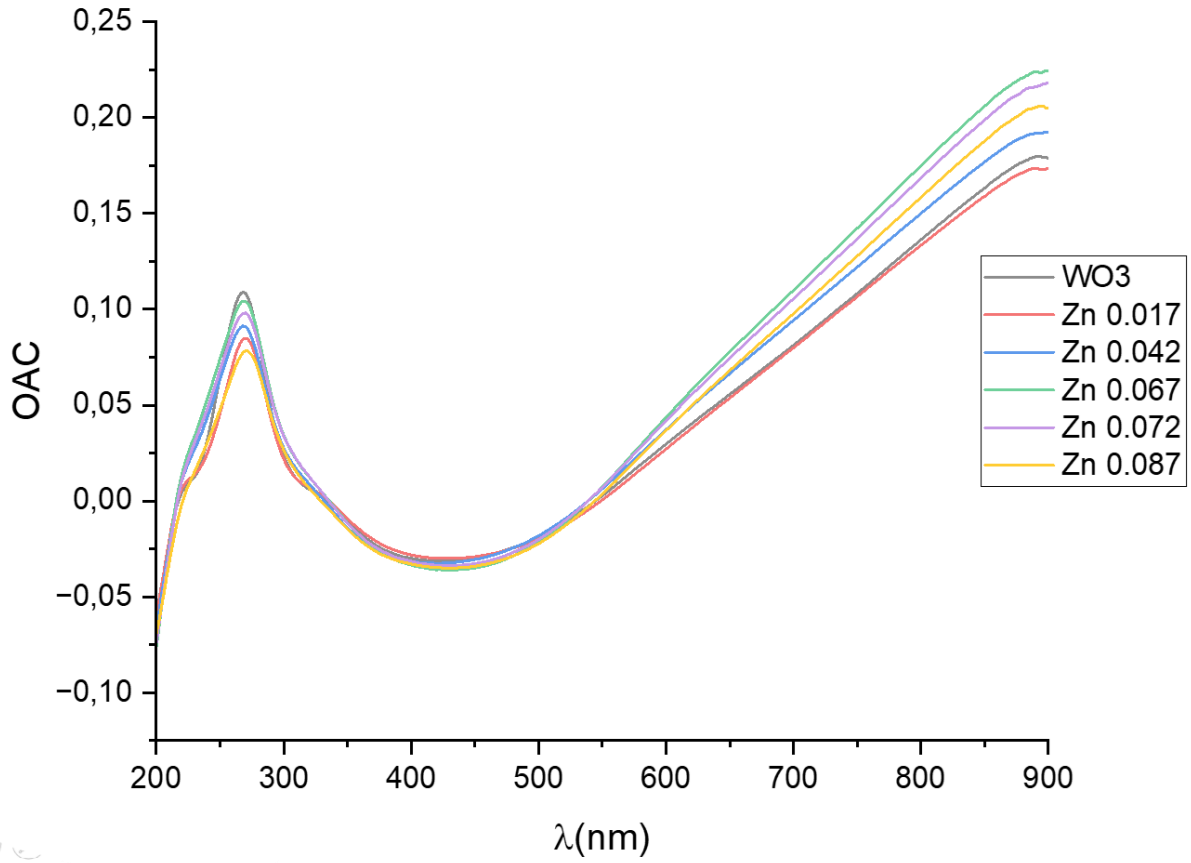

Figure 4.22: dependence of OAC on composition and wavelenght in S-synthesis samples

As the graph evidences, the 0.067 Zn sample shows the highest absorbance variation at the wavelength of our interest, confirming itself as the best molar ratio for a high response in an optical gas sensor working at 870 nm.

It's interesting to note that all the films instead performed slightly worse at 270 nm than pure WO_3, suggesting that this synthesis produces heterostructures between WO_3 and $ZnWO_4$ that cause a decrease in absorption change in the NUV range. However, there is little variation of OAC with composition in the range 380-470 nm, corresponding to the bandgap of pristine WO_3, depending on its crystallinity [20]. So, promotion from deep within the valence band is inhibited by the formation of the heterostructure, but transitions around the band gap maintain more or less the same probability. This could be explained by mid-gap trap states generated by the formation of the $WO_3/ZnWO_4$ heterostructure which provide a different excitation pathway for light absorption, diminishing absorbance at short

wavelengths. It has been proven that the formation of oxygen vacancies associated with the formation of a $WO_3/ZnWO_4$ composite leads to a negative shift of the valence band [126], and that these vacancies create states within the forbidden gap of WO_3 allowing for new electronic transitions between different oxidation states of the vacancy [127]. The formation of such trap states should not hinder gasochromism, since the absorbance at NIR wavelengths is due to transitions between small polaron bands [33]. It is reasonable to assume that this tuning of OAC observed in this series of samples is mostly due to composition, as these samples presented very similar thickness and refractive index, and thus a similar degree of crystallization.

Figure 4.23 reproduces the values of OAC at 870 nm, presenting a trend that complements and corroborates the ones found in our previous experiments. Apparently, very low concentrations of zinc produce a response that's very similar and, in the case of our Zn 0.017 sample, even worse than pure WO_3. Then, OAC rises with zinc ratio to a maximum for 0.067, and decreases for further increases of concentration. Note that, with this S synthesis, we were able at this point to obtain samples with a higher response than pristine WO_3, demonstrating an improvement in the general quality of our films with respect to earlier trials.

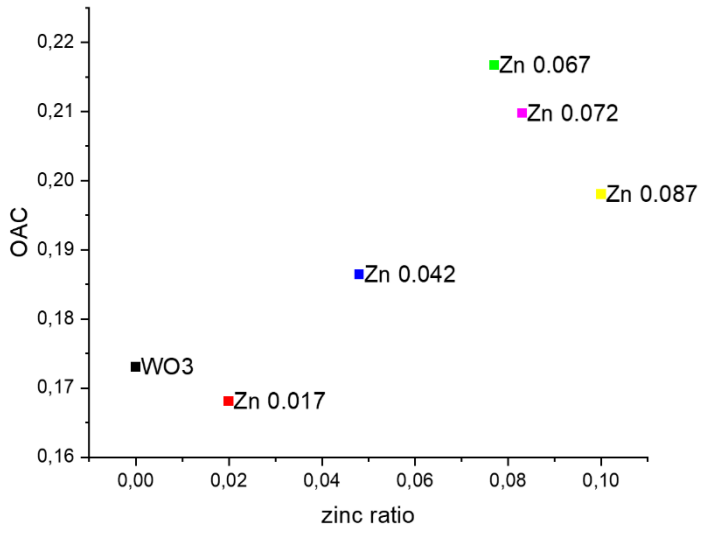

Figure 4.23: OAC at 870 nm against composition in S-synthesis samples

Taking into account the considerations previously discussed on $WO_3/ZnWO_4$ grain boundaries, we could propose an explanation for this trend. At low concentrations of zinc, few crystallites of $ZnWO_4$ form, as evidenced by the absence of the (111) peak under 0.042

zinc ratio, and thus few grain boundaries between the compounds, making the change in response small or even negative. With increasing zinc, these grain boundaries logically increase in number up to a maximum, after which the grain refinement effects of zinc take place, modifying the distribution of grains and thus increasing the probability that a $ZnWO_4$ crystallite is found inside a polycrystalline grain. The fact that WO_3 crystallite size reaches a minimum for low zinc concentration might compound on this effect, because it implies that more WO_3 crystallites will be found inside the large polycrystalline grains. In essence, we're arguing that for zinc ratio 0.067 the number of grain boundaries reaches a maximum, and that this can explain the improved gas sensing behavior of such a composition.

Since F4 (Zn 0.067) was the sample that showed the highest OAC in this series, we decided to perform on it dynamic gas sensing tests in the same conditions as those before. Figure 4.24 shows the data, while Table 4.11 presents the gas sensing parameters as a function of operating temperature.

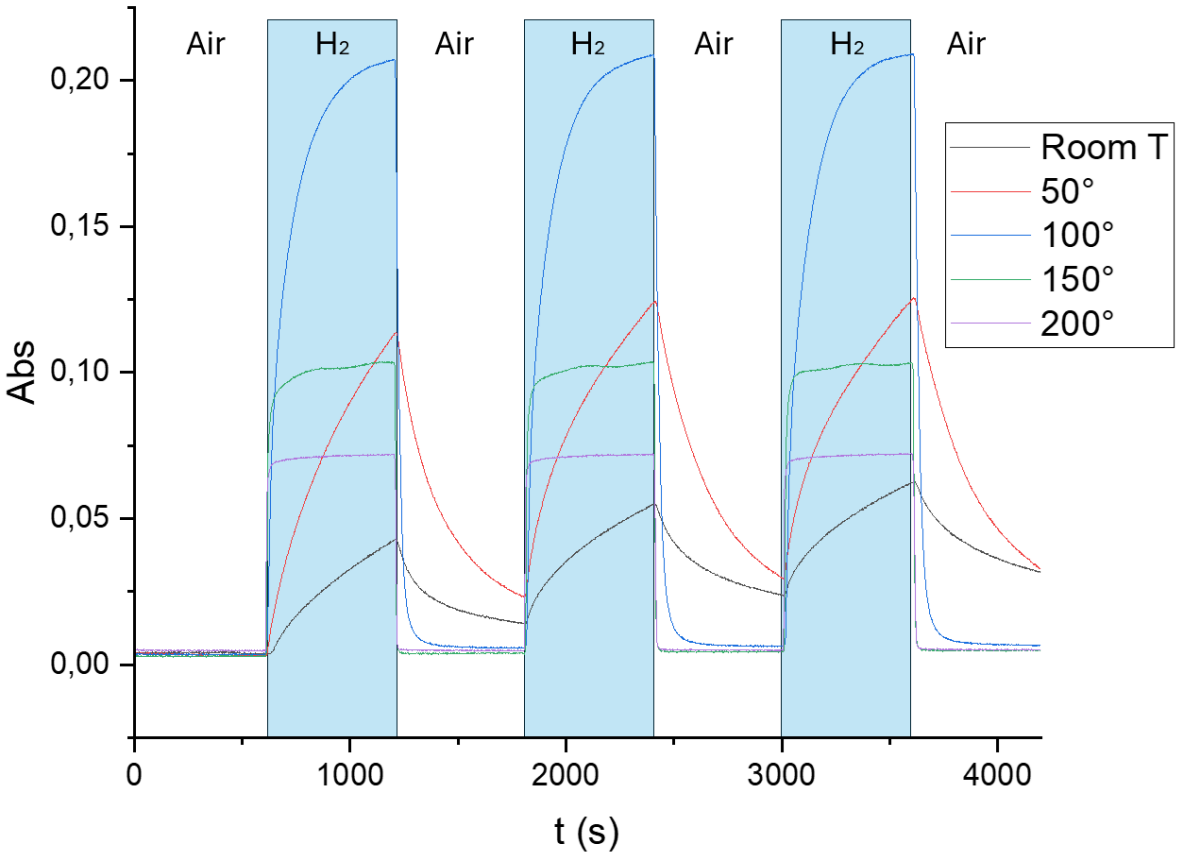

Figure 4.24: Dynamic gas sensing tests performed on F4

Temperature	$\Delta Abs_{\lambda=870nm}$	$t_{response}$90% (s)	$t_{recovery}$90% (s)
Room T	0.040	N/A	N/A
50°	0.100	N/A	N/A
100°	0.203	N/A	52
150°	0.098	32	12
200°	0.067	12	15

Table 4.11: gas sensing parameters of F4 as a function of temperature.

There are several considerations to be made on these data. First, it is noticeable that response at 100°C is more complete than in the earlier samples, in the sense that the absorbance curve becomes closer to horizontality. The trend of response (rising with temperature to a maximum at 100°C and then decreasing) is conserved in this sample. Positively, $\Delta Abs_{\lambda=870nm}$ at 100°C is even higher than the best-performing samples from previous tests. Instead at lower temperatures the response is both less intense, with lower $\Delta Abs_{\lambda=870nm}$, and less complete, as the curves still show a high slope at the end of each coloring cycle.

Concerning recovery, it is noticeable that this sample had an especially poor recovery at low temperatures. It is evident a baseline drift steeper at room temperature than at 50°C, indicating an incomplete return to the original bleached stated. Turning our attention to response and recovery speeds, we didn't manage to exactly reproduce our earlier results, but there are some similarities. The response and recovery times for this sensor are all equal or lesser than the ones obtained for samples via M synthesis in the same composition previously, confirming the improvement afforded by the S approach in this aspect. These results are mostly similar to the ones obtained for the previous S samples, with absorption and desorption kinetics improving with temperature leading to faster speeds, with the noticeable exception of the higher response time at 150°C. Nevertheless, these results prove that we were able to obtain a sensitive film with high $\Delta Abs_{\lambda=870nm}$ at 100°C and fast response and recovery times via the S synthesis, with the optimal zinc molar ratio being 0.067 to obtain the highest sensitivity.

4.3.4 Stability Test

To further characterize our film, we decided to perform a measurement with a higher number of cycles, to assess the repeatability of the response. We chose to perform this measure at 150°C, since our sensor had already showed a complete response/recovery at that temperature. We utilized the same Air/H_2 5% in Ar cycle as before but repeated 10 times. Figure 4.25 presents the results from this stability test.

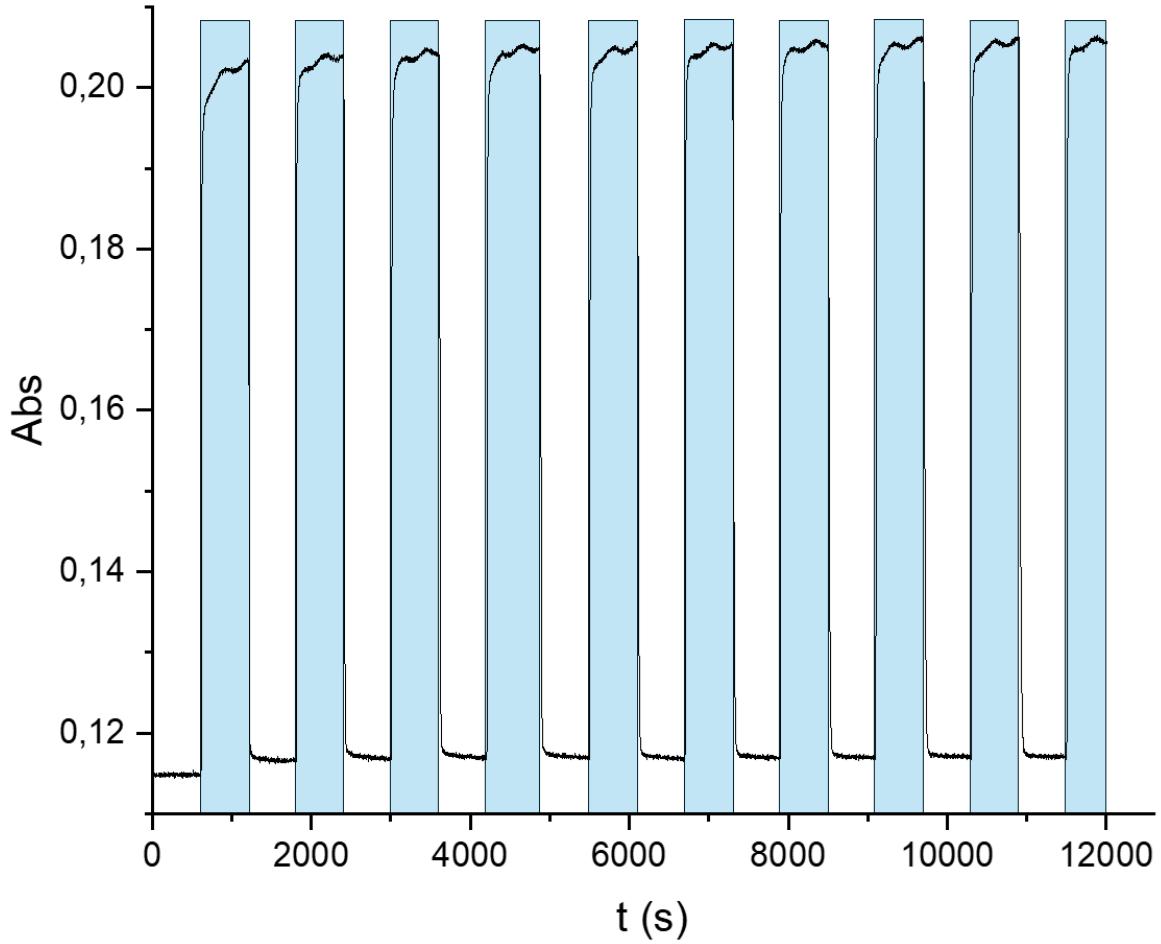

Figure 4.25: long-cycle stability of dynamic gas sensing in F4 (Zn 0.067)

First, it is noticeable that the $\Delta Abs_{\lambda=870nm}$ remains constant across the cycles, with an average $\Delta Abs_{\lambda=870nm}=0.0873\pm0.0005$, with deviations within 2% of the average value. The fluctuation in absorbance during the coloring cycles is due to fluctuations in H_2 flow during the measurement, which incidentally shows that our sample is able to respond to fast and continuous changes of H_2 concentration as long as they are small. There is no noticeable drift of the baseline, meaning that the bleached state is fully recovered each time. There is,

however, a change in response and especially recovery time across the cycles, as Figure 4.26 shows.

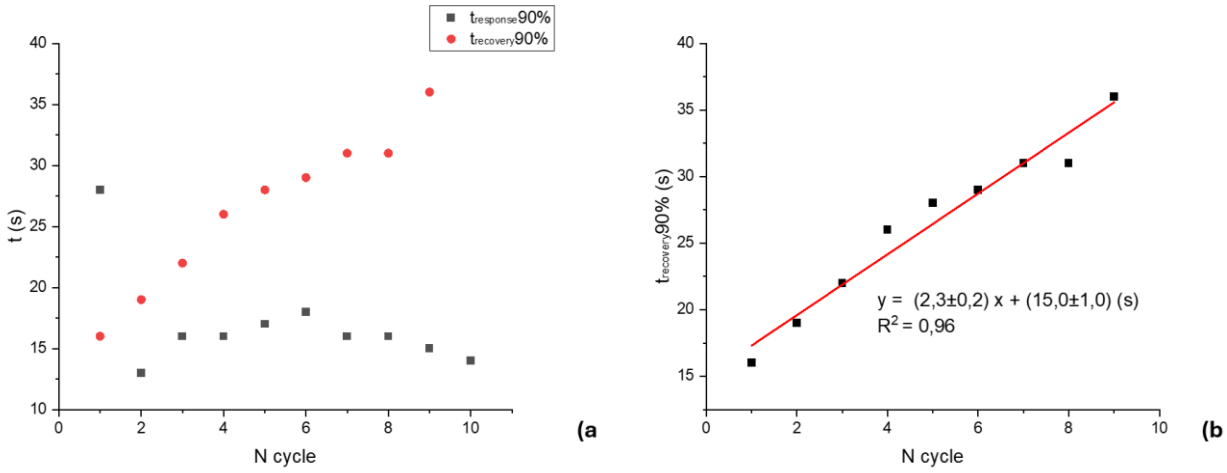

Figure 4.26: a) dependence of response and recovery times on the cycle number and b) linear fitting of the recovery time with cycle number

It is evident that response time is larger in the first cycle, and then stabilizes to lower values with some fluctuation upon subsequent cycles. This behavior might hint that in order to obtain the fastest response time in a future optical sensor, it should be activated by exposure to a trial cycle of H_2 and recovery gas.

A possible explanation for the dependence of recovery time from the number of cycles might be the diffusion of oxygen vacancies across the film. Georg and coworkers proposed a mechanism to explain the gasochromism of WO_3 called the “oxygen vacancy” model, according to which oxygen vacancies (V_O) and water are formed during the coloration process, and the V_O recombines with oxygen during the bleaching process [128]. Luo et al. further developed this model into the “localized water molecule” model based on their Raman spectroscopy studies on gasochromic behavior of WO_3 nanowires [129]. According to them, during the coloration process, the absorbed H_2 molecules dissociate into hydrogen atoms or ions on the Pt NPs, then the hydrogen species spillover onto the WO_3 surface and diffuse along pore surface or grain boundaries, intercalate into the lattice and form localized water and V_O. The bleaching process involves first the absorption and dissociation of oxygen molecules on the Pt nanoparticle. Then the oxygen ions diffuse inside and recombine with V_O. Based on these models, we can explain the reduction of response time after the first cycle and the linear increase of recovery time as follows. As the bleaching reaction proceeds, more and more oxygen ions recombine with V_O, decreasing their concentration at the surface of WO_3 particles. This creates a gradient of V_O concentration that attracts

vacancies from the core to the surface of the particle Thus, upon subsequent reexposure to H_2, there are more oxygen vacancies closer to the surface, providing more easily accessible active sites. Logically, upon subsequent cycles, this diffusion must become more difficult as the vacancies closer to the surface have already diffused towards it and thus it becomes harder and harder for V_O deep into the particle to diffuse from the core to the surface, as the vacancies already close to the surface repel them with their lattice distortion fields. In conclusion, this last measurement ensured us that our films presented good stability in terms of $\Delta Abs_{\lambda=870nm}$ and considerations on the variation of response and recovery time with the number of cycles provided us with useful insights for repeated use of our sensors.

Conclusion

Over the course of this thesis project, a thin film optical hydrogen sensor was developed via a facile sol-gel approach. In particular, a heterostructure composed of WO_3 and $ZnWO_4$ was deposited and was then functionalized via platinum nanoparticles. The optimal conditions for enhancing gas sensing properties with respect to pure WO_3 were determined in terms of ageing, synthetic approach, and zinc concentration. It was also determined the importance of an adequate recovery gas, as employing argon instead of compressed air lead to measurements in which the recovery of the baseline was incomplete.

Our analysis of the influence of ageing on film thickness and morphology revealed that using aged instead of fresh sols or mixtures produces films that are excessively thick and present an inadequate morphology. The increase in thickness is ascribed to the increased viscosity of the aged sol or mixture, while the morphological effect manifests itself as an excessive grain growth of the smallest grains, concurring with an apparent decrease in porosity.

Our study of the effect of the synthetic approach demonstrated that, upon fabrication of a composite film, $ZnWO_4$ instead of ZnO is formed. This result of $ZnWO_4$ being formed from the mixing of either their precursor sols or a precursor salt of zinc into the WO_3 sol is consistent with the literature. The investigation of the films produced by the two syntheses proved that there are different morphological effects. In the case of the M-synthesis, with increasing zinc concentration there is a grain refinement effect which decreases the size of the largest grains and restricts the grain size distribution while maintaining it right-skewed. In the case of the S-synthesis there is a change in the shape of the grain size distribution with increasing zinc content, leading to more symmetrical distribution. Both these morphological changes lead to decreased contact between WO_3 and $ZnWO_4$ crystallites with increasing zinc concentration, which lead us to investigate towards lower zinc concentrations. Concerning the influence of synthesis on gas sensing, it was proved that the M-synthesis produces samples with improved response saturation at lower temperatures, while the S-synthesis produces films with faster response and recovery speeds at every temperature. This fact, together with the simpler experimental procedure of the S-synthesis, convinced us that this synthetic approach is the better one.

Our investigation of the influence of zinc concentration proved that, for very low zinc molar ratios, a net improvement in response over pure WO_3 is obtained. It was found that the response was maximum (OAC equal to 0.21 compared to 0.17 for pure WO_3) for a Zn/(W+Zn) molar ratio of 0.067, and then decreases for higher concentrations. This effect

is explained by two competing effects in the crystallinity and morphology of the material: for lower zinc concentrations, too little $ZnWO_4$ is formed, while for higher concentrations the evolution of the morphology via grain refinement diminishes the number of WO_3 and $ZnWO_4$ crystallites in contact. Our dynamic gas sensing tests performed on the sample with zinc molar ratio of 0.067 showed an improved response with respect to earlier samples ($\Delta Abs_{\lambda=870nm}$ improved from 0.15 to 0.20 at 100°C) thanks to the improvement over the course of this work of the synthetic and deposition process. Unfortunately, this sample showed worse recovery at temperatures lower than 100°C. We propose as an explanation for this slightly different behaviour the larger crystallite sizes obtained in the later samples, which must make desorption of H_2 from the $HxWO_3$ lattice more difficult at lower temperatures, in which the thermal desorption reaction is not active and thus the only available pathway for bleaching is the oxidation, hindered by the increased crystallite size. Nevertheless, we were able to reproduce similar results in terms of $\Delta Abs_{\lambda=870nm}$, response and recovery speeds, proving the reproducibility of our method. T=100°C was determined as the optimal operating temperature for our films as it produced the greatest response. The stability of the dynamic gas sensing behavior was investigated, proving that while response times decrease notably after the first cycle, recovery time increases linearly with successive cycles. The stability of the $\Delta Abs_{\lambda=870nm}$ over a number of cycles convinced us that our sensor shows good repeatability, and the variation of response and recovery time allowed us to formulate possible improvements in the use of these sensors.

Further investigation on the structure of our sensors is still required, especially via XPS and TEM/EDS, with the purpose of determining, respectively, the valence states of W and whether they are modified by the formation of Zn-W bonds with the former technique, and exactly how WO3 and ZnWO4 are distributed across the grains with the latter techniques. Variations in the gas sensing tests are to be considered too, particularly testing the response of our optimal composition to different concentrations of H_2 in order to obtain a sensitivity curve. I leave these investigations to my colleagues in the research group, hoping for further progress in this field of great importance.

Bibliography

[1] Christine Mansilla, Cyril Bourasseau, Camille Cany, Benjamin Guinot, Alain Le Duigou, Paul Lucchese. “Hydrogen Applications: Overview of the Key Economic Issues and Perspectives” in *Hydrogen Supply Chains,* edited by Catherine Azzaro-Pantel, pp. 271–292. Academic Press, 2018.

[2] Vergara, Diego, Pablo Fernández-Arias, Georgios Lampropoulos, and Álvaro Antón-Sancho. "Hydrogen Revolution in Europe: Bibliometric Review of Industrial Hydrogen Applications for a Sustainable Future" *Energies*, Vol. 17, No. 15, pp. 3658-3674, 2024

[3] Yang, J., Chen, X., Huang, C. and Ma, T. "Hotspot and frontier discovery of hydrogen detection technology based on bibliometrics", *Sensor Review*, Vol. 42 No. 5, pp. 599-610, 2022

[4] H. Idriss, M. Scott e V. Subramani, “Introduction to hydrogen and its properties” in *Compendium of Hydrogen Energy*, Edited by Velu Subramani, Angelo Basile, T. Nejat Veziroğlu, pp. 3-19. Woodhead Publishing, 2015.

[5] Ruichao Wei, Jiamei Lan, Liping Lian, Shenshi Huang, Chen Zhao, Zhurong Dong, Jingwen Weng, “A bibliometric study on research trends in hydrogen safety”, *Process Safety and Environmental Protection*, Vol. 159, pp. 1064-1081, 2022

[6] Hulanicki, A.; Glab, S.; Ingman, F. “Chemical sensors: Definitions and classification” , *Pure Appl. Chem.* Vol. 63, no. 9, pp. 1247–1250, 1991

[7] Matteo Tonezzer, Lai Van Duy, “Gas sensors” in *Encyclopedia of Sensors and Biosensors Volume 3: Sensor Development*, edited by Mehmet R. Yuce, pp. 185-208. Elsevier 2023

[8] Massimo Guglielmi, Alessandro Martucci, “Optical Gas Sensors” in *Sol-Gel Derived Optical and Photonic Materials*, edited by Rui Almeida, Alessandro Martucci, Luis Santos, Rocío Estefanía Rojas Hernández, pp. 271-291, Elsevier 2021.

[9] Vishal Baloria, Aditya Yadav, Preetam Singh and Govind Gupta, “Semiconductor oxide based chemiresistive gas sensors” in *Carbon Nanomaterials and their Nanocomposite-Based Chemiresistive Gas Sensors*, edited by Shivani Dhall, pp. 133-166, Elsevier 2023.

[10] S.M. Majhi, A. Mirzaei, H.W. Kim, S.S. Kim, T.W. Kim , “Recent advances in energy-saving chemiresistive gas sensors: a review”, *Nano Energy*, Vol. 79, no. 1 , pp. 1-25, 2021

[11] European Commission, Joint Research Centre, Weidner, E., Ortiz Cebolla, R., Bonato, C. et al., *Summary report for a hydrogen sensor workshop – Hydrogen safety sensors and their use in applications with hydrogen as an alternative fuel*, Publications Office, 2017

[12] T. Hübert, L. Boon-Brett, G. Black, U. Banach “Hydrogen sensors – A review”, *Sensors and Actuators B: Chemical*,vol. 157 no. 2, pp. 329-352, 2011

[13] Wiegleb, G. , “Physical-Chemical Gas Sensors” in *Gas Measurement Technology in Theory and Practice*, pp. 215-285. Springer, Wiesbaden. 2003

[14] Korotcenkov, Ghenadii, Sang Do Han, and Joseph R. Stetter. "Review of electrochemical hydrogen sensors." *Chemical reviews* vol. 109, no. 3, pp. 1402-1433. 2009.

[15] Gurlo, Alexander, and Ralf Riedel. "In situ and operando spectroscopy for assessing mechanisms of gas sensing." *Angewandte Chemie International Edition* vol. 46, no .21 pp. 3826-3848. 2007

[16] Della Gaspera, E., Guglielmi, M. and Martucci, A. “Sol–Gel for Gas Sensing Applications” In *The Sol-Gel Handbook*, edited by D. Levy and M. Zayat, pp. 1173-1206, Wiley 2015.

[17] Jia, Chenghao, Ling Zhao, Gang Huang, Litao Liu, Weirong Wang, Yunkai Yang, and Yang Miao.ji "A Review of Hydrogen Sensors for ECLSS: Fundamentals, Recent Advances, and Challenges" *Applied Sciences* vol. 13 no. 12, pp. 6869-6894. 2023.

[18] Della Gaspera, E., Antonello, A., Guglielmi, M., Post, M. L., Bello, V., Mattei, G., Romanato, F., and Martucci, A. “ Colloidal approach to Au-loaded TiO_2 thin films with optimized optical sensing properties” *Journal of Materials Chemistry*, vol. 21 no. 12, pp. 4293-4300. 2011

[19] Claes-Göran Granqvist , “Electrochromic Metal Oxides: An Introduction to Materials and Devices” from *Electrochromic materials and devices*, Edited by Mortimer, R. J., Rosseinsky, D. R., & Monk, P. M. John Wiley & Sons, 2015

[20] Gillet, M., Aguir, K., Lemire, C., Gillet, E., and Schierbaum, K. “The structure and electrical conductivity of vacuum-annealed WO3 thin films”, *Thin Solid Films*, vol. 467 no.1-2, pp. 239-246. 2004

[21] Razzaq, M., Khan, M. J., Imran, Z., Ahmad, M., Rasool, S., Rehan, M., Iqban, S., Anjum., M. A. R. , Mehboob, S., and Saifullah, M. “Enhanced electrochemical performance of WO3 thin films prepared from polyvinyl alcohol-modified nanoparticle ink”, *Solid State Ionics*, vol .*397*, 116246. 2023

[22] Zheng, H., Ou, J. Z., Strano, M. S., Kaner, R. B., Mitchell, A., & Kalantar‐zadeh, K. “Nanostructured tungsten oxide–properties, synthesis, and applications”, *Advanced Functional Materials*, vol. 21 no. 12, pp. 2175-2196. 2011

[23] Mirzaei, Ali, Jae-Hun Kim, Hyoun Woo Kim, and Sang Sub Kim. 2019. "Gasochromic WO_3 Nanostructures for the Detection of Hydrogen Gas: An Overview" *Applied Sciences* 9, no. 9: 1775.

[24] Wriedt, H. A. “The O - W (oxygen-tungsten) system”, *Bulletin of Alloy phase diagrams*, vol. 10 no. 4, pp. 368-384. 1989

[25] Polaczek, A., Pekala, M., & Obuszko, Z. “Magnetic susceptibility and thermoelectric power of tungsten intermediary oxides”, *Journal of Physics: Condensed Matter*, vol. *6* no. 39, 7909-7920. 1994

[26] Gullapalli, S. K., Vemuri, R. S., & Ramana, C. V. “Structural transformation induced changes in the optical properties of nanocrystalline tungsten oxide thin films”, *Applied physics letters*, vol. 96 no. 17. 2010

[27] Yoffe, A. D. “Low-dimensional systems: quantum size effects and electronic properties of semiconductor microcrystallites (zero-dimensional systems) and some quasi-two-dimensional systems” *Advances in Physics*, vol. 42 no. 2, pp. 173-262. 1993

[28] Hjelm, A., Granqvist, C. G., & Wills, J. M. “Electronic structure and optical properties of WO 3, LiWO 3, NaWO 3, and HWO 3” *Physical Review B*, vol. 54 no. 4, pp. 2436-2445. 1996

[29] Davazoglou, D., & Donnadieu, A. “Structure and optical properties of WO3 thin films prepared by chemical vapour deposition” *Thin solid films*, vol. 147 no.2, pp. 131-142. 1987

[30] Claes-Göran Granqvist, “Electrochromic Metal Oxides: An Introduction to Materials and Devices” in Electrochromic Materials and Devices, edited by Roger J. Mortimer, David R. Rosseinsky, and Paul M. S. Monk, pp. 1-40. Wiley 2015

[31] Dickens, P. G., Moore, J. H., & Neild, D. J. “Thermochemistry of hydrogen tungsten bronze phases HxWO3”, *Journal of Solid State Chemistry,* vol.7 no.2, pp.241–244. 1973

[32] Orel, B., Grošelj, N., Krašovec, U. O., Ješe, R., & Georg, A., “IR spectroscopic investigations of gasochromic and electrochromic sol-gel—derived peroxotungstic acid/ormosil composite and crystalline WO 3 films”, *Journal of sol-gel science and technology*, vol. 24, pp. 5-22. 2002

[33] Wittwer, V., Schirmer, O. F., & Schlotter, P. “Disorder dependence and optical detection of the Anderson transition in amorphous H_xWO_3 bronzes” *Solid State Communications*, vol. 25 no. 12, pp. 977-980. 1978

[34] Yang, M., Zhang, X., Grosjean, A., Soroka, I., & Jonsson, M. “Kinetics and Mechanism of the Reaction between H_2O_2 and Tungsten Powder in Water”, *The Journal of Physical Chemistry C*, vol.119 no.39, pp.22560-22569. 2015

[35] Ştefan, M., Bica, E., Muresan, L., Grecu, R., Indrea, E., Trif, M., & Popovici, E. J. “Synthesis and characterisation of tungsten trioxide powder prepared by sol-gel route”, *Journal of Optoelectronics and Advanced Materials*, vol.2 no.1, pp.115-118. 2010

[36] Hemati, A., Ranjbar, M., Kameli, P., & Salamati, H. “Gasochromic tungsten oxide films with PdCl2 solution as an aqueous Hydrogen catalyst”, *Solar energy materials and solar cells*, vol.*108*, pp.105-112. 2013

[37] Ippolito, S. J., Kandasamy, S., Kalantar-Zadeh, K., & Wlodarski, W. “Hydrogen sensing characteristics of WO3 thin film conductometric sensors activated by Pt and Au catalysts” *Sensors and Actuators B: Chemical*, vol.108 no.1-2, pp. 154-158. 2005

[38] Tan, T., Hang, Z., Li, X., Wang, S., Homewood, K., Xia, X., Bao, Y. and Gao, Y. “Ultra-high-response heat free H2 sensor based on a WO3/Pt-ZnO thin film”, *Journal of Alloys and Compounds*, vol. 979, 173527. 2024

[39] Longato, A., Vanzan, M., Colusso, E., Corni, S., & Martucci, A. “Enhancing tungsten oxide gasochromism with noble metal nanoparticles: The importance of the interface” *Small*, vol. 19 no.6, 2205522. 2023

[40] Yamazoe, N., & Miura, N. “Some basic aspects of semiconductor gas sensors” in *Chemical sensor technology*, vol .*4*, edited by Shigeru Yamaguchi, pp .19-42. Elsevier 1992

[41] Zhu, L. Y., Ou, L. X., Mao, L. W., Wu, X. Y., Liu, Y. P., & Lu, H. L. “Advances in noble metal-decorated metal oxide nanomaterials for chemiresistive gas sensors: overview”, *Nano-Micro Letters*, vol. 15 no. 1, pp. 88-162. 2023

[42] B. Poelsema, G. Mechtersheimer, G. Cosma, “The interaction of hydrogen with platinum(S)-9(111) x (111) studied with helium beam diffraction” *Surf. Sci.,* vol. 111 no. 3, pp. 519-544. 1981

[43] Połczyński, P., & Jurczakowski, R. “Extremely fast hydrogen absorption/desorption through platinum overlayers”, *Journal of Power Sources*, vol. 305, pp. 233-239. 2016

[44] Will, F. G. “Hydrogen adsorption on platinum single crystal electrodes: I. Isotherms and heats of adsorption”, *Journal of the electrochemical society*, vol. 112 no.4, pp.451-456. 1965

[45] Morin, S., Dumont, H., & Conway, B. E. “Evaluation of the effect of two-dimensional geometry of Pt single-crystal faces on the kinetics of upd of H using impedance spectroscopy”, *Journal of Electroanalytical Chemistry*, vol .412 no.1-2, pp. 39-52. 1996

[46] Xi, Y., Zhang, Q., & Cheng, H. “Mechanism of Hydrogen Spillover on WO3 (001) and Formation of H x WO3 (x= 0.125, 0.25, 0.375, and 0.5)”, *The Journal of Physical Chemistry C*, vol.118 no.1, pp.494-501. 2014

[47] Herricks, T., Chen, J., & Xia, Y. “Polyol synthesis of platinum nanoparticles: control of morphology with sodium nitrate” *Nano Letters*, vol .4 no.12, pp. 2367-2371. 2004

[48] Chernov, A. A. Theory of Stability of Face Forms of Crystals. *Soviet Physics Crystallography, USSR*, vol. 16 no.4, 734. 1972

[49] Long, N. V., Chien, N. D., Hayakawa, T., Hirata, H., Lakshminarayana, G., & Nogami, M. “The synthesis and characterization of platinum nanoparticles: a method of controlling the size and morphology”, *Nanotechnology*, vol.21 no.3, 035605. 2009

[50] Boita, J., Nicolao, L., Alves, M. C., & Morais, J. “Observing Pt nanoparticle formation at the atomic level during polyol synthesis”, *Physical Chemistry Chemical Physics*, vol.16 no.33, pp.17640-17647. 2014

[51] Tsuji, M., Jiang, P., Hikino, S., Lim, S., Yano, R., Jang, S. M., ... & Kamarudin, K. S. N. “ Toward to branched platinum nanoparticles by polyol reduction: a role of poly (vinylpyrrolidone) molecules”, *Colloids and Surfaces A: Physicochemical and Engineering Aspects*, vol.317 no.1-3, pp.23-31. 2008

[52] Chen, J., Herricks, T., & Xia, Y. “Polyol synthesis of platinum nanostructures: control of morphology through the manipulation of reduction kinetics”, *Angewandte Chemie International Edition*, vol. 44 no. 17, pp. 2589-2592. 2005

[53] Fiévet, F., Ammar-Merah, S., Brayner, R., Chau, F., Giraud, M., Mammeri, F., ... & Viau, G. “The polyol process: a unique method for easy access to metal nanoparticles with tailored sizes, shapes and compositions”, *Chemical Society Reviews*, vol.47 no.14, pp.5187-5233. 2018

[54] Dye, R. F. “Ethylene glycols technology”, *Korean Journal of Chemical Engineering*, vol.18, pp.571-579. 2001

[55] Chen, J., Yang, G., Shen, D., Zhang, Q., Liu, Z., & Peng, F. “ Surfactant-free synthesis of colloidal Pt nanoparticles with a wide size range from 2 to 10 nm for studying size effect”, *International Journal of Hydrogen Energy*, vol.53, pp.728-735. 2024

[56] Borysiewicz, M. A. “ZnO as a functional material, a review” *Crystals*, vol.9 no.10,pp. 505-533. 2016

[57] Sharma, D. K., Shukla, S., Sharma, K. K., & Kumar, V. “A review on ZnO: Fundamental properties and applications”, *Materials Today: Proceedings*, vol.49, pp.3028-3035. 2022

[58] Desgreniers, S. “High-density phases of ZnO: Structural and compressive parameters”, *Physical Review B*, vol.58 no.21, pp.14102-14105. 1998

[59] . Hadis Morkoç and Ümit Özgur . “General Properties of ZnO”, in *Zinc Oxide: Fundamentals, Materials and Device Technology*. Wiley 2009

[60] Bhati, V. S., Hojamberdiev, M., & Kumar, M. “Enhanced sensing performance of ZnO nanostructures-based gas sensors: A review” *Energy Reports*, vol.*6*, pp.46-62. 2020

[61] McCluskey, M. D., & Jokela, S. J. “Defects in zno”, *Journal of Applied Physics*, vol.106 no.7. 2009

[62] Doh, W. H., Roy, P. C., & Kim, C. M. “Interaction of hydrogen with ZnO: surface adsorption versus bulk diffusion”, *Langmuir*, vol.26 no.21, pp.16278-16281. 2010

[63] Znaidi, L. “Sol–gel-deposited ZnO thin films: A review”, *Materials Science and Engineering: B*, vol.174 no.1-3, pp.18-30. 2010

[64] Adl, A. H., Kar, P., Farsinezhad, S., Sharma, H., & Shankar, K. “Effect of sol stabilizer on the structure and electronic properties of solution-processed ZnO thin films”, *Rsc Advances*, vol.*5* no.106, pp.87007-87018. 2015

[65] Bahadur, H., Srivastava, A. K., Sharma, R. K., & Chandra, S. “Morphologies of sol–gel derived thin films of ZnO using different precursor materials and their nanostructures”, *Nanoscale Research Letters*, vol.*2*, pp.469-475. 2007

[66] Mahmud, M. A., Elumalai, N. K., Upama, M. B., Wang, D., Soufiani, A. M., Wright, M., ... & Uddin, A “Solution-processed lithium-doped ZnO electron transport layer for efficient triple cation (Rb, MA, FA) perovskite solar cells”, *ACS applied materials & interfaces*, vol.*9* no.39, pp.33841-33854. 2017

[67] Znaidi, L., Illia, G. S., Benyahia, S., Sanchez, C., & Kanaev, A. V. (2003). Oriented ZnO thin films synthesis by sol–gel process for laser application. *Thin solid films*, vol.*428* no.1-2, pp.257-262.

[68] Gómez-Núñez, A., López, C., Alonso-Gil, S., Roura, P., & Vilà, A. “Study of a sol–gel precursor and its evolution towards ZnO”, *Materials Chemistry and Physics*, vol.162, pp.645-651. 2015

[69]Gómez-Núñez, A., Alonso-Gil, S., López, C., Roura-Grabulosa, P., & Vilà, A. “From ethanolamine precursor towards ZnO—how N is released from the experimental and theoretical points of view”, *Nanomaterials*, vol.9 no.10, 1415. 2019

[70] Benramache, S., Rahal, A., & Benhaoua, B. “The effects of solvent nature on spray-deposited ZnO thin film prepared from Zn (CH3COO) 2, 2H2O”, *Optik*, vol.*125* no.2, pp.663-666. 2014

[71] Sagar, P., Shishodia, P. K., & Mehra, R. M. “ Influence of pH value on the quality of sol–gel derived ZnO films. *Applied surface science*” vol.*253* no.12, pp.5419-5424. 2007

[72] Nehmann JB, Ehrmann N, Reineke-Koch R, Bahnemann DW “ Aluminum-doped zinc oxide sol–gel thin films: influence of the sol’s water content on the resistivity.”, *Thin Solid Films* vol.556, pp.168–173. 2014

[73] Hayami, R., Endo, N., Abe, T. *et al.* “Zinc–diethanolamine complex: synthesis, characterization, and formation mechanism of zinc oxide via thermal decomposition”, *Journal of Sol-Gel Science and Technology,* vol.87, pp.743–748. 2018

[74] Najafidoust, A., Hakki, H. K., Avalzali, H. A., & Bonab, M. K. A. “ The role of Diethanolamine as stabilizer in controlling morphology, roughness and photocatalytic activity of ZnO coatings in sonophotodegradation of methylene blue” *Materials Research Express*, vol.*6* no.9, 096401. 2019

[75] Kim J.-H., Lee J.-H., Park Y., Kim J.-Y., Mirzaei A., Kim H.W., Kim S.S. , “Toluene- and benzene-selective gas sensors based on Pt- and Pd-functionalized ZnO nanowires in self-heating mode” *Sensors and Actuators B: Chemical*, vol.294, pp. 78-88. 2019

[76] Nie, L., Guo, X., Gao, C., Wu, X., Chen, J., & Peng, L. “Effect of ZnO Content on the Optical H2 Sensing Properties of Porous Pt/(WO3) 1− x (ZnO) x Films”, *Journal of Electronic Materials*, vol.51 no.11, pp.6463-6474. 2022

[77] Lei, B., Zhang, H., Zhao, Q., Liu, W., Wei, Y., Lu, Y., ... & Cai, W. “Facile synthesis of ZnO/WO3 nanocomposite porous films for high-performance gas sensing of multiple VOCs”, *Nanomaterials*, vol.13 no.4, pp.733-746. 2023

[78] Kröger, F. A. “Some aspects of the luminescence of solids” pp. 232-233. Elsevier Publishing Company. New York, 1948

[79] Van Uitert, L. G., and Preziosi, S. “Zinc tungstates for microwave maser applications”, *Journal of Applied Physics*, vol.33 no.9, pp. 2908-2909. 1962

[80] Oi, T., Takagi, K., and Fukazawa, T. “Scintillation study of ZnWO4 single crystals” *Applied Physics Letters*, vol.36 no.4, 278-279. 1980

[81] Földvári, I., Peter, A., Keszthelyi-Lándori, S., Capelletti, R., Cravero, I., and Schmidt, F. “Improvement of the quality of ZnWO4 single crystals for scintillation applications” *Journal of Crystal Growth*, vol.79 no.1-3, pp. 714-719. 1986

[82] Yu, S. H., Liu, B., Mo, M. S., Huang, J. H., Liu, X. M., & Qian, Y. T. “General synthesis of single-crystal tungstate nanorods/nanowires: a facile, low-temperature solution approach”, *Advanced Functional Materials*, vol.13 no.8, pp. 639-647. 2003

[83] Zhao, X., Yao, W., Wu, Y., Zhang, S., Yang, H., & Zhu, Y. “Fabrication and photoelectrochemical properties of porous ZnWO4 film”, *Journal of Solid State Chemistry*, vol.179 no.8, pp. 2562-2570. 2006

[84] Dong, T., Li, Z., Ding, Z., Wu, L., Wang, X., & Fu, X. “Characterizations and properties of Eu3+-doped ZnWO4 prepared via a facile self-propagating combustion method”, *Materials Research Bulletin*, vol.43 no.7, pp.1694-1701. 2008

[85] Kim, M. J., & Huh, Y. D. “Ligand-assisted hydrothermal synthesis of ZnWO4 rods and their photocatalytic activities”, *Materials Research Bulletin*, vol.45 no.12, pp. 1921-1924. 2010

[86] He, D., Zhang, X., Xie, T., Zhai, J., Li, H., Chen, L., and Jiang, T. “Studies of photo-induced charge transfer properties of ZnWO4 photocatalyst”, *Applied Surface Science*, vol.*257* no.6, pp.2327-2331. 2011

[87] Dodd, A., McKinley, A., Tsuzuki, T., & Saunders, M. “Mechanochemical synthesis of nanoparticulate ZnO–ZnWO4 powders and their photocatalytic activity”, *Journal of the European Ceramic Society*, vol.29 no.1, pp.139-144. 2009

[88] Khyzhun, O. Y., Bekenev, V. L., Atuchin, V. V., Galashov, E. N., & Shlegel, V. N. “Electronic properties of ZnWO4 based on ab initio FP-LAPW band-structure calculations and X-ray spectroscopy data”, *Materials Chemistry and Physics*, vol.*140* no.2-3, pp. 588-595. 2013

[89] Schofield, P. F., Knight, K. S., Redfern, S. A. T., & Cressey, G. “Distortion characteristics across the structural phase transition in (Cu1− xZnx) WO4”, *Acta Crystallographica Section B: Structural Science*, vol.*53* no.1, pp. 102-112. 1997

[90] Chen, S., Sun, S., Sun, H., Fan, W., Zhao, X., & Sun, X. “Experimental and theoretical studies on the enhanced photocatalytic activity of ZnWO4 nanorods by fluorine doping” *The Journal of Physical Chemistry C*, vol.*114* no.17, pp. 7680-7688. 2010

[91] Lin, J., Lin, J., & Zhu, Y. “Controlled synthesis of the ZnWO4 nanostructure and effects on the photocatalytic performance”, *Inorganic chemistry*, vol.46 no.20, pp. 8372-8378. 2007

[92] Lacomba-Perales, R., Ruiz-Fuertes, J., Errandonea, D., Martínez-García, D., & Segura, A. “Optical absorption of divalent metal tungstates: Correlation between the band-gap energy and the cation ionic radius”, *Europhysics letters*, vol. *83* no.3, 37002. 2006

[93] Zhao, X., Yao, W., Wu, Y., Zhang, S., Yang, H., & Zhu, Y. “Fabrication and photoelectrochemical properties of porous ZnWO4 film”, *Journal of Solid State Chemistry*, vol.*179* no.8, pp. 2562-2570. 2006

[94] Li, Cong et al. "Enhancement of gas-sensing abilities in p-type ZnWO4 by local modification of Pt nanoparticles", *Analytica Chimica Acta* vol.927 pp. 107-116. 2016

[95] Dai, M., He, Z., Zhang, P., Li, X., & Wang, S. ZnWO4-ZnIn2S4 S-scheme heterojunction for enhanced photocatalytic H2 evolution. *Journal of Materials Science & Technology*, vol.*122*, pp. 231-242. 2022

[96] Hu, P., Chen, J., Ma, Q., Yin, J., Zhou, D., Kou, C., ... & Xu, J. “One-step thermal compensation decomposition synthesis of ZnWO4/WO3 composite with synergy of multiple structural effects for efficient trace H2S detection”, *Sensors and Actuators B: Chemical*, vol.381:133388. 2023

[97] Cai, L. X., Chen, L., Sun, X. Q., Geng, J., Liu, C. C., Wang, Y., & Guo, Z. “Ultra-sensitive triethylamine gas sensors based on polyoxometalate-assisted synthesis of $ZnWO_4$/ZnO hetero-structured nanofibers”, *Sensors and Actuators B: Chemical*, vol.*370*:132422. 2022

[98] Kakati, N., Jee, S. H., Kim, S. H., Oh, J. Y., & Yoon, Y. S. “Thickness dependency of sol-gel derived ZnO thin films on gas sensing behaviors”, *Thin Solid Films*, vol.519 no.1, pp.494-498. 2010

[99] Chen, W., Shen, H., Zhu, X., Yao, H., & Wang, W. “Preparation and photochromic properties of PEG-400 assisted WO3–TiO2–ZnO composite films”, *Ceramics International*, vol.41 no.10, pp.14008-14012. 2015

[100] Hunge, Y. M., Mahadik, M. A., Moholkar, A. V., & Bhosale, C. H. “Photoelectrocatalytic degradation of phthalic acid using spray deposited stratified WO3/ZnO thin films under sunlight illumination”, *Applied Surface Science*, vol.*420*, pp.764-772. 2017

[101] Leonard, K. C., Nam, K. M., Lee, H. C., Kang, S. H., Park, H. S., & Bard, A. J. “ZnWO4/WO3 composite for improving photoelectrochemical water oxidation” *The Journal of Physical Chemistry C*, no.117 vol.31, pp.15901-15910. 2013

[102] Hamrouni, A., Moussa, N., Di Paola, A., Parrino, F., Houas, A., & Palmisano, L. “Characterization and photoactivity of coupled ZnO–ZnWO4 catalysts prepared by a sol–gel method”, *Applied Catalysis B: Environmental*, vol.154, pp.379-385. 2014

[103] Tian, Y. F., Yu, P., Liu, X., Xie, R. S., Liu, Y., & Xiao, D. Q. “Structure and Photoluminescence Property of ZnWO4 Films Prepared by Sol-Gel Processing”, *Ferroelectrics*, vol.382 no.1, pp.16-21. 2009

[104] Rice, S. B., Chan, C., Brown, S. C., Eschbach, P., Han, L., Ensor, D. S., ... & Grulke, E. A. “Particle size distributions by transmission electron microscopy: an interlaboratory comparison case study”, *Metrologia*, vol.50 no.6:663. 2013

[105] Norhidayah, C. A., Kamaruddin, S. A., Nayan, N., Tawil, S. N. M., & Sahdan, M. Z. “Effects of ageing time of ZnO sol on properties of ZnO films by sol gel spin coating” *Advanced Materials Research*, vol.925, pp.329-333. 2014

[106] Nazarzadeh, M., Irannejad, A., & Joodaki, M. “Effect of temperature in the sol–gel method on the morphology of the ZnO layer used as a window layer in the PbS quantum dot solar cells”, *Bulletin of Materials Science*, vol.47 no.2, pp.68. 2014

[107] Shuangjiao, W., Zhenglan, B., Xingquan, W., Xiaokang, M., Guilin, Z., Liang, X., ... & Fenghong, C. “Study of WO3/Pt hydrogen sensitive film fabricated by Sol-Gel method”, *Optik*, vol.271, 170124. 2022

[108] Takahashi, H., Okazaki, S., Nishijima, Y., & Arakawa, T. “Optimization of hydrogen sensing performance of Pt/WO3 gasochromic film fabricated by sol–gel method”, *Sensors and Materials*, vol.*29* no.9, pp.1259-1268.

[109] Qadri, M. U., Diaz Diaz, A. F., Cittadini, M., Martucci, A., Pujol, M. C., Ferré-Borrull, J., ... & Díaz, F. “Effect of Pt nanoparticles on the optical gas sensing properties of WO3 thin films”, *Sensors*, vol.14 no.7, 11427-11443. 2014

[110] Van Minh, N., & Hung, N. MA “A study of the optical properties in ZnWO4 nanorods synthesized by hydrothermal method”, *Materials Sciences and Applications*, vol.2 no.8, pp.988-992. 2011

[111] Au, B. W. C., Chan, K. Y., & Knipp, D. “Effect of film thickness on electrochromic performance of sol-gel deposited tungsten oxide (WO3)”, *Optical Materials*, vol.94, pp.387-392. 2019

[112] Paipitak, K., Techitdheera, W., Porntheeraphat, S., & Pecharapa, W. “Influence of Ti and Zn dopants on structural properties and electrochromic performance of sol-gel derived WO3 thin films”, *Energy Procedia*, vol.34, pp.689-696. 2013

[113] Lu, Z. Q., Quinn, T., & Reehal, H. S. “Polarization-dependent Raman spectra of thin crystalline silicon films”, *Journal of Applied Physics*, vol. 97 no.3:033512. 2005

[114] Sáenz-Hernández, R. J., Herrera-Pérez, G. M., Uribe-Chavira, J. S., Grijalva-Castillo, M. C., Elizalde-Galindo, J. T., & Matutes-Aquino, J. A. “Correlation between thickness and optical properties in nanocrystalline γ-Monoclinic WO3 thin films” *Coatings*, vol.12 no.11:1727. 2022

[115] Santato, C., Odziemkowski, M., Ulmann, M., & Augustynski, J. “Crystallographically oriented mesoporous WO3 films: synthesis, characterization, and applications”, *Journal of the American Chemical Society*, vol.123 no.43, pp.10639-10649. 2001

[116] Díaz-Reyes, J., Castillo-Ojeda, R., Galván-Arellano, M., & Zaca-Moran, O. “Characterization of WO3 thin films grown on silicon by HFMOD”, *Advances in Condensed Matter Physics*, 1:591787. 2013

[117] Van Minh, N., & Hung, N. M. “ A study of the optical properties in ZnWO4 nanorods synthesized by hydrothermal method” *Materials Sciences and Applications*, vol.2 no.8, pp.988-992. 2011

[118] Liu, M. T., Xiao, E. C., Lv, J. Q., Qi, Z. M., Yue, Z., Chen, Y., ... & Shi, F. “Phonon characteristics and intrinsic properties of single phase ZnWO4 ceramic” *Journal of Materials Science: Materials in Electronics*, vol.31, pp.6192-6198. 2020

[119] Yahia, S. B., Znaidi, L., Kanaev, A., & Petitet, J. P. “Raman study of oriented ZnO thin films deposited by sol–gel method” *Spectrochimica Acta Part A: Molecular and Biomolecular Spectroscopy*, vol.71 no.4, pp.1234-1238. 2008

[120] Hammouda, A., Canizarès, A., Simon, P., Boughalout, A., & Kechouane, M. “Improving the sensitivity of Raman signal of ZnO thin films deposited on silicon substrate” *Vibrational Spectroscopy*, vol.62, pp.217-221. 2012

[121] Vemuri, R. S., Engelhard, M. H., & Ramana, C. V. “Correlation between surface chemistry, density, and band gap in nanocrystalline WO3 thin films”, *ACS applied materials & interfaces*, vol.4 no.3, pp.1371-1377. 2012

[122] Kalanur, S. S., Noh, Y. G., & Seo, H. “Engineering band edge properties of WO3 with respect to photoelectrochemical water splitting potentials via a generalized doping protocol of first-row transition metal ions”, *Applied Surface Science*, vol.509:145253. 2020

[123] Okazaki, S., & Johjima, S. “Temperature dependence and degradation of gasochromic response behavior in hydrogen sensing with Pt/WO3 thin film” *Thin Solid Films*, vol.*558*, pp.411-415. 2014

[124] Mazur, M., Kapuścik, P., Weichbrodt, W., Domaradzki, J., Mazur, P., Kot, M., & Flege, J. I. “WO3 Thin-Film Optical Gas Sensors Based on Gasochromic Effect towards Low Hydrogen Concentrations”, *Materials*, vol.*16* no.10, pp.3831. 2023

[125] Fardindoost, S., Rahimi, F., & Ghasempour, R. “Pd doped WO3 films prepared by sol–gel process for hydrogen sensing” *International Journal of Hydrogen Energy*, vol.*35* no.2, pp.854-860. 2010

[126] Zhan, F., Liu, Y., Wang, K., Liu, Y., Yang, X., Yang, Y., ... & Li, J. “In situ formation of WO3-based heterojunction photoanodes with abundant oxygen vacancies via a novel microbattery method”, *ACS applied materials & interfaces*, *11*(17), 15467-15477. 2019

[127] Wang, B. B., Zhong, X. X., He, C. L., Zhang, B., Shao, R. W., Shvalya, V., ... & Ostrikov, K. “Controlling oxygen vacancies of WOx suboxides by ZnWO4 nanophase hybridization”, *Materials Science and Engineering: B*, *262*, 114706. 2020

[128] A. Georg Wg, R. Neumann, V. Wittwer, “Mechanism of the gasochromic coloration of porous WO3 films”, *Solid State Ionics*, vol.127, pp. 319-328. 2000

[129] J.Y. Luo, S.Z. Deng, Y.T. Tao, F.L. Zhao, L.F. Zhu, L. Gong, *et al.* “Evidence of localized water molecules and their role in the gasochromic effect of WO3 nanowire films”, *Journal of Physical Chemisty C*, vol.113 , pp. 15877-1588. 2009